Doctoral Thesis

Pixel detector modules performance for ATLAS IBL and future pixel detectors

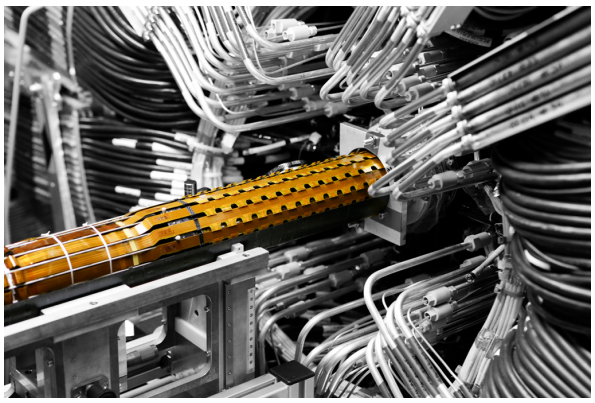

Dissertation
zur Erlangung des akademischen Grades
eines Doktors der Naturwissenschaften
der Fakultät Physik der Technischen Universität Dortmund

vorgelegt von

Jennifer Jentzsch*

March 2015

TU Dortmund - Fakultät für Physik
Experimentelle Physik IV

*jennifer.jentzsch@tu-dortmund.de

1. Gutachter : Prof. Dr. Gössling

2. Gutachter : Prof. Dr. Weis

Prüfungsvorsitz : Prof. Dr. Böhmer

Prüfungsbeisitz : Fr. Dr. Siegmann

Datum des Einreichens der Arbeit: 27. März 2015

Datum der Verteidigung: 19. Juni 2015

”Da kiekste, wa?”

- Berliner Redensart

Abstract

The ATLAS Detector is one of the four big particle physics experiments at CERN's LHC. Its innermost tracking system consisted of the 3-Layer silicon Pixel Detector (∼80M readout channels) in the first run (2010-2012). Over the past two years it was refurbished and equipped with new services as well as a new beam monitor. The major upgrade, however, was the Insertable B-Layer (IBL). It adds ∼12M readout channels for improved vertexing, tracking robustness and b-tagging performance for the upcoming runs, before the high luminosity upgrade of the LHC will take place.

This thesis covers two main aspects of Pixel detector performance studies: The main work was the planning, commissioning and operation of a test bench that meets the requirements of current pixel detector components. Each newly built ATLAS IBL stave was thoroughly tested, following a specifically developed procedure, and initially calibrated in that setup. A variety of production accompanying measurements as well as preliminary results after integration into the ATLAS Pixel Detector, right before the start of the second LHC run, will be presented and discussed.

The second focus of this thesis are pixel detector studies with the help of high energetic particle beams. A 3D prototype sensor from the ATLAS IBL production was studied at various rotation angles to investigate its charge collection properties. During these measurements, tracking information was provided by the Timepix telescope. Preliminary results depicting the detectors performance at various particle incidence angles will be evaluated.

Contents

I cry Babel! Babel! Look at me now,
but the walls of my town,
they come crumbling down.
- Mumford & Sons

Chapter 1

High Energy Physics at CERN

CERN[1] was founded in 1954 as a european facility for peaceful fundamental research. Since 2014 it has 21 member states and many more are in the ratification process to join, which also includes non-european countries. Over its 60 years of existence it has established various accelerators and experiments that significantly contributed to mankind's understanding of nature. In the 1960's a theoretical model was established, describing the fundamental particles along with the forces that are responsible for the interactions among them, the Standard Model of particle physics. It describes particles' properties with high precision, which could be verified in various experiments. It also predicted a number of new particles that were eventually discovered in high energy physics experiments. In 2013 Francois Englert and Peter Higgs were awarded the Nobel Prize in Physics "for the theoretical discovery of a mechanism that contributes to our understanding of the origin of mass of subatomic particles, and which recently was confirmed through the discovery of the predicted fundamental particle, by the ATLAS[2] and CMS[3] experiments at CERN's Large Hadron Collider" [1]. This so-called Higgs Boson was measured by the two experiments with a significance of $5.9\,\sigma$ [2] and $5.0\,\sigma$ [3], respectively.

However, not all observations are well described in that Standard Model. For instance, the relatively high amount of matter in the universe along with the lack of visible anti-matter, the origin of dark matter, supersymmetry, the unification of the forces as well as the gravitational force are not properly described and understood yet. In order to probe the Standard Model and the physics beyond, particle accelerators have been built to mimic the high energy conditions shortly after the big bang. At present, the LHC[4] is the accelerator providing the highest available center of mass energy in proton-proton collisions. The secondary particles emerging from those collisions are studied in on-going high precision experiments. One main requirement for such detailed studies is the precise vertex reconstruction of the secondary particle decays and determination of their momentum with the help of a surrounding magnetic field. Therefore, tracking detectors are built close to the interaction regions, resulting in high demands on the

[1] **C**onseil **E**uropéen pour la **R**echerche **N**ucléaire
[2] **A** **T**oroidal **L**HC **A**pparatu**S**
[3] **C**ompact **M**uon **S**olenoid
[4] **L**arge **H**adron **C**ollider

used components, namely a fine spatial resolution, fast readout, low power consumption and reliable operation even in high radiation environments. Nowadays, mainly solid state detectors are used in those environments as they meet the requirements best. However, regular maintenance and upgrades on their components are necessary to successfully continue the search for a deeper understanding of nature and new physics.

The focus of this thesis is the state-of-the-art 4-Layer ATLAS Pixel Detector. To give the corresponding context, the Standard Model of particle physics, the CERN accelerator complex and its four big experiments along with the foreseen upgrades of the LHC and the ATLAS Detector will be introduced in the following pages. Furthermore, particle detection techniques focussing on silicon detectors including radiation damages expected from the harsh LHC environment will be described.

Chapter 2 is dedicated to the original 3-Layer ATLAS Pixel Detector after three years of successful operation. Its composition, calibration, performance so far and the carried out upgrades will be presented.

The main part of this thesis, Chapter 3, will cover the ATLAS Insertable B-Layer, the fourth layer recently added to the existing ATLAS Pixel Detector. After describing the various components and production steps, the established testing setup along with calibration results will be depicted. First commissioning and cosmic data taking results obtained shortly before the restart of the LHC in 2015 will be shown.

In Chapter 4 a measurement carried out at a testbeam facility at CERN during the prototyping phase of the ATLAS Insertable B-Layer will be described. These kinds of studies are essential for sensor characterization, particularly with regard to future detector upgrades. Furthermore, a completely new sensor characterization method will be introduced. Based on the idea of Computed Tomography a way of evaluating the charge collection efficiency in a three dimensional manner is investigated, which is a very promising approach for complementing sensor characterizations carried out in laboratories and two dimensional hit and charge collection efficiency studies from conventional testbeam measurements.

1.1. The Standard Model of Particle Physics

In the Standard Model of particle physics there are twelve fermions (half-integer spin particles), five gauge bosons (integer spin particles) and the Higgs boson (spin-0 particle). The fermions are grouped into three generations with two quarks and two leptons each. The first one consists of the lightest quarks, namely up (u) and down (d) along with the electron (e) and its neutrino (ν_e). Matter is made up of only those stable particles. The second generation holds the charm (c) and the strange (s) quark and the muon (μ) with its neutrino (ν_μ). The heaviest quarks are found in the third generation, the bottom[1] (b) and the top (t) quark. The corresponding leptons are the tau (τ) and the tau neutrino (ν_τ).

[1]Sometimes also called **b**eauty quark.

Four fundamental forces are known today, the electromagnetic, the strong and the weak force, which are described by the Standard Model, and the gravitational force, which still eludes a quantum mechanical description. The forces among the fundamental particles couple to corresponding charges. All fermions carry weak charge and thus interact weakly while only electrically charged particles take part in the electromagnetic interaction. The strong force couples to the so-called color charge, which only the quarks and gluons possess. The weak force is mediated by two electrically charged gauge bosons, W^+ and W^-, and one neutral boson, Z^0. The carrier of the electromagnetic force is the mass-less photon (γ). The strong force that confines quarks into hadrons is carried by the gluon (g).

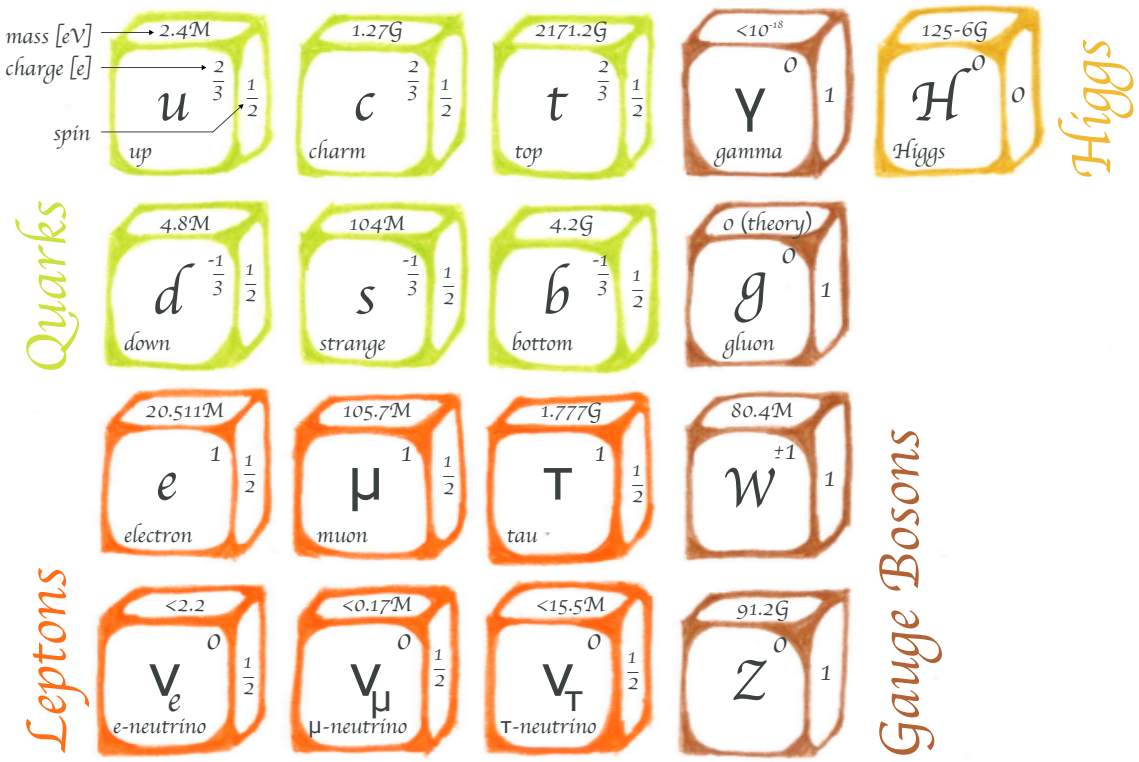

Figure 1.1.: The Standard Model of particle physics.

The fact that the particles have mass is described with the help of the Higgs-mechanism, breaking the local electro-weak symmetry. It describes the particles' interaction with the all-surrounding Higgs-field. One can assign a particle to the excitation of such a field which is the Higgs (H^0) particle. The named particles along with their properties are summarized in Figure 1.1.

1.2. The LHC and its Experiments

The current layout of the CERN accelerator complex is shown in Figure 1.2. The main focus is the high energy proton physics for fundamental research. Therefor, hydrogen from a bottle is injected into a duoplasmatron with a high electric field that strips the electrons off the nuclei. The resulting free protons are bunched and pre-accelerated in a radio frequency quadrupole before entering the Linear Accelerator 2 (LINAC 2). There they are accelerated to an energy of 50 MeV. After being transferred to the Booster they are accelerated to 1.4 GeV, then to 25 GeV in the Proton Synchrotron (PS) and to 450 GeV in the Super Proton Synchrotron (SPS) before entering the LHC. In the LHC they are further accelerated to a maximum energy of 7 TeV and finally brought to collide. In a second run mode of the LHC ions can collide. In that case the ions are transferred from Linear Accelerator 3 (LINAC 3) at an energy of 4.2 MeV/u to the Low Energy Ion Ring (LEIR) accelerator which then feeds them into the PS and again via the SPS to the LHC.

Apart from the high energy physics collisions sector there are antimatter experiments at the AD (Antiproton Decelerator), nuclear physics experiments like ISOLDE (Isotope Separator On Line DEvice) at the Booster and n-ToF (neutron Time of Flight) at the PS. Furthermore, there are experimental areas for a wide range of experiments including detector characterization at the PS and SPS, irradiation facilities at the PS and a test facility for future accelerators, namely CLiC (Compact Linear Collider).

1.2.1. The LHC

The LHC [5] project was proposed in the 1980's and started operation in 2008. It provides proton-proton collisions as well as ion-ion and ion-proton collisions at unprecedented energy and intensity to its four large experiments. Shortly after the startup a faulty connection between two superconducting bending magnets required a major intervention until 2009 [6]. The LHC was restarted at an energy of 3.5 TeV per beam providing collisions in 2010 and 2011. In 2012 the beam energy was increased to 4 TeV. Over the first three years of operation it delivered 29 fb^{-1} of proton-proton collisions to the two multipurpose detectors, ATLAS and CMS, at a peak luminosity of $7.7 \cdot 10^{33}\,\mathrm{cm}^{-2}\mathrm{s}^{-1}$ which lead to the discovery of the so-called Higgs Boson.

In 1994 the CERN council approved the LHC project which re-uses the tunnel built for the LEP[1] accelerator. The 26.7 km long tunnel with eight straight sections and eight arcs is inclined at 1.4 % and is located between 45 m and 170 m below the surface to take advantage of the geological conditions. Given the size of the accelerator, the LHC is designed to reach collision energies of 14 TeV and luminosities L of up to $L = 10^{34}\,\mathrm{cm}^{-2}\mathrm{s}^{-1}$ where L is defined by beam parameters only and can be written as:

$$L = \frac{N_b^2 n_b f_{\mathrm{rev}} \gamma_r}{4\pi \epsilon_n \beta^*} F \tag{1.2.1}$$

[1] **L**arge **E**lectron-**P**ositron Collider

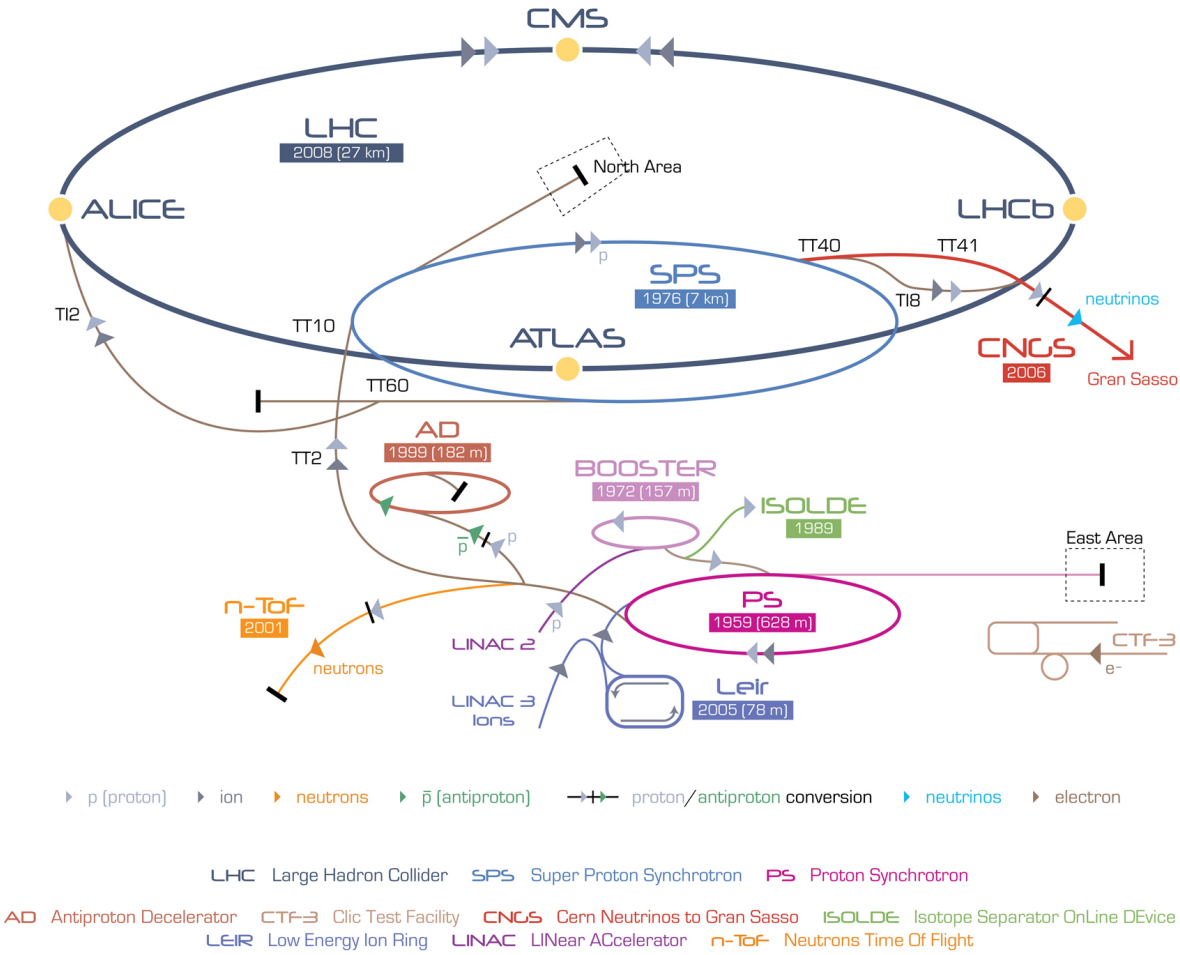

Figure 1.2.: The CERN accelerator complex [4]. Not to scale.

This assumes the ideal case of identical round beams. N_b stands for the number of particles per bunch, n_b for the number of bunches in the machine, f_{rev} for the revolution frequency, γ_r for the relativistic gamma factor, ϵ_n for the normalized transverse beam emittance (beam dimensions) and β^* for the beta function at the collision point. To reduce parasitic collisions in the straight sections in the experiments, the beams cross at an angle Θ_c. That angle and the RMS[1] of the bunch length σ_z as well as the transverse RMS beam size σ^* in the interaction point define the geometric luminosity reduction factor F[2].

Since the luminosity scales linearly with the number of particles per beam the use of anti-proton beams is excluded. Thus, the LHC is the first ring collider to accelerate two counter-rotating particle beams instead of one particle and one anti-particle beam. To

[1] **R**oot **M**ean **S**quare

[2] $F = \sqrt{1 + \left(\frac{\Theta_c \sigma_z}{2\sigma^*}\right)^2}$ [5].

reach 14 TeV center of mass energy in that given radius a nominal dipole field of 8.33 T is required for the bending magnets. Those are designed as super conducting NbTi twin-bore magnets, operated in a cryogenic environment, cooled with 1.9 K superfluid helium.

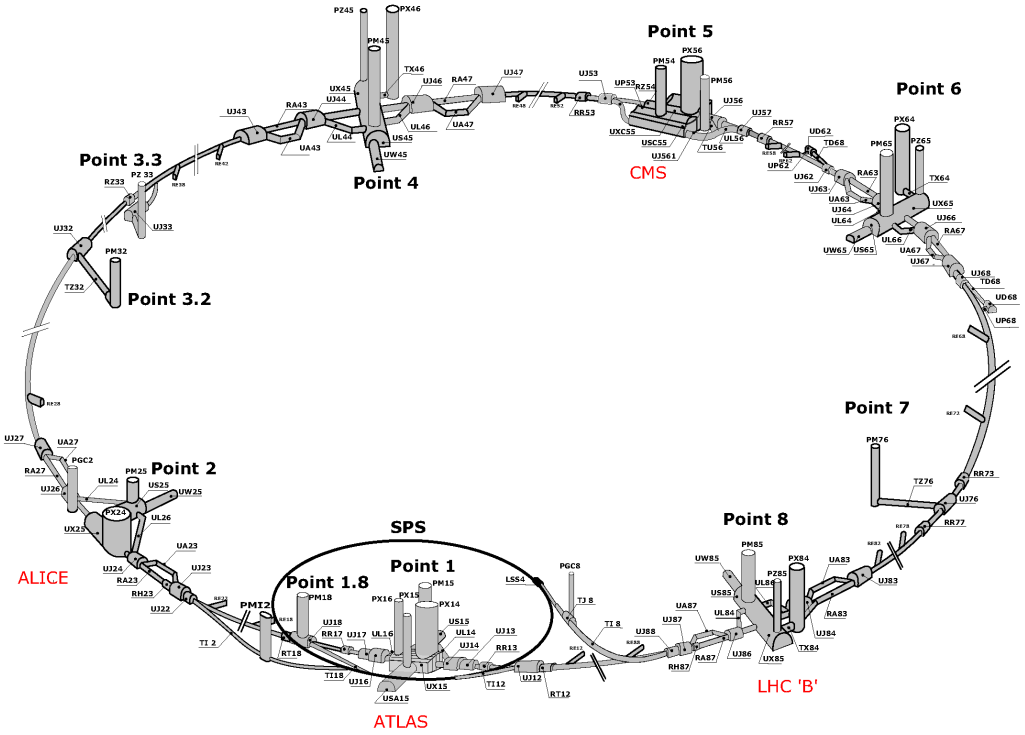

Figure 1.3.: Schematic layout of the LHC underground facilities and access points [7].

A schematic layout of the LHC underground facilities and access points is shown in Figure 1.3. The accelerator is divided into eight independent sections for cryogenics and magnet powering with corresponding access points. The beams are injected in Point 1 towards Point 2 (Beam 1, clockwise) and between Point 1 and Point 8 towards Point 8 (Beam 2, anticlockwise). The radio frequency acceleration section is located in Point 4 hosting independent cavities for the two beams. The beams cross vertically in the experiments at Point 1 (ATLAS) and 8 (LHCb[1]) and horizontally in Point 2 (ALICE[2]) and 5 (CMS). The beam dump region is located in Point 6. Point 3 and 7 are equipped with collimators for beam cleaning. Nominal beam conditions foresee 2 808 bunches with $1.15 \cdot 10^{11}$ protons per bunch and 25 ns spacing. With the help of different filling patterns and optics the experiments can be supplied with varying luminosities in a global range from $10^{26}\,\mathrm{cm^{-2}s^{-1}}$ to $10^{34}\,\mathrm{cm^{-2}s^{-1}}$ for protons and from $10^{24}\,\mathrm{cm^{-2}s^{-1}}$ to $10^{27}\,\mathrm{cm^{-2}s^{-1}}$ for ion runs, respectively.

[1] **LHC-b**eauty
[2] **A L**arge **I**on **C**ollider **E**xperiment

1.2.2. The ATLAS Experiment

The ATLAS [8] Experiment is one of the four large LHC experiments and within those one of the two multipurpose detectors. It is built to measure the various particles originating from proton-proton as well as ion-ion collisions provided by the LHC, covering as much solid angle around the interaction point as possible. Thus, its design is forward-backward symmetric with a cylindrical shape. The ATLAS Detector is 25 m in diameter, 44 m long and weighs 7 000 t. A schematic view of the main sub-systems is shown in Figure 1.4. The eightfold symmetry of the detector is driven by its ex-

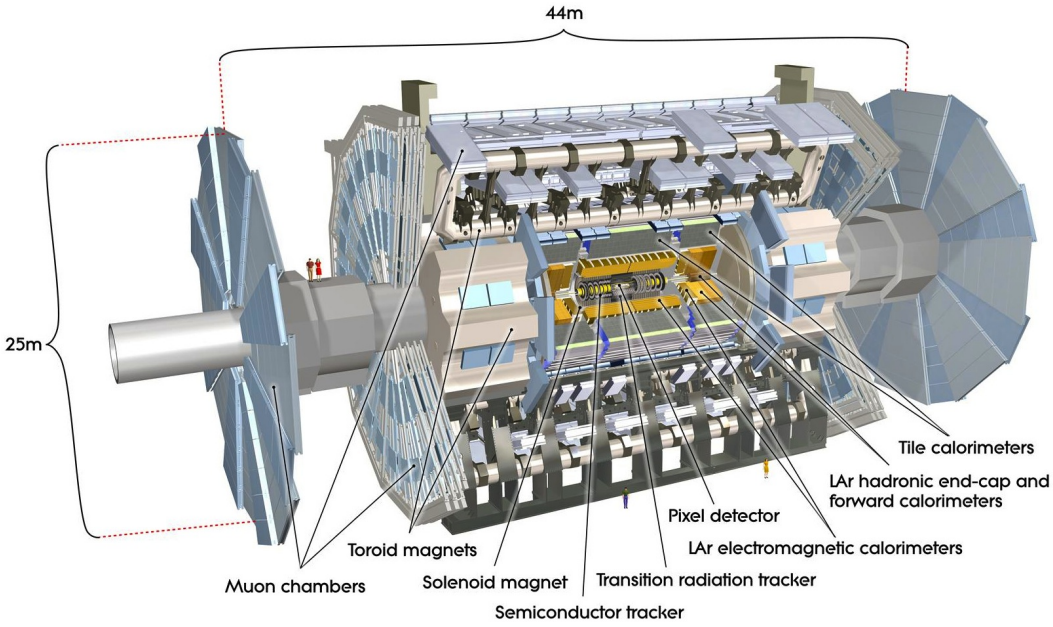

Figure 1.4.: Sectional view of the ATLAS Detector [8].

ceptional magnetic field configuration. A 2 T solenoid, which extends over a length of 5.3 m with a diameter of 2.5 m, is surrounding the inner tracking detectors while the muon spectrometer is immersed in a toroidal field. The barrel toroid provides 1.5 to 5.5 Tm of bending power in the pseudorapidity range $0 < |\eta| < 1.4$, and the end-cap toroids approximately 1 to 7.5 Tm in the region $1.6 < |\eta| < 2.7$. The bending power is lower in the transition regions where the two magnets overlap ($1.4 < |\eta| < 1.6$). This allows the measurement of muon momenta independently in two perpendicular planes. All sub-detectors are divided into a central part, called barrel, and a forward part on each side of the barrel, called end-cap.

The Inner Detector consists of three different tracking systems, the Pixel Detector, the SCT[1] and the TRT[2]. The Pixel Detector will be described in detail in Chapter 2. The

[1] **S**emi**c**onductor **T**racker
[2] **T**ransition **R**adiation **T**racker

SCT consists of four micro-strip silicon detector layers in the barrel and nine disks in each end-cap region. The TRT is made out of 73 straw planes in the barrel and 80 straw planes in each end-cap region. It provides around 36 hits per track.

Two kinds of sampling calorimeters are located outside the solenoid volume. The electromagnetic calorimeter uses liquid Argon (LAr) as active medium with accordion-shaped copper electrodes and lead absorber plates over its full coverage. The hadronic calorimeter barrel is made up of alternating steel and scintillating tiles. The scintillators are read out on both sides by wavelength shifting fibers into two separate photomultiplier tubes. In the end-caps copper plates are used as absorbers and the LAr acts as active medium. A dedicated forward calorimeter uses LAr as active medium with copper absorbers for electromagnetic showers, followed by tungsten absorbers for hadronic showers.

The muon system combines trigger elements (resistive plate chambers and thin gap chambers) with high precision tracking detectors (monitored drift tubes and cathode strip chambers). In the barrel region three layers are mounted cylindrically around the beam axis in the air-core of the toroid magnets, while the three layers in the transition and end-cap region are installed perpendicular to the beam in the magnetic field of the toroid end-caps and outside the magnets.

1.2.3. The CMS Experiment

Just like the ATLAS Experiment the CMS [9] Detector is a multi-purpose experiment searching for new physics at the LHC. The main components are the same as for ATLAS: A cylindrical setup consisting of a tracking system close to the beam pipe, an electromagnetic and a hadronic calorimeter in the middle, a strong magnetic field and muon chambers on the outside. However, the realization is very much different in the two experiments to limit systematical uncertainties and to ensure two independent measurements of the same processes. CMS's core part is the 3.8 T superconducting solenoid magnet. It is 13 m long with an inner diameter of 5.9 m. The return field is large enough to saturate 1.5 m of iron which allows four dedicated muon detection stations inside the yoke. The tracking and calorimetry systems are installed inside this magnet. The experiment is 21.6 m long with a diameter of 14.6 m and a total weight of 14 000 t. A schematic view of the main sub-systems is shown in Figure 1.5.

The tracking system is 5.8 m long with a diameter of 2.6 m. It consists of 3 layers of silicon pixel detectors with analog readout and 10 layers of microstrip silicon detectors. The electromagnetic calorimeter is made of lead tungstate ($PbWo_4$) crystals in which the scintillation light is read out by silicon avalanche photodiodes in the barrel regions and vacuum phototriodes in the end-cap region.

The hadronic calorimeter is realized by alternating brass and scintillator layers. Via wavelength shifting fibers the light is converted and then transported to novel hybrid photodiodes which can also be operated in high axial magnetic fields. In the forward

region an additional iron quartz calorimeter is installed to increase the geometrical coverage for transverse energy measurements.

The muon system uses aluminum drift tubes in the barrel region and cathode strip chambers in the end-cap region, complemented by resistive plate chambers.

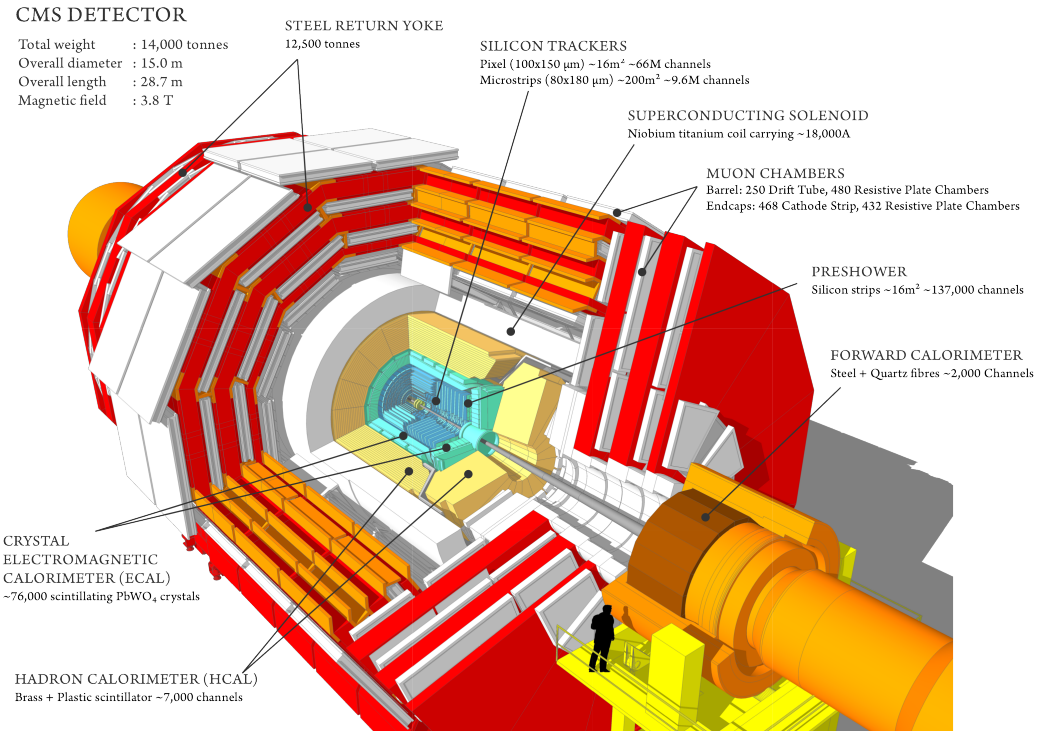

Figure 1.5.: Sectional view of the CMS Detector [10].

1.2.4. The ALICE Experiment

The ALICE [11] Experiment is a more specialized detector for probing dense media of strongly interacting particles. It focusses on the study of primordial matter produced in quark-gluon plasmas which can be formed by colliding heavy ions, mostly lead ions in the LHC. The physics program also includes studies of lighter ion collisions and proton-nucleus collisions. During the main operation mode of the LHC, i.e. proton-proton collisions, reference data is taken. Due to its focus on strong interactions it is complementary to the other three big LHC experiments.

The ALICE Experiment is 26 m long and weighs 10 000 t. As can be seen from the schematic view in Figure 1.6 it consists of two main parts, a cylindrical detector part inside the solenoid magnet and a forward muon arm. The 16 m diameter magnet is re-used from the L3 Experiment at LEP with a magnetic field strength of 0.5 T. Driven by the physics requirements ALICE combines various ultra light tracking detectors

(pixel, silicon drift and microstrip detectors as well as a time projection chamber) producing up to 150 three-dimensional space points. Three different types of particle identification detectors, namely time-of-flight, ring imaging Cherenkov and transition radiation detectors are used. In addition two electromagnetic calorimeters for photon and jet measurements as well as a forward muon arm for the study of heavy-quark resonances have been installed. Most of the sub-detectors cover a small solid angle.

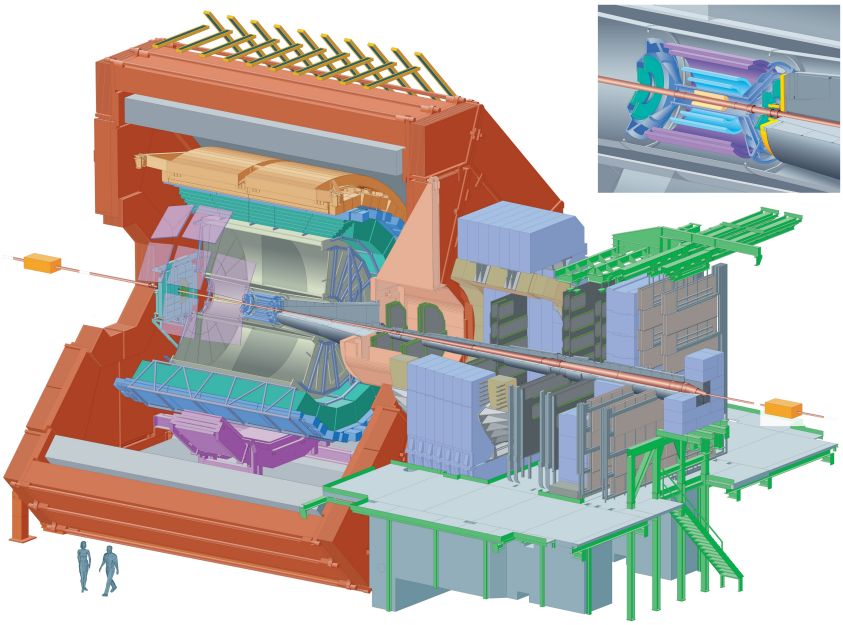

Figure 1.6.: Sectional view of the ALICE Detector [11].

1.2.5. The LHCb Experiment

The second specialized detector is the LHCb [12] Experiment. Within the Standard Model of particle physics the asymmetry between matter and antimatter is explained by the CP violating weak interaction. However, the weak interaction alone cannot account for the amount of matter that is observed in the universe.

The LHCb Experiment investigates rare decays of heavy hadrons containing b or c quarks to search for new sources of the asymmetry between matter and antimatter. A schematic view of the detector is shown in Figure 1.7. Contrary to the two multi-purpose LHC experiments, ATLAS and CMS, the LHCb Detector is not forward-backward symmetric but is built as a single-arm spectrometer covering an angle of $\pm 250\,\mathrm{mrad}$ vertically and $\pm 300\,\mathrm{mrad}$ horizontally with respect to the beam axis. The high precision vertex locator (VELO) is located very close to the interaction point. In order to prevent damages of the detector during non-stable beam conditions in the LHC, the VELO is retractable inside a secondary vacuum. Further downstream stands

another micro-strip silicon tracker, Tracker Turicensis (TT). It is followed by a warm dipole magnet which induces a horizontal spread of incoming particle depending on their charge and momentum. Behind the magnet three more tracking systems, T1-T3, measure the particles' trajectories using micro-strip detectors close to the beam and straw-tubes in the outer regions.

Right behind the tracking stations RICH[1] detectors separate pions and kaons originating from B meson decays. For energy measurements and further particle identification a scintillator pad detector (SPD) and pre-shower (PS), followed an electromagnetic and a hadronic calorimeter are used. The electromagnetic calorimeter is comprised of lead while the hadronic calorimeter uses iron as absorber material. They are both mounted alternating with scintillating tiles as active medium. Both calorimeters are segmented with lateral variation to fit the beam properties and read out via wavelength shifting fibers connected to photomultiplier tubes. One muon station is placed upstream the calorimeters, the other four downstream, interleaved with iron absorbers to select penetrating muons. The muon detectors are built as multi-wire proportional chambers apart from the inner region of M1, where triple-GEM[2] detectors are installed.

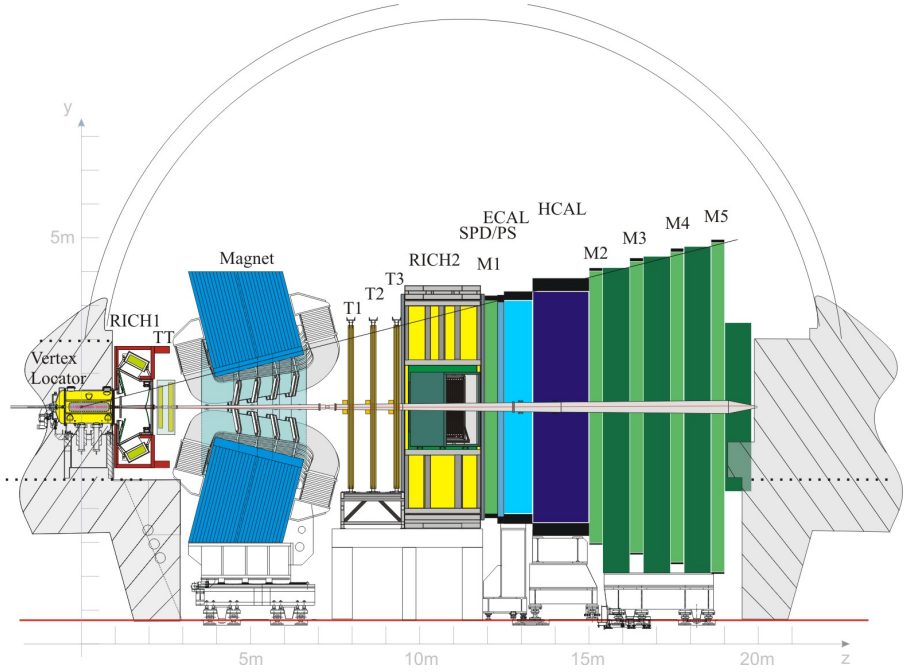

Figure 1.7.: Sectional view of the LHCb Detector. The LHC beams travel in opposite directions along the central axis of the experiment colliding in the center of the Vertex Locator [12].

[1] **R**ing **I**maging **CH**erenkov
[2] **G**as **E**lectron **M**ultiplier

1.2.6. The LHC Upgrades

Already during the construction phase several possible upgrade scenarios are considered. Details on upcoming experiments and searches are planned based on recent discoveries and measurements performed so far. Since experiments at this scale are huge and cost intensive, usually several upgrade scenarios are discussed and realized to fully exploit all capabilities of the scientific facilities before requiring entirely new technologies and concepts. In the case of the LHC three major upgrades are foreseen. They will be described in the following pages.

Phase 0

In the first long shutdown (LS1) of the LHC, the main task was the strengthening of the 10 170 superconducting magnet interconnections to enable the operation at the design energy of 7 TeV per beam. In total 18 bending magnets have been replaced. Vacuum, cryogenics and electronics systems have been consolidated. In addition, other upgrades and renovation works on all (pre-)accelerators and experiments, e.g. on collimation, radiation tolerance of electronics and tunnel ventilation systems, have been performed. First proton collisions are planned for May 2015. In the upcoming Run 2 about 100-120 fb^{-1} shall be delivered to the two high-luminosity experiments.

The major changes in the ATLAS Experiment concern the Pixel Detector. Those will be described in more details in Sections 2.5.1 and 2.5.2. The additional pixel layer which has been installed recently will be depicted in Chapter 3. Furthermore, a new Inner Detector cooling and end-cap extension muon chambers have been installed. The central first trigger level and the magnet cryogenics have been upgraded and a specific neutron shielding has been added.

Phase 1

Run 2 is foreseen to last until mid 2018 until the second long shutdown (LS2) which is scheduled for one and a half years. During that shutdown machine improvements are planned to ensure reliable operation at a luminosity of $2 \cdot 10^{34}\,\mathrm{cm}^{-2}\mathrm{s}^{-1}$ in Run 3. That requires more flexibility for beam interactions in ATLAS and CMS Detectors which is realized by installing new low-β quadrupoles with 120 mm aperture instead of 70 mm as they are used now [13]. Furthermore, a new linear accelerator is already under construction (LINAC 4), foreseen to replace LINAC 2 as the first proton injector in CERN's accelerator chain in the Phase 1 upgrade. The major improvements are increased output energy of 160 MeV (compared to 50 MeV from LINAC 2) and increased beam brightness to deliver higher intensity beams for the required LHC luminosity upgrades.

The main focus for the ATLAS Detector in LS2 will be the replacement of the small wheel of the forward muon spectrometer then using MicroMegas and strip Thin Gap

Chambers, the integration of a high precision calorimeter trigger at the first trigger level (Level-1), the establishment of a Fast TracKing (FTK) for the second trigger level (Level-2) and the installation of a proton detector, ATLAS Forward Physics (AFP), at 210 m distance from the interaction point on both sides of the ATLAS Detector.

Phase 2 - HL-LHC

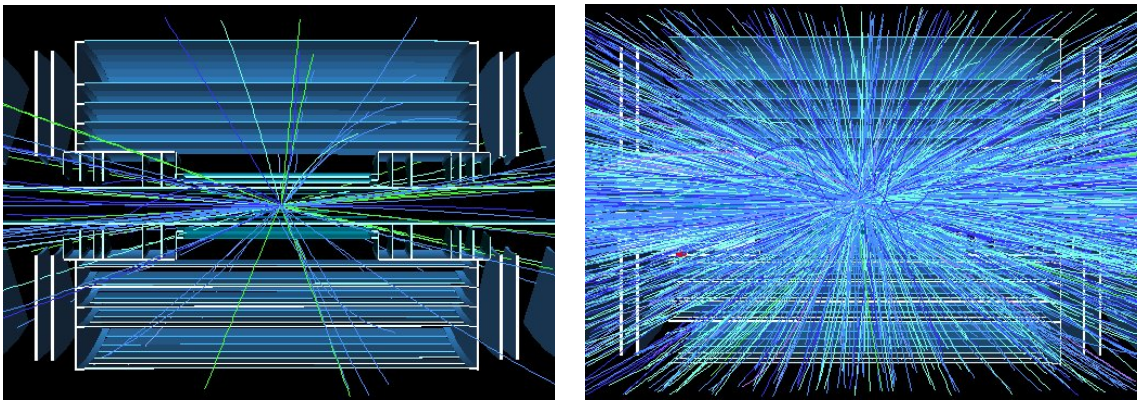

(a) (b)

Figure 1.8.: Simulation of (a) 5 pile up events and (b) 400 pile up events in the ATLAS Pixel and SCT Detectors in the HL-LHC scenarios [14].

It is the goal to collect around $300\,\mathrm{fb}^{-1}$ of data until the High-Luminosity-LHC upgrade. This machine upgrade is scheduled for 2023 until mid 2025 during the third long shutdown (LS3). The major interventions, namely the replacement of the interaction region quadrupole magnets (inner triplets) and installation of 11 T bending magnets in Nb_3Sn technology, upgrades of collimation regions and cryogenics, installation of crab cavities and new machine protection parts as well as cold powering, will affect more than 1.2 km of the LHC. The targeted luminosity will be $5 \cdot 10^{35}\,\mathrm{cm}^{-2}\mathrm{s}^{-1}$.

At the same time all experiments will be significantly upgraded to cope with the expected increase in luminosity and hence collision data as shown in Figure 1.8. In the ATLAS Experiment the entire Inner Detector will be replaced by an new Inner TracKer (ITK). The most challenging requirements are the granularity needed to resolve up to 200 interactions in one collision while demanding a detector occupancy of less than 1 % along with the high radiation environment ($2 \cdot 10^{16}\,\mathrm{n_{eq}cm}^{-2}$) while further reducing the tracker's radiation length. Also the overall silicon detector covered area will be significantly increased to almost $200\,\mathrm{m}^2$. Thereby, the number of read out channels will increase by one order of magnitude. To properly prepare the entire detector for the difficult HL-LHC environment upgrades on calorimeter electronics, muon trigger systems, Level-1 track trigger and changes to the forward calorimeters are being evaluated.

1.3. Particle Detection Techniques

In this section the basic principles of particles interacting with matter will be discussed. Furthermore, detection techniques using solid state devices will be explained and radiation effects depicted. The main focus here will be on silicon detectors, which are the most common tracking devices in high energy physics applications such as the LHC experiments. For instance two (Pixel, SCT) out of three sub-detectors of the ATLAS Inner Detector are made up of silicon modules. The observable macroscopic radiation effects in silicon sensors will be demonstrated in Section 2.4 using the example of the 3-Layer ATLAS Pixel Detector after three years of operation.

1.3.1. Energy Loss in Matter

For the application in collider experiments' tracking systems, high energetic charged particles need to be detected while depositing only a small amount of energy in order to not significantly distract their trajectory. That is essential for momentum measurements inside a magnetic field whereas calorimeters with a high atomic number Z are used to fully stop those particles and thus determine their energies. Thereby, the different particles interact according to their coupling forces. Here, the electromagnetic interaction of photons and charged particles will be discussed as those are used in the measurements presented in the following chapters. More detailed information on particle detection techniques can be found in [15].

For photons interacting with matter there are three effects to be mentioned. The first one is called the Photo-electric effect where a photon is entirely absorbed by an electron bound in the atomic shell, which is then kicked off in case of a photon energy higher than the electrons binding energy. The second effect is Compton scattering at which the incoming photon interacts with an atomic shell electron inelastically and is converted into a photon with lower kinetic energy. A third way of energy conversion is pair production. The incoming photon can convert its energy into an electron-positron pair through interaction with the nucleus or even with a surrounding electron given enough initial kinetic energy of the photon, i.e. twice the resting energy of an electron or four times the energy, respectively. In order to absorb a photon in silicon of just a few hundred μm thickness, comparatively low energetic γ's, e.g. $< 160\,\text{keV}$ from ^{241}Am sources, are used for sensor functionality tests and calibration measurements. Results from source measurements will be presented in Section 3.4.

For charged particles there are also three fundamental interaction processes caused by the electromagnetic force. One is ionization of the passed material, the second one is Cherenkov radiation which occurs in case of a particle passing a medium faster than its specific speed of light and finally transition radiation which is emitted if the particle passes an inhomogeneous medium. Quantitatively the energy loss per track length of a traversing heavy charged particle caused by these effects is accounted for in the Bethe-Bloch formula [15]:

$$-\frac{\mathrm{d}E}{\mathrm{d}x} = 2\pi N_\mathrm{a} r_\mathrm{e}^2 m_\mathrm{e} c^2 \rho \frac{Z z^2}{A\beta^2}\left[\ln\left(\frac{2m_\mathrm{e}\gamma^2\nu^2 W_\mathrm{max}}{I^2}\right) - 2\beta^2 - \delta(\beta\gamma)\right] \tag{1.3.1}$$

with

$$\begin{aligned}
\frac{\mathrm{d}E}{\mathrm{d}x} &: \text{mean energy loss per track length}\\
N_\mathrm{a} &: \text{Avogadro's number: } 6.022\cdot 10^{23}\,\mathrm{mol}^{-1}\\
r_\mathrm{e} &: \text{classical electron radius: } 2.817\cdot 10^{-13}\,\mathrm{cm}\\
m_\mathrm{e} &: \text{electron mass: } 511\,\mathrm{keV/c}\\
\rho &: \text{density of absorbing material: } 2.33\,\frac{\mathrm{g}}{\mathrm{cm}^3} \quad \text{(for silicon)}\\
I &: \text{mean excitation potential: } 173\,\mathrm{eV} \quad \text{(for silicon)}\\
Z &: \text{atomic number of absorbing material: } 14 \quad \text{(for silicon)}\\
A &: \text{atomic weight of absorbing material: } 28 \quad \text{(for silicon)}\\
z &: \text{charge of traversing particle in units of e}\\
\beta &: v/c \text{ of the traversing particle}\\
\gamma &: \frac{1}{\sqrt{1-\beta^2}}\\
\delta &: \text{density correction}\\
W_\mathrm{max} &: \text{maximum energy transfer in a single collision}
\end{aligned}$$

The mean excitation potential I is essentially the mean orbital frequency, averaged over all bound electron states of the material, times Planck's constant h. However, since the averaging of the oscillation frequencies on the atomic level bears different uncertainties for various materials, the actual values have usually been re-calculated from $\mathrm{d}E/\,\mathrm{d}x$ measurements. An example plot of the measured energy dependent specific ionization using the 3-Layer ATLAS Pixel Detector is shown in Figure 2.6(b). The density correction is added to account for polarization effects inside the traversed material caused by the incident particle. It thus scales only with the particle's velocity and not with its mass. Generally, particles with a $\beta\gamma > 3$ are called MIP[1]s since that energy corresponds to a local minimum and at higher energies the energy deposition only increases slightly. In the case of rather thin silicon detectors the energy deposition is not gaussian but follows a non-symmetric so-called Landau distribution with a tail towards higher energy transfers due to contributions from secondary electrons (so-called δ-electrons) that can continue to ionize the material. The values for silicon stated in the list above are taken from [16].

[1] **M**inimum **I**onising **P**article

1.3.2. Tracking Devices

Nowadays high energy physics experiments are required to cope with high collision rates and particle fluxes. In the above mentioned fashion electron hole pairs are created in solid state detectors. These electrical signals usually are collected on one side of the detector, then shaped and amplified for further processing. Here, two technologies will be introduced. First, the use of silicon as sensor will be motivated and eventually insulating materials, in this case diamond sensors, will be described as these are the two technologies relevant for the first upgrade of the ATLAS Pixel Detector that will be described in more detail in Chapters 2 and 3.

Silicon is the favored material in semiconductors industry and thus the most feasible option for large scale vertex identification in the innermost layers of the experiments. It is a semiconducting element from the fourth main group of the periodic table with a band gap energy of 1.21 eV. Introduction of impurities through neighboring main group elements provides additional charge carriers in the valence band or the conduction band, respectively. Silicon doped with atoms from the fifth main group has a surplus of negative charge carriers and is thus called n-doped. Doping with atoms from the third main group leaves additional positive charge carriers and is therefore called p-doped. The working principle of a silicon sensor is based on the pn-junction, i.e. the transition region from n-doped to p-doped silicon. There the free charge carriers from the n-doped material combine with the empty spaces in the lattice and thus form a so-called depletion region. An incident particle creates electron-hole pairs in the depletion region (see Figure 1.9(a)). These start drifting in the sensor and can be separated by an externally applied electrical field. The second advantage of the electrical field is the growth of the depletion region as can be seen in Figure 1.9(b). The amount of HV[1]

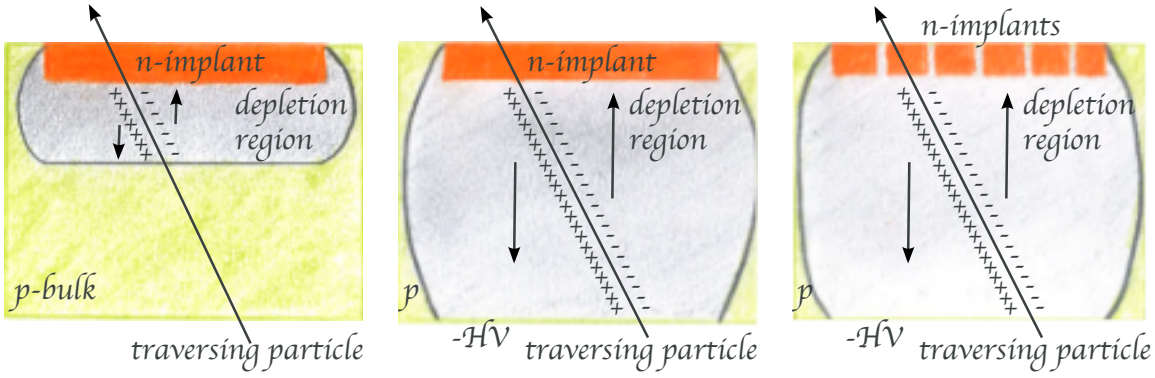

Figure 1.9.: Working principles of silicon detectors. (a) A simple pn-junction without external field, (b) a simple pn-junction with external field and (c) a segmented pn-junction with external field are shown.

[1]**H**igh **V**oltage, here: sensor bias

needed to fully deplete a sensor depends on its thickness, its material and eventually the level of radiation induced damages in the crystal lattice. In the following it will be referred to as depletion voltage. By segmenting the n-implants the spatial resolution of the particle trajectory can be improved (see Figure 1.9(c)). The spatial resolution of such a pixelated sensor depends on the dimensions of the segmentation, the efficiency of the charge collection, the amount of shared charged between neighboring pixels and eventually the threshold of the connected readout. A good first approximation for designing a sensor is given by only considering the segmentation width (pitch p) while omitting efficiency and readout effects. Assuming that only one pixel registers hits which happened half the pitch around its center, the average difference σ_{pos} between the actual hit position x_{hit} and the measured position x_{meas} can be calculated to:

$$\sigma_{\text{pos}}^2 = \frac{\int_{-p/2}^{p/2}(x_{\text{hit}} - x_{\text{meas}})^2 f(x_{\text{hit}})\,\mathrm{d}x_{\text{hit}}}{\int_{-p/2}^{p/2} f(x_{\text{hit}})\,\mathrm{d}x_{\text{hit}}} \tag{1.3.2}$$

$$= \frac{\int_{-p/2}^{p/2} x_{\text{hit}}^2\,\mathrm{d}x_{\text{hit}}}{\int_{-p/2}^{p/2} 1\,\mathrm{d}x_{\text{hit}}} = \frac{p^2}{12} \tag{1.3.3}$$

and thus

$$\sigma_{\text{pos}} = \frac{p}{\sqrt{12}} \tag{1.3.4}$$

This assumes the particle distribution $f(x_{\text{hit}})$ to be homogeneously 1 over the entire pixel and its center in the middle of the coordinate system. More details can be found in [15].

Another advancing base material for solid state particle tracking sensors is CVD[1] diamond with metal contacts on both sides. Diamond is an insulator with a band gap energy of 5.5 eV and therefore contains much less free charge carriers which results in a smaller leakage current. However, only roughly 36 electron-hole pairs per micrometer are created by an incident particle which is less than half of the charge carriers produced in silicon [17]. Thus, it requires a higher sensor bias and more sensitive readout. The main advantage over silicon is the higher thermal conductivity and its inherent radiation hardness. Due to the higher thermal conductivity no excessive cooling is required. Because of the higher band gap energy displacement effects induced by incident particles have a much lower impact on the diamond's properties. Thus, diamond sensors are used for applications in high radiation environments, e.g. very close to the primary beam as in the ATLAS BCM[2] and its successor DBM[3] (see Section 2.5.2).

[1] **C**hemical **V**apor **D**eposition
[2] **B**eam **C**onditions **M**onitor
[3] **D**iamond **B**eam **M**onitor

1.3.3. Radiation Damages in Silicon Detectors

Particles traversing silicon, depositing energy in the above mentioned fashion, leave the lattice unaffected, whereas the so-called NIEL[1] effects damage the crystal and leave impurities as shown in Figure 1.10. If an incident particle transfers an energy of at least 15 eV onto an atom it can be kicked out of its lattice position [18]. This so-called PKA[2] leaves its original position (vacancy) and can cause ionization or further displacement damages until it finally rests as an interstitial atom. Depending on the energy regions point defects but also cluster damages are possible. To quantify the amount of radiation a material is exposed to one normalizes the fluence in units of 1 MeV neutrons, Φ_{eq}, and defines an energy and particle type dependent hardness factor κ for scaling the actual fluence Φ_{irr}:

$$\Phi_{\text{eq}} = \kappa \cdot \Phi_{\text{irr}} \tag{1.3.5}$$

This approximation assumes that the main damage is caused by the PKA. While the interactions of the incident particle and the PKA are well understood [18], the macroscopic effects are hard to predict. However, it was found that the paramount observables are a change in the effective doping concentration of the material, an increased leakage current and a decrease in collected charge at the sensors' electrodes. The measured effective impurity concentration depending on the fluence is shown in Figure 1.11(b). As can be seen, the effective doping concentration inverts for the common FZ[3] based silicon sensors at a radiation fluence of around $3 \cdot 10^{13}\,\text{n}_{\text{eq}}\text{cm}^{-2}$. The different growth mechanisms for the depletion zones before and after type inversion of an n-bulk sensor, as it is used in the ATLAS Pixel Detector, are qualitatively sketched in Figure 1.11(a) and Figure 1.11(c) respectively. The effective doping concentration has an influence on the depletion voltage. Thereby, the leakage current scales linearly with the radiation fluence the sensor was exposed to. Finally, charge carriers can be trapped in the radiation induced impurities which yields in a reduced charge collection. Hence, during prototyping runs all these aspects have to be investigated to make sure the sensors can endure the conditions foreseen in the particular experiments.

The mechanism introduced above concerns bulk damages. However, there are also surface effects induced by ionization that affect primarily the silicon dioxide (SiO_2) layers. Due to their higher mobility electrons move rapidly to the electrodes while the holes remain and thus charge up the SiO_2 layer close to the SiO_2-Si boundary surface. Surface effects can be minimized by proper sensor design [18] and are thus mostly negligible in recent detectors.

The various defects, however, are not necessarily stable. Thermally induced movements can lead to recombination of impurities (beneficial annealing) but also to further enlargement of defects (reverse annealing) due to the healing of other regions. For detector

[1] **N**on **I**onising **E**nergy **L**oss
[2] **P**rimary **K**nock-on **A**tom
[3] **F**loat**Z**one

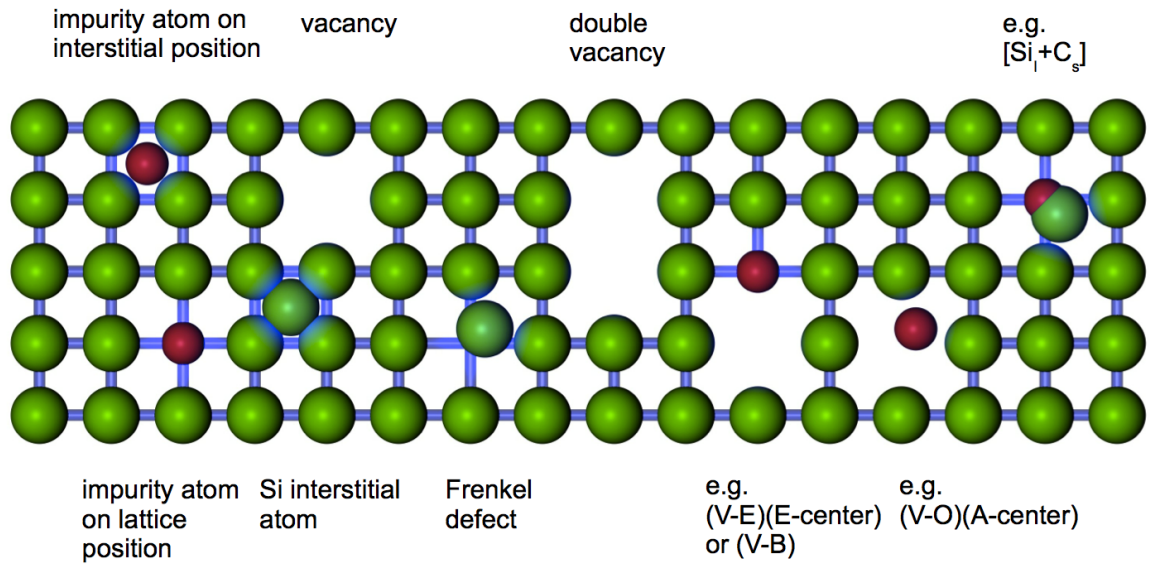

Figure 1.10.: Sketch of possible lattice damages induced by non-ionizing energy losses of traversing particles. Original taken from [18], modified in [19].

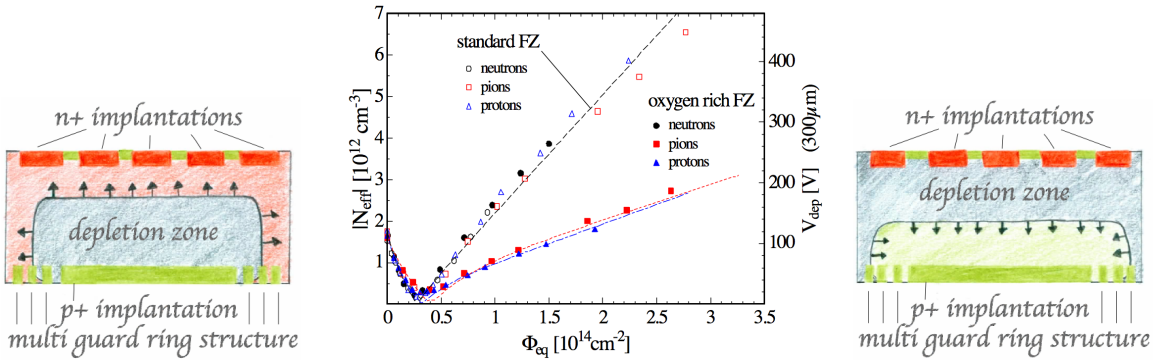

(a) (b) (c)

Figure 1.11.: (b) Effective impurity concentration depending on the fluence [20] and a sketch of the depletion zone growth principle (a) before and (c) after type inversion. Originals taken from [21] and modified.

design it is thus important to quantify the temperature and exposure time in order to improve its properties and life time. Monitoring of silicon sensor leakage currents as well as changes in depletion voltage using the example of the 3-Layer ATLAS Pixel Detector will be presented in Section 2.4.

Just get my me overdose
I'll try to stay awake
The silent way, the silent way.
- Rabia Sorda

Chapter 2

The ATLAS Pixel Detector

The ATLAS Pixel Detector [22] is the innermost detector of the ATLAS Experiment [8] at the Large Hadron Collider at CERN. The detector provides hermetic coverage up to $|\eta| < 2.5$ with three cylindrical layers and three layers (disks) of pixel detectors located in forward and backward direction. It consists of approximately 80 million pixels that are individually read out via FE-I3[1] [23] readout chips bump-bonded to 1744 n^+-in-n silicon sensors. Results from the successful operation of the Pixel Detector at the LHC and its status after three years of operation have been presented in [24], including monitoring, calibration procedures and detector performance.

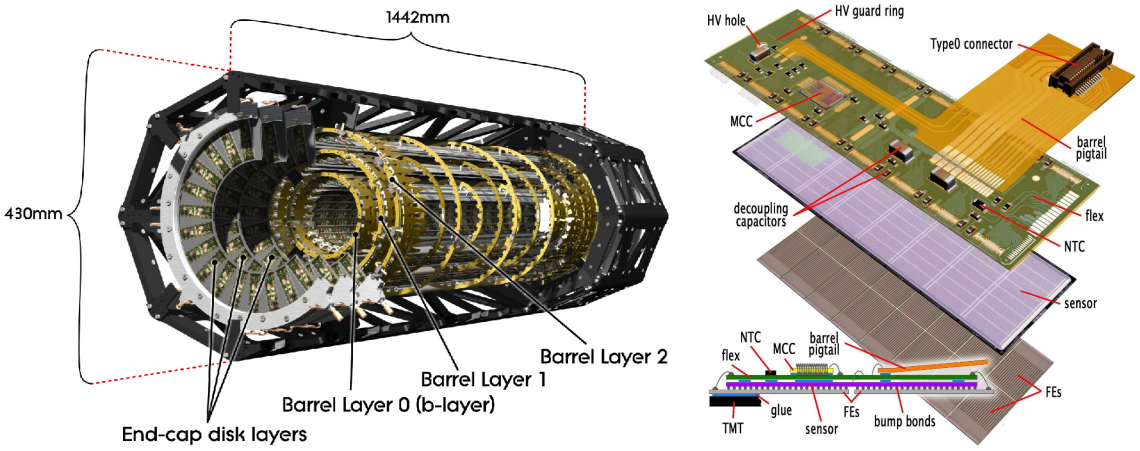

(a) (b)

Figure 2.1.: (a) Perspective view of the ATLAS Pixel Detector and a (b) Pixel module [21].

The record breaking instantaneous luminosities of $7.7 \cdot 10^{33}\,\mathrm{cm}^{-2}\mathrm{s}^{-1}$ recently surpassed at the Large Hadron Collider generate a rapidly increasing particle fluence in the ATLAS Pixel Detector. In 2010 - 2012 (Run 1) $29\,\mathrm{fb}^{-1}$ of data have been collected. As the radiation dose accumulates, first effects of radiation damage are now observable in

[1] **F**ront**E**nd chip - Version 3

the silicon sensors. A regular monitoring program has been conducted and reveals an increase in the silicon leakage current, which is found to be correlated with the rising radiation dose recorded by independent sensors within the inner detector volume. In the longer-term crystal defect formation in the silicon bulk is expected to alter the effective doping concentration, producing type-inversion and ultimately an increase of the voltage required to fully deplete the sensor. Here, some details and an update on the current status will be given as a context for the coming chapters.

2.1. Detector Design

The ATLAS Pixel Detector is designed to ensure tracking based on three hits for each particle traversing at a pseudo-rapidity[1] up to $|\eta| < 2.5$ in order to find primary and secondary vertices in the ATLAS Experiment. In total 1744 modules, overlapping in z and $r\varphi$ to reduce the inactive area fraction, have been installed. They are arranged in three layers in the barrel region (at nominal radii of 50.5, 88.5 and 122.5 mm) and three disks at the extremities. The detector was designed to withstand particle radiation up to a fluence of 10^{15} 1 MeV n_{eq} cm^{-2} corresponding to a dose of 500kGy (50Mrad).

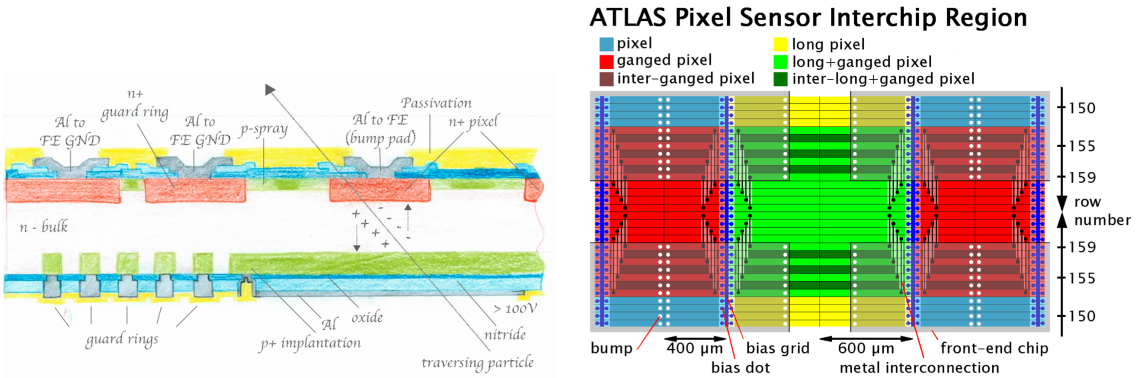

(a) (b)

Figure 2.2.: (a) Schematic partial cross section of the ATLAS Pixel Sensor and (b) schematic of the inter chip region [21].

The basic unit of the Pixel Detector is a module (see Figure 2.1(b)). It consists of one sensor tile ($\sim 2 \times 6.3\,cm^2$), 16 readout chips, a Module Controller Chip and a flex hybrid to access the output signals via the so called PP0 cables. The sensors were produced at CiS[2] and ON[3] using 250 μm thick n^+-in-n planar technology with a regular pixel size

[1] spatial coordinate describing the angle of a particle relative to the beam axis. It is defined as $\eta \equiv -\ln[\tan(\theta/2)]$, where θ is the angle between the particle three-momentum p and the positive direction of the beam axis

[2] **C**ompetence **i**n **S**ilicon, Forschungsinstitut für Mikrosensorik und Photovoltaik GmbH (Erfurt, Germany)

[3] **ON** Semiconductor Czech Republic a.s., Roznov, Czech Republic

of $50 \times 400\,\mu\text{m}^2$. The $250\,\mu$m thick lightly n-doped substrate contains highly n^+-doped pixel implantations on the front side and highly p^+-doped implantations on the back side, namely the HV pad and the guard rings. Since there are more than one readout chip connected to one sensor tile, the gaps between the FE[1]s have been bridged with long ($50 \times 600\,\mu\text{m}^2$) and ganged pixels (two sensor pixels connected to one read out pixel) respectively, as shown in Figure 2.2(b).

Limited by the power supplies, up to 600 V reverse bias voltage can be applied to the sensors. The amount of voltage needed to fully deplete the sensor depends mainly on the temperature and the irradiation level (see Section 2.4). The detection principle is shown in Figure 2.2(a). While traversing the silicon substrate the particle creates electron hole pairs that start drifting towards the electrodes (as described in Section 1.3.1). In this case the electrons are collected at the n^+ pixel implants which are directly connected to the readout pixels via bump bonds. To effectively isolate the individual pixel implants p-spray[2] was deposited in-between. 16 guard rings have been implemented all around the active area to successively reduce the voltage applied to the p^+ implantation on the back side of the sensor and thus prevent surface currents from flowing over the conductive cutting edge to the pixel side.

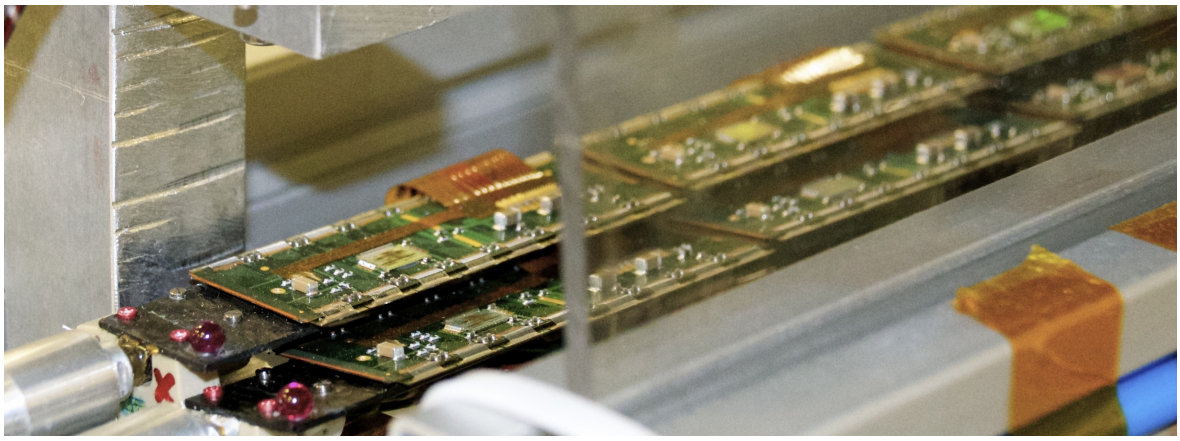

Figure 2.3.: Photograph of one ATLAS Pixel bi-stave located in a test stand in the CERN SR1 clean room.

The readout chips consist of 2880 individual pixels covering a sensor area of $7.2 \times 10.8\,\text{mm}^2$. In the digital part of the readout chips the individual pixel hit information is transferred to the end of column logic, then buffered on the end of chip logic and can be read out after arrival of a trigger signal. A Module Controller Chip (MCC) on top of each module combines the FE information and builds module events which will then be read out. The different layers operate at 40 up to 160 Mbit/s transmitting zero suppressed hit data. The modules are placed on carbon bi-stave support structures

[1] **F**ront**E**nd Electronic

[2] A p-implantation with a doping profile which features a higher doping concentration in the center

(13 on each stave) with integrated evaporative C_3F_8 cooling. A photograph of such a bi-stave is shown in Figure 2.3. The operational set temperature in the detector is $-20°$ C (2 bar) which results in an average module temperature of $-13°$ C.

2.2. Readout Chip Calibration

The read out chip (version FE-I3) hosts internal injection and calibration circuits to ensure a consistent response for all pixels. To effectively differentiate between noise and the actual signal a charge threshold can be set via a 7 bit DAC[1] (TDAC[2]). The discrimination digitalizes the analog sensor signal. In addition, the original amplitude is represented by the length of the output signal (ToT[3]). This can be adjusted by tuning the feedback current for each preamplifier using a 3 bit DAC (FDAC[4]). The FE-I3 chip diagram is shown in the next chapter in Figure 3.4(a). Here, the principle is just mentioned for the sake of completeness. A more detailed description of the circuits can be found in [22] and [23].

The qualitative dependence of the output signals of the preamplifier and the discriminator are presented in Figure 2.4(a). It appears that the length of the output signal depends on both, the set threshold and the feedback current. Thus, an iterated calibration procedure needs to be implemented. The threshold and the inherent noise can be derived from the discriminator activation curve as a function of the internally injected charge. An example of such an activation curve is shown in 2.4(b).

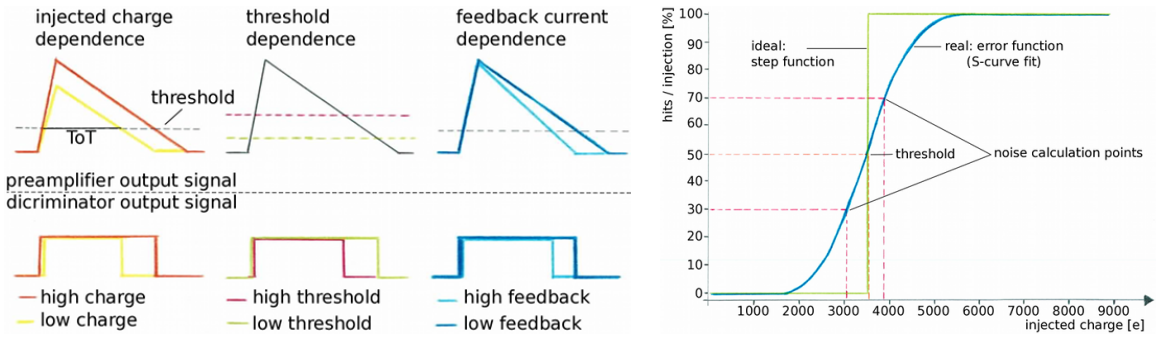

(a) (b)

Figure 2.4.: (a) The preamplifier and discriminator output signals of an ATLAS Pixel sensor cell for high and low charges and for different threshold and ToT settings, (b) S-curve resulting from convolution of a step function and a Gaussian pixel noise distribution.

[1] **D**igital to **A**nalog **C**onverter
[2] **T**hreshold **D**igital to **A**nalog **C**onverter
[3] **T**ime **o**ver **T**hreshold
[4] **F**eedback-current **D**igital to **A**nalog **C**onverter

In the ideal case it would correspond to a step function. However, the amplifier noise and sensor coupling capacitance cause an distortion of the actual charge response. That leads to a characteristic corresponding to a convolution of the ideal step function and a gaussian distribution caused by that noise, the complementary error function, which can be described with the so called s-curve fit $P_{\text{hit}}(Q)$ [25]:

$$P_{\text{hit}}(Q) = \Theta(Q - Q_{\text{thr}}) \otimes e^{\left(-\frac{Q^2}{2\sigma_{\text{noise}}}\right)} \tag{2.2.1}$$

$$= \frac{1}{2}\text{erf}\left(\frac{Q_{\text{thr}} - Q}{\sqrt{2}\sigma_{\text{noise}}}\right) \tag{2.2.2}$$

$$\text{with} \quad \text{erf} = \frac{2}{\sqrt{\pi}} \cdot \int_x^\infty e^{-t^2}\, \mathrm{d}t. \tag{2.2.3}$$

The 50 % level then corresponds to the pixel's threshold. The 30 % and 70 % points are defined as reference points to derive the noise of the module.

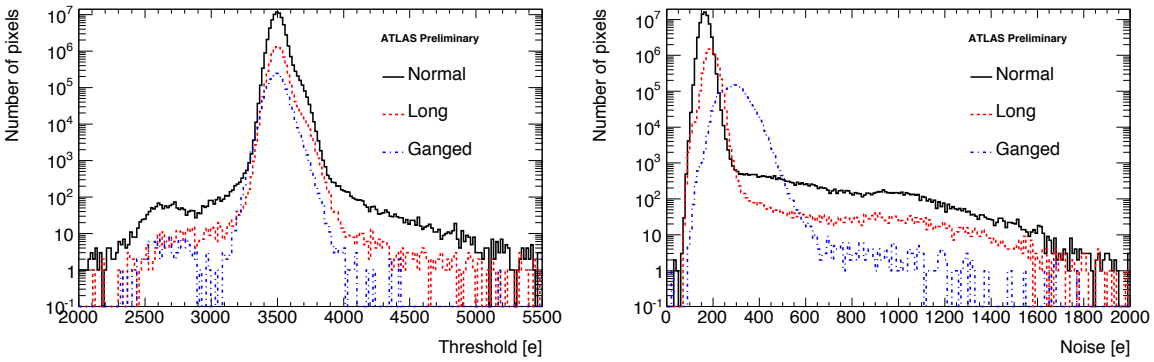

(a) (b)

Figure 2.5.: (a) Operation threshold and (b) noise distributions of all ATLAS Pixel modules [26].

The current threshold setting for the ATLAS Pixel Detector is 3500 e^- with a typical dispersion of 40 e^-. For regular pixels the noise level is well below 200 e^-, but twice as high for ganged pixels (see Figure 2.5) as they have double the capacitance of normal sized pixels. That results in a threshold over noise ratio of roughly 25 for regular sized pixels and around 10 for the ganged pixels. Pixels with a noise occupancy higher than 10^{-6} are masked online to not confuse those random hits with actual particle hits. The time over threshold (ToT) is measured in units of bunch crossing, i.e. in multiples of 25 ns in the case of the LHC. It is generally proportional to the injected or collected charge, respectively. As can be seen in Figure 2.6(a) the majority of pixels show a linear relation between injected charge and the ToT output signal. Since a MIP is expected to create a signal of ~20 ke^- in the sensor, the readout is tuned to provide a 30 bunch

crossing long output signal at this reference charge. Because of the high ToT resolution the specific ionization dE/dx (as was described in Equation 1.3.1 Section 1.3) of a track can be measured by the ATLAS Pixel Detector with a typical resolution of 10 %. It is even sufficient to distinguish a proton from a kaon in minimum bias events below 1 GeV as shown in Figure 2.6(b).

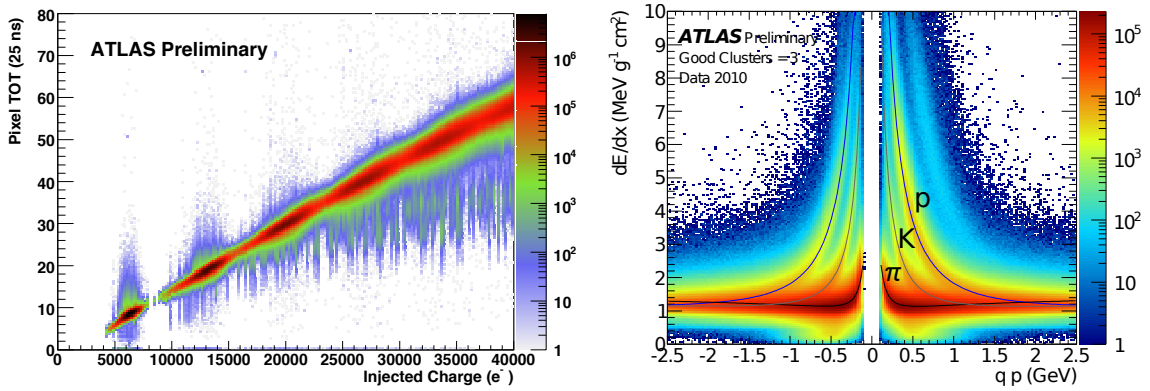

(a) (b)

Figure 2.6.: (a) Time over threshold versus injected charge of all pixels and (b) bidimensional distribution of dE/dx and momentum for tracks with 3 Good Clusters in 2010 data. The distributions of the most probable value for the fitted probability density functions of pions (π), kaons (K) and protons (p) of this track category are superimposed [26].

2.3. Performance over the first three Years

The performance of a tracking detector highly depends on its hit to track association efficiency. It is well above 98% for the different layers of the ATLAS Pixel Detector (except for the outer disks) while the B-Layer efficiency is stated with 100% because of the track selection, i.e. for this measurement only tracks traversing the B-Layer were taken into account. The result is shown in Figure 2.7(a). In this computation dead modules are excluded, but otherwise dead regions and inefficiencies contribute. The rather low efficiency for the external discs is mainly due to inefficient regions in some modules caused by either defect front end chips or disconnected solder bump bonds as shown in Figure 2.7(b). In this hit map disconnected solder bump bonds are represented by the large white area in the corners. The white horizontal space in the middle is a feature of the display which represents the sensor pixels. The ganged sensor pixels (compare Figure 2.2(b)) between the readout chips, however, are not connected to single readout pixels, but share a readout pixel within the seven outermost FE rows. Thus, the rows close to the horizontal white space show an increased number of entries in Figure 2.7(b).

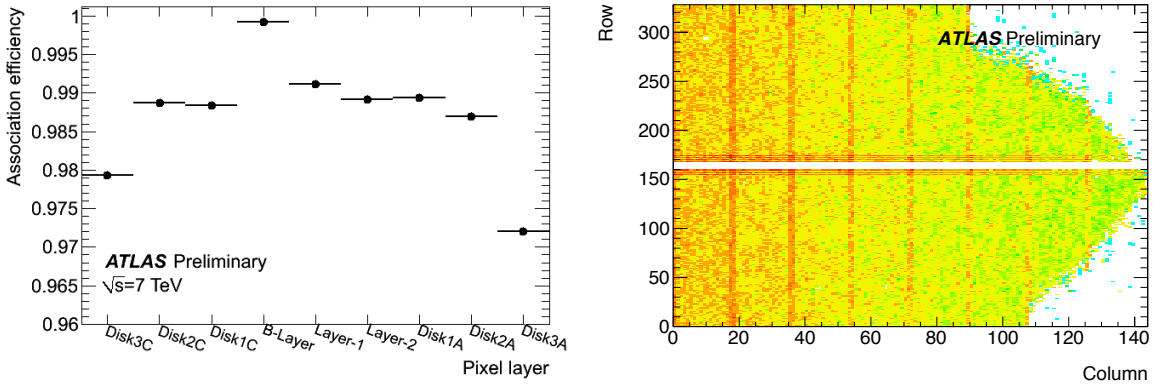

(a) (b)

Figure 2.7.: (a) Hit to track association of the three layer pixel detector and (b) the hit map of a disk module (D3AS03M) showing some inefficient regions due to disconnected bumps [26].

In the presence of an electric and a magnetic field the charge carriers created by a passing particle within silicon drift along a direction at an angle with respect to the electric field direction (see Figure 2.8(a)). They usually spread over several pixels, leading to bigger cluster sizes, depending on the angle of the incident particle. This spread is at minimum for an angle equal to the Lorentz angle. The measurement of the cluster sizes depending on the incident angle has been performed both, once with the ATLAS solenoid magnet being turned off and once in operational magnetic field (see Figure 2.8(b)). The Lorentz angle is found to be consistent with 0 for no presence of a magnetic field. Using the data with magnetic field on the preliminary measurement of the Lorentz angle is $205 \pm 0.5\,\text{mrad}$ which is in the expectation of about $225\,\text{mrad}$.

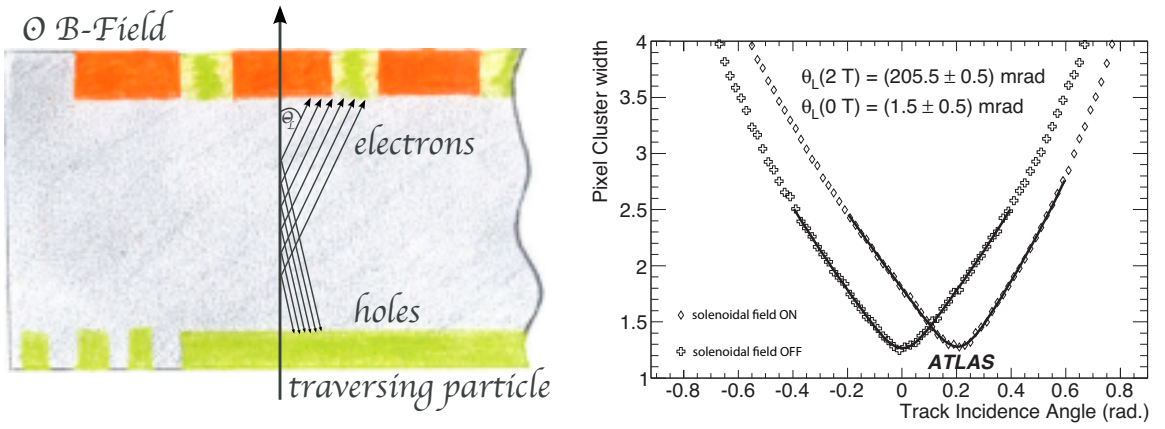

(a) (b)

Figure 2.8.: (a) Lorentz angle definition and (b) measurement of the Lorentz angle with the ATLAS Pixel Detector [26].

Furthermore, the ToT information of each pixel is used for weighted cluster position determination, so called analog clustering, improving the spatial resolution mainly in the range of two-hit clusters in the transverse coordinate as well as in the longitudinal coordinate.

2.4. Monitoring of Radiation Damages

After collecting $29\,\mathrm{fb}^{-1}$ of LHC data radiation damages are not negligible anymore. Non Ionizing Energy Losses (NIEL) are the cause for displacement defects in the sensors' silicon bulk as was described in Section 1.3.3. The first measurable effect is the increase of the leakage current through the bulk which is proportional to the fluence. Furthermore, the number of collected charge carriers drops constantly and eventually, after a fluence of $0.3 \cdot 10^{14}\,1\,\mathrm{MeV\,n_{eq}\,cm^{-2}}$ the effective doping concentration changes, mainly caused by the displacement damages. This effect eventually leads to type inversion. The leakage currents, depletion voltages and depletion depths after type inversion need to be constantly monitored and the applied voltages need to be adjusted accordingly to ensure an optimal data taking.

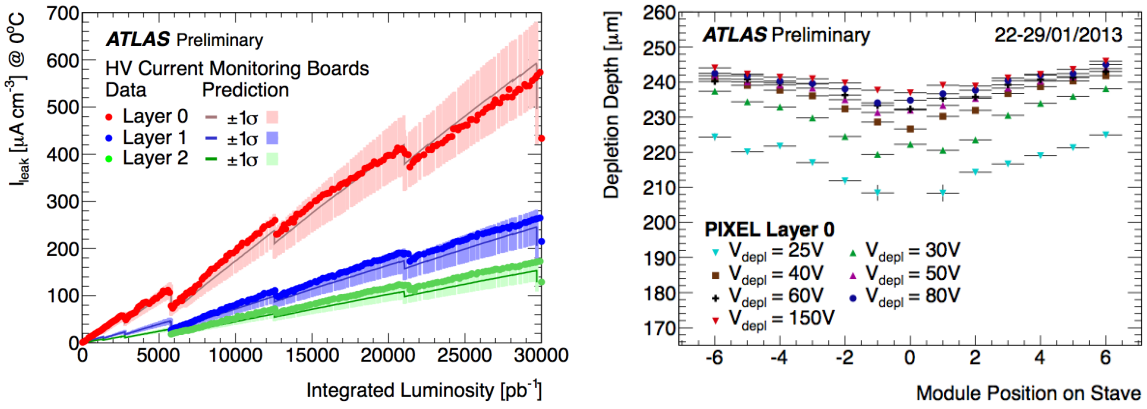

(a) (b)

Figure 2.9.: (a) ATLAS Pixel leakage current trend and (b) track based B-Layer depletion voltage measurements [26].

The measured sensor leakage current for all three Pixel layers clearly follows the integrated luminosity (see Figure 2.9(a)). The steps are consistent with annealing during detector warm up periods. The absolute values for each layer scale with the distance from the beam axis and thus the actual radiation levels. The prediction shown in that plot is based on delivered luminosity, expected fluence from simulations and the "Dortmund model". Before irradiation, for instance before type inversion, the depletion voltage can be determined using the crosstalk method at different sensor bias voltages.

Internally a very high charge (up to 200 ke^-) is injected into one pixel while the neighboring pixels are read out. Since the charge is very high it will talk over to the neighbor in case of an un-depleted sensor. By step wise applying different bias voltages one can calculate the effective depletion voltage. Performing these scans in regular intervals allows additional monitoring of irradiation levels and annealing periods.

After type inversion this method is not applicable anymore. However, actual tracks can be used to determine the depletion depth depending on the bias voltage. In Figure 2.9(b) results from the B-Layer are presented which clearly show that the depletion depth increases with bias voltage. As was found from the crosstalk method it is already type inverted since it is the innermost layer and thus suffers most from radiation damages. It is also shown that at the end of Run 1 an operational bias voltage of 150 V is still sufficient to deplete the sensors of the B-Layer.

2.5. The ATLAS Phase 0 Upgrade

For Run 2 of the LHC, starting beginning of 2015, three upgrades of the ATLAS Pixel Detector have been implemented. The original Pixel services have been renewed by installing new Service Quarter Panels with passive e-boards to route the optical transceivers to a more accessible position in case of needed repairs. In addition, a new Diamond Beam Monitor for beam loss monitoring and bunch-by-bunch luminosity measurements was installed using diamond sensors matching the FE-I4[1] footprint. Finally, the major upgrade is the Insertable B-Layer, a fourth Pixel Detector layer to increase granularity and tracking reliability. The first two will be described for the context in the following two sections. The Insertable B-Layer, which was one of the main focuses of this thesis, will be described separately in Chapter 3.

2.5.1. ATLAS Pixel Refurbishment

Inside the Pixel services special electrical-optical converters, so-called opto-boards, were used for both, translation of electrical signals from the detector into optical signals which then were sent over fibres to the service cavern and vice versa. Similar boards are used in off-detector components. There, however, the internal lasers showed a significant mortality rate and needed frequent replacement during Run 1. Thus, it was decided to reroute the on-detector opto-boards to a more accessible location and replace all on-detector services with new ones, so-called nSQPs. Those new services, just like the old ones, carry LV[2] and HV power as well as cooling and (environmental) monitoring lines. In contrary to the original SQP[3]s, however, there are passive e-boards now routing the electrical signals. The new services will also allow a later

[1] **F**ront**E**nd chip - Version 4
[2] **L**ow **V**oltage, here: readout chip bias
[3] **S**ervice **Q**uarter **P**anel

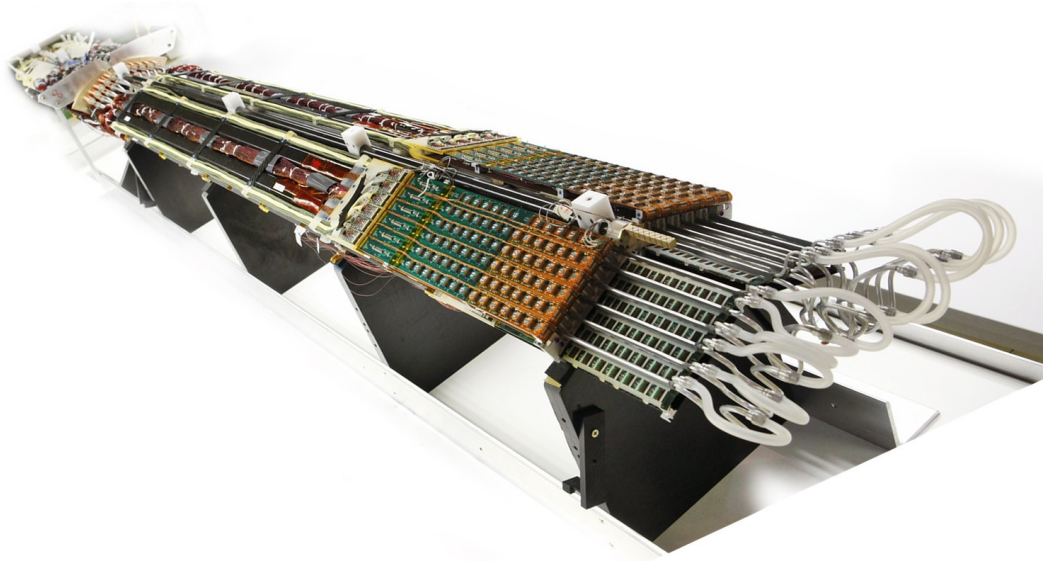

Figure 2.10.: Photograph of one out of eight ATLAS Pixel nSQP located in a test stand in the CERN Bât. 180 clean room.

Layer-1 readout speed upgrade to 160 Mbit/s by providing two outlinks per module. Readout chain differences between the ATLAS Pixel SQPs from Run 1 and the nSQPs are shown in Figure 2.11. The components basically remained the same but were routed differently. The major novelty is the opto-box that is located outside the Pixel package at the end plate of the ATLAS Inner Detector hosting the new opto-boards. At the

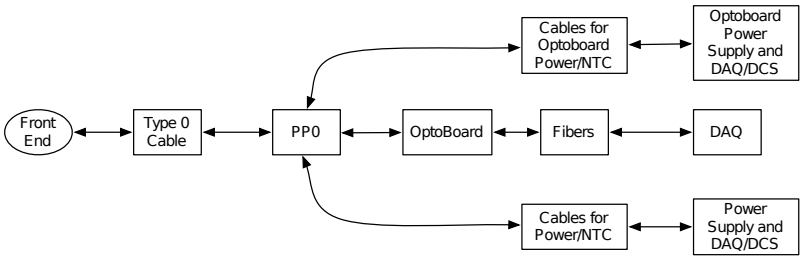

(a)

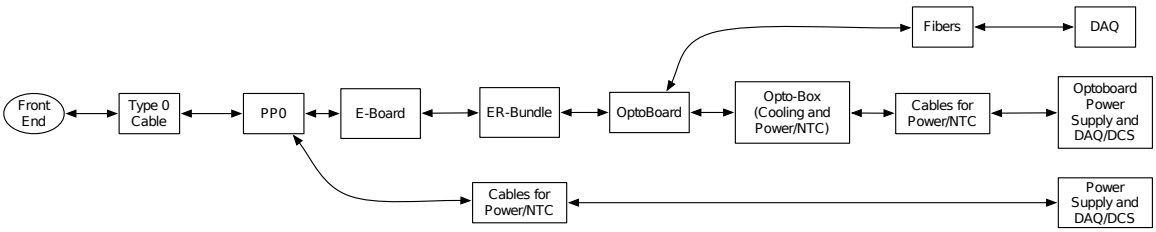

(b)

Figure 2.11.: (a) Pixel Services and (b) new Service Quarter Panel modularity [27].

end of Run 1 the working fraction of the ATLAS Pixel Detector was 95%, i.e. 88 (out of 1744) modules plus 60 individual front ends were excluded from data taking [28]. 75% of the modules were disabled due to damaged or disconnected services. Some of the remaining 25% had open HV wires that could be reworked once all services had been removed. Before re-insertion into the ATLAS Detector only 8% of the failing modules could not be recovered. Eventually, after re-insertion and testing in the detector 33 modules will be disabled at the start of Run 2 [29].

2.5.2. The Diamond Beam Monitor

Due to the foreseen raise of luminosity of the LHC significantly increased numbers of collisions per bunch crossing are expected. The Beam Conditions Monitor (BCM) [30] from Run 1 will eventually saturate within the next runs. Thus, the new Diamond Beam Monitor (DBM) [31] has been built and installed in the forward regions ($\sim$90 cm from the interaction point) into the ATLAS Pixel package in 2014. In contrast to the BCM it consists of pixelated pCVD[1] diamond sensors (21 mm $\times$ 18 mm with 500 μm thickness) which are being read out by the new Pixel front end generation FE-I4 (see Section 3.2) that is also used for the IBL[2]. It therefore uses the same readout components as the IBL but integrated into the Pixel services.

Diamond is an insulator with a band gap energy of 5.5 eV. Hence, the leakage current stays very low (order of 10 nA) even when applying a bias voltage of 1000 V to reach the desired electric field of 2V/μm. In addition, the low number of free charge carriers leads to less noise to distort the rather low signal. Furthermore, diamond has a much higher thermal conductivity than silicon: 2000W/m·K (compared to 150 W/m·K), i.e. less cooling coupling is needed which is advantageous considering the position of the DBM (see Figure 2.12) close to the sensitive part of the 3-Layer ATLAS Pixel Detector and with no dedicated cooling loops connected to the chips. Only the main mechanical structure is cooled using C_3F_8 cooling loops that were formerly used to cool the opto-boards inside the SQPs.

Mechanically it is organized in so-called telescopes where each telescope holds three sensors and one hitbus chip for advanced triggering. In total there are eight telescopes, four on each side of the Pixel Detector at an angle of 10 ° with respect to the beam axis. This tilt was chosen as a compromise between orientation towards the interaction point and an angular displacement with respect to the magnetic field lines in the ATLAS Inner Detector which has a positive effect on the erratic dark currents suppression [32]. However, because of production difficulties there had not been enough diamond sensors available at the time of integration into the Pixel package. Hence, two of the telescopes host three planar n^+-in-n silicon sensors instead.

[1] **p**olycrystalline **C**hemical **V**apor **D**eposition
[2] **I**nsertable **B**-**L**ayer

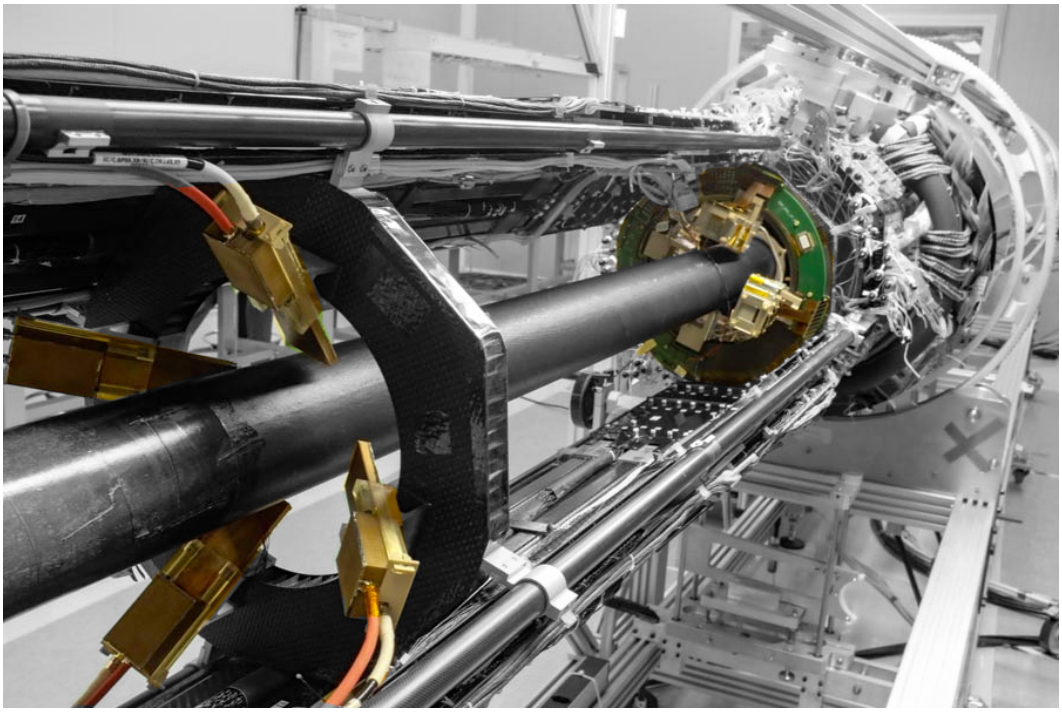

Figure 2.12.: Photograph of the ATLAS Pixel package located in a test stand in the CERN SR1 clean room. One can see 4 BCM detectors on the left and 4 DBM telescopes closer to the Pixel detector around the IST. Two nSQPs are already loaded. One at the top and one at the bottom of the support structure.

Hey now, hey now now,
sing this corrosion to me
(Like a healing hand)
- Sisters of Mercy

Chapter 3

The ATLAS Insertable B-Layer

An additional layer of pixel detectors, known as the Insertable B-Layer (IBL) [33], was installed in mid 2014 into the existing 3-layer ATLAS Pixel Detector [22] in order to improve tracking robustness, the tracks' impact parameter reconstruction, vertexing and b tagging performance for Run 2 and 3 of the LHC. This new layer of silicon pixel detectors was mounted around a new, smaller radius Beryllium beam-pipe at a nominal distance of 33.25 mm from the beam. It is more robust to the conditions expected for the upcoming runs, namely increased luminosity, radiation damage and pileup and thus will help compensate possible failures that may emerge over time in the existing pixel layers.

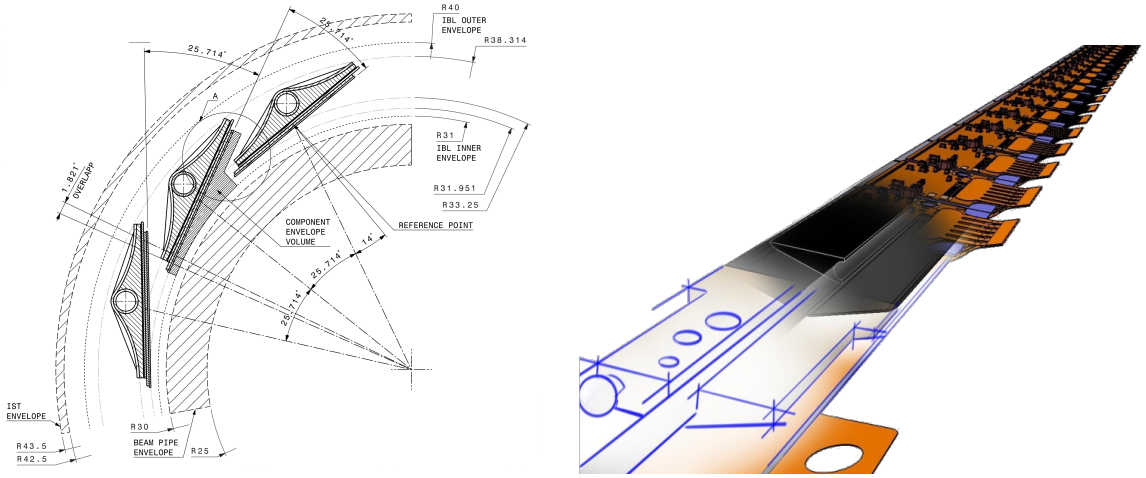

(a) (b)

Figure 3.1.: (a) Partial technical drawing of the ATLAS IBL [33] and (b) a 3D sketch of one stave.

Two new sensor designs were implemented to minimize inactive area: planar n^+-in-n sensors with slim edges and double sided 3D designs with a slim fence. Details on the specific IBL sensor designs can be found in Section 3.1 and in [34]. An IBL module consists of either one planar sensor hosting two FE-I4 [35] chips or one 3D sensor bump bonded to one FE-I4 chip. With the FE-I4 generation the individual pixel size

was reduced from $50 \times 400\,\mu\text{m}^2$ to $50 \times 250\,\mu\text{m}^2$ which reduces the cross section and simultaneously increases the granularity of the detector. Each pixel holds internal calibration circuits as well as adjustable charge sensitive amplifiers and discriminators. More details on the FE-I4 readout chip will be given in Section 3.2.

The modules are glued to 64 cm long Parylene coated carbon foam support structures (staves), covering up to a pseudo-rapidity[1] $|\eta| \leq 2.9$. Twelve planar modules (24 FE-I4 chips long) cover the central part of a stave, and four 3D modules (four FE-I4 chips long) cover the regions of the both ends of a stave. In total 32 FE-I4 units are placed on a stave.

The IBL Detector consists of 14 staves made of low density carbon foams mounted at a tilt angle of 14° (Figure 3.1(a)). The light design structure of the IBL leads to a radiation length of 1.9 %. Inside the carbon foam support structure a titanium pipe carries CO_2 for cooling. In total 20 staves were built over the past two years and eventually tested in a designated setup at CERN. The main results obtained in this QA[2] bench will be presented in Section 3.4.

3.1. The IBL Sensors

The sensors are required to have in inactive edge of at most $450\,\mu\text{m}$ as there can be no overlap of material in z (along the beam direction) due to space constraints. Considering the expected lifetime and the service capabilities of the ATLAS IBL, the sensors must show sufficient charge collection up to a fluence of $5 \cdot 10^{15}\,\text{n}_{\text{eq}}\,\text{cm}^{-2}$ at a total ionizing dose of 250 MRad, be operational at a temperature of -25 °C, dissipate at maximum $200\,\text{mWcm}^{-2}$ power at a temperature of -15 °C and, furthermore, the required high voltage must not exceed 1000 V.

In the beginning four technologies were considered: Planar n^+-in-n silicon, planar n^+-in-p silicon, 3D silicon and diamond sensors. Because of availability and high costs, diamond sensors were not chosen for the IBL. However, they were integrated into the DBM as described in Section 2.5.2. Instead, 75 % of the IBL sensors are planar n^+-in-n and 25 % are 3D silicon sensors, respectively. These sensors will be discussed in the following pages.

3.1.1. Planar Sensors

The planar n^+-in-n technology was already implemented in the 3-layer ATLAS Pixel Detector in Run 1 and had proven to be reliable during its operation so far (see Figure 3.2 (top)). Hence, it was favored to construct a new sensor as close as possible to the

[1] $\eta \equiv -\ln[\tan(\theta/2)]$, where θ is the angle between the particle three-momentum p and the positive direction of the beam axis

[2] **Q**uality **A**ssurance

previous one but matching the FE-I4 footprint. So, 4" n-doped float zone silicon wafers with <111> crystal orientation and a bulk resistivity of 2-5 kΩcm were produced at CiS in five different thicknesses from 250 μm to 150 μm, while the yield was stable down to 175 μm. For hybridization, however, an UBM[1] needs to be applied in a dedicated process step which can cope with wafers down to 200 μm thickness. For thinner wafers an additional handling wafer would have been necessary. Thus, it was decided to

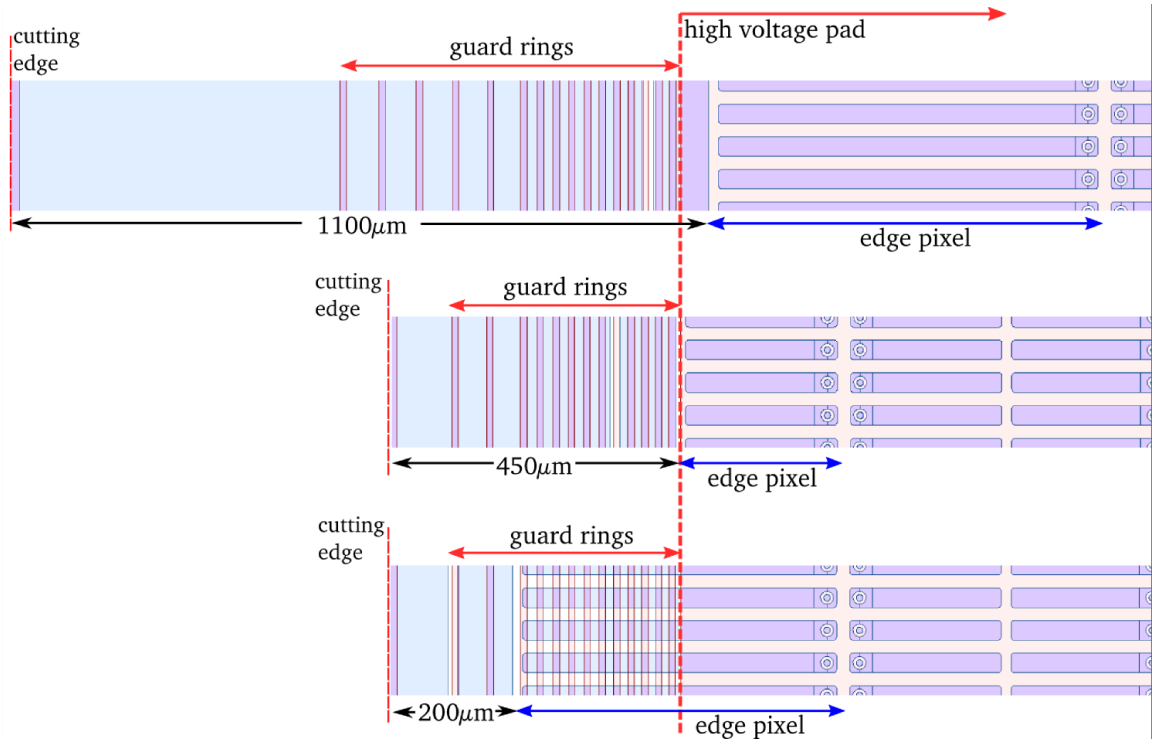

Figure 3.2.: Top view of the sensor edge region of the ATLAS Pixel (top), the conservative (middle) and the slim edge (bottom) IBL design. The n^+ implantation is seen in blue, the p^+ implantation in red. By reducing the number of guard rings, narrowing of the safety margin and by extending the edge pixels beyond the high voltage pad, the inactive edge could be reduced from 1100 μm for the ATLAS Pixel design to ca. 200 μm for the slim edge IBL design [36].

use 200 μm thick wafers for the ATLAS IBL in order to reduce production costs [34]. The bias grid network, which allows to supply the high voltage via the punch-through effect, was kept in the new design to ease the step of sensor characterization and to avoid a floating potential on pixels having an open bump connection to the readout chip, despite the fact that the charge collection efficiency decreases significantly in the bias-dot region with irradiation. The bias-dot is each pixel's connection to the bias grid located at the other end of the pixel with respect to the readout bump. The bias grid

[1] **U**nder **B**ump **M**etallization

is connected to an approximately 90 μm wide bias grid ring which surrounds the pixel matrix. Outside the bias ring, a homogeneous n^+-implantation (the so-called outer guard ring) extends to the dicing streets and ensures that the sensor surface outside the pixel matrix and the cutting edges share the same potential. Each pixel, the bias grid and the outer guard ring are connected to the FE-I4 readout chip via bump-bonds. There are two bumps each for the bias grid and the outer guard ring. In the 3-layer ATLAS Pixel Detector design with a module overlap in z, the 16 guard rings reach a width of 600 μm and an additional safety margin towards the dicing street of 500 μm could easily be left.

To meet the IBL requirements of a minimized inactive area on the sensor edges in z, however, the number of guard rings was reduced in the so-called conservative design (see Figure 3.2 (middle)). This design exactly meets the requirement of a maximum inactive edge width of 450 μm. The influence of the number of guard rings on the break down behavior had been evaluated in [37]. In addition, a second design was implemented in which the overlap between the active pixel region and the guard ring region on the backside of the sensor was increased, the so-called slim edge design (see Figure 3.2 (bottom)). In testbeam measurements it was found that the charge collection efficiency reduces with increasing distance from the edge of the bias voltage pad due to the inhomogeneously formed depletion zone in the sensor. However, it was shown in [38] that the collected charge is sufficient for reliable particle detection up to a distance of about 200 μm from the bias voltage pad. The production yield during the prototype runs was stable for both designs. Thus, the planar slim edge design with 13 guard rings and 500 μm long edge pixels (i.e. 250 μm overlap in the guard ring region) was chosen for the ATLAS IBL Detector. More details on the planar n^+-in-n sensor designs can be found in [36] and [39]. Finally, $18.8 \times 41.3\,\mathrm{mm}^2$ big double chip sensors with 450 μm long pixel bridging the gap between the two readout chips, which are bump bonded to the sensor, were produced.

3.1.2. 3D Sensors

A new approach of manufacturing sensors, instead of processing the surface of a silicon wafer, is to use the rather recently developed industrial process called DRIE[1] to penetrate the bulk. In a high temperature thermal diffusion process n^+ and p^+ electrodes can be established inside the formed pillars. Thus, the electrons and holes drift horizontally between the columns which significantly reduces the collection distance and hence the required bias voltage. Just like in the planar scenario it was favored to avoid using handling wafers. The so-called double sided 3D design with a slim fence was chosen for the ATLAS IBL as first sensor application in high energy physics experiments and candidates for future detectors. In this case the n^+ columns were etched from the front and the p^+ columns from the back side. Contrary to the planar sensors, 4" p-type float zone wafers with a thickness of 230 μm were used.

[1] **D**eep **R**eactive **I**on **E**tching

The sensors were produced by two different manufacturers: CNM[1] and FBK[2]. There are slight differences in the designs as shown in Figure 3.3. The most prominent difference is the depth of the columns. While for FBK sensors the columns fully penetrate the substrate (Figure 3.3(a)) the columns stop shortly before reaching the opposite surface in the CNM design (Figure 3.3(b)). Furthermore, two different ways for isolating the columns from each other were implemented. FBK sensors have p-spray implantations on both ends of the column, whereas CNM sensors have p-stop implantations in the front side. The third difference is the implementation of the slim fence to gradually reduce the potential towards the conductive cutting edge. In the CNM case, a slim edge guard ring structure which combines a grounded n^+ 3D ring and biased fences are used. For FBK sensors, however, several rows of ohmic columns shielding the cutting edge from the active area were implemented [34].

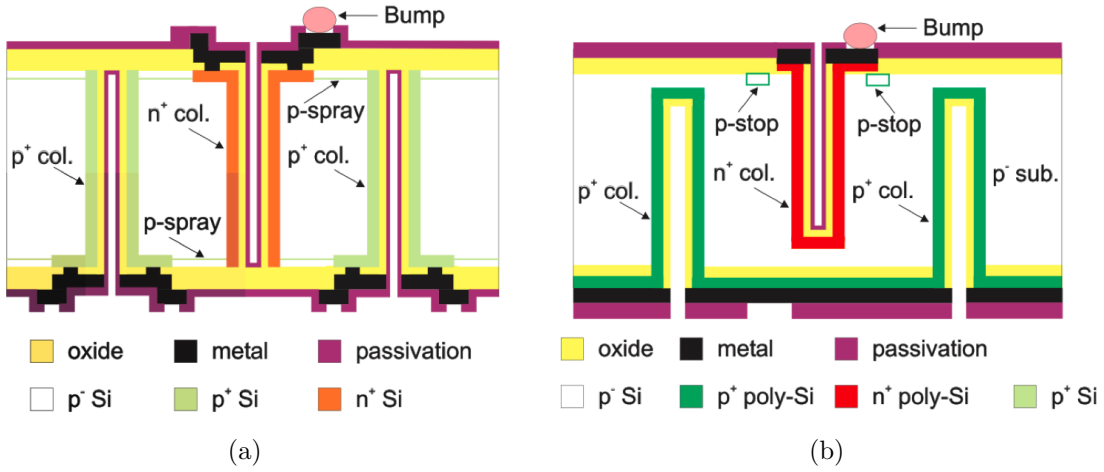

Figure 3.3.: (a) FBK and (b) CNM sensor design sketches. [34]

3.2. The IBL Readout Chip

To cope with the much more challenging requirements for the detector performance in the IBL case compared to the 3-layer ATLAS Pixel Detector, a completely new readout chip had to be designed. The main drivers for the new development were the very limited space available inside the 3-layer ATLAS Pixel Detector (for mechanics as well as for services), material budget, increased radiation environment, more pile-up events expected from the LHC in Run 2 and investigation of low cost approaches with regards to future upgrades. The very limited space and low material budget requirements lead to rather strict constraints for cooling capacity and power dissipation. To reduce the

[1] **C**entro **N**acional de **M**icroelectronica (Barcelona, Spain)
[2] **F**ondazione **B**runo **K**essler (Trento, Italy)

cable budget and to limit the power losses, the current flowing through the supply lines had to be minimized. Thus, a maximum analog and digital current of 10 μA per pixel was targeted. To reduce transient currents in case of load fluctuations, e.g. during configuration of the chips or in case of accidental configuration loss, the on-chip LDO[1]s are operated in a partial shunt mode. That means, as long as the chips' current consumption is above a minimum adjustable input current they are operated as usual LDOs. However, if the consumption is below that threshold, an additional current is shunted by the powering blocks. The reference voltages needed for the operation of the two LDOs are generated on-chip. The digital activity was reduced with respect to the FE-I3 generation by changing from a column drain architecture to four-pixel regions, i.e. four analog pixels sharing one digital block (see Figure 3.4). In the FE-I3 case a hit pixel is busy until the double column bus is free to send the hit information to the end of column logic. With increased hit occupancy this bus starts to saturate and consequently the number of rejected hits would reach an unacceptable level [35].

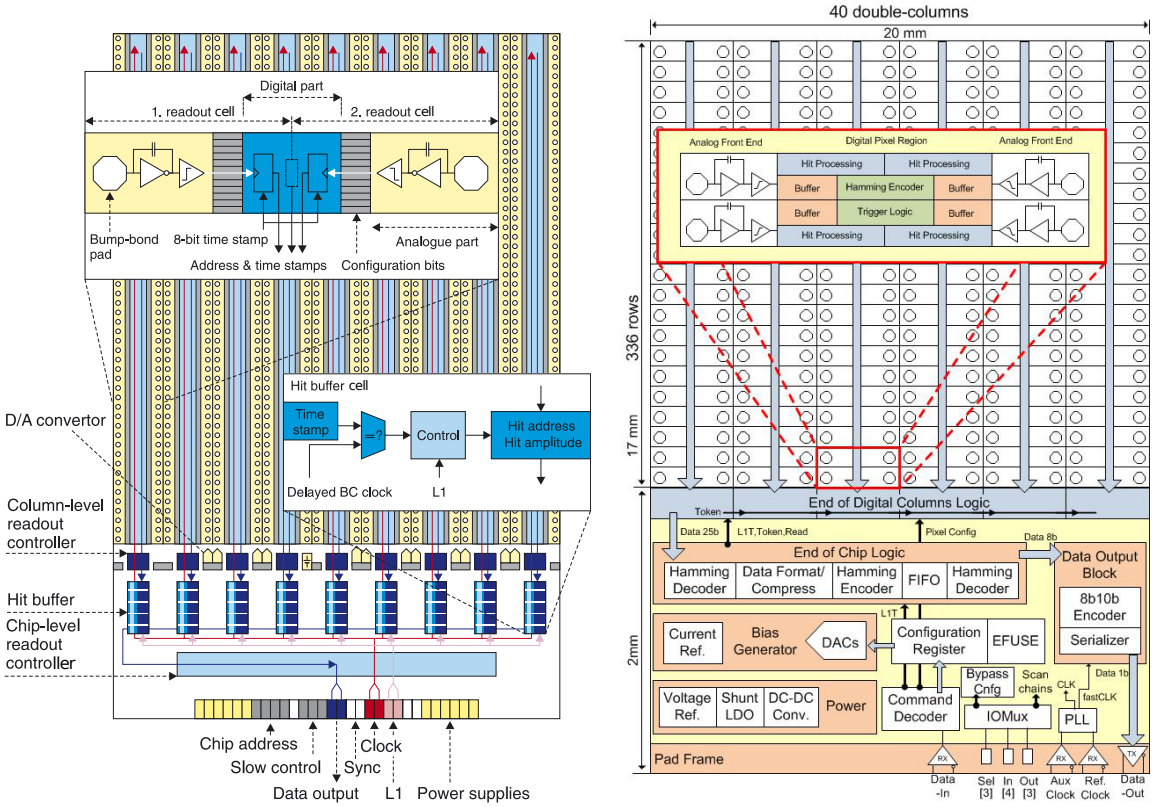

Figure 3.4.: (a) FE-I3 [22] and (b) FE-I4 chip diagram [34]. Not to scale.

[1]**L**ow **D**rop-**O**ut regulators

In the FE-I4 case a shared SEU[1] hard FIFO[2] memory and an additional logic block were built into the four-pixel regions which can store up to five events with a dedicated counter keeping track of the time elapsed since the hit occurred. Broadcasted from the End of Chip Logic an external trigger (Level 1) selects the events matching the programmed latency from the corresponding blocks. The Hamming encoded data output from the pixel array is then decoded in the End of Chip Logic, re-organized for bandwidth reduction and to fit an 8-bit-word-based scheme for the following encoding step. The data is subsequently stored in an asynchronous FIFO before being processed by the Data Output Block. The Data Output Block collects the pixel data stored in the End of Chip logic FIFO and provides 8b/10b encoding before streaming out the encoded data at 160 Mb/s. The additional decoding steps were implemented to improve the data stability. Since the data is only transferred to the periphery in case of a trigger, the digital activity along with the power dissipation are immensely reduced while the chip can cope with much higher hit occupancies compared to the previous chip generation. Another improvement in that respect is the individual pixel size. It has been reduced from $50 \times 400\,\mu\text{m}^2$ to $50 \times 250\,\mu\text{m}^2$ which reduces the cross section and simultaneously increases the granularity of the detector. The pixels are organized in a 80 columns by 336 rows matrix. The chip's physical size is $20.2 \times 18.8\,\text{mm}^2$ with an active area of $20.2 \times 16.8\,\text{mm}^2$ and a periphery of $20.2 \times 2.0\,\text{mm}^2$, resulting in an active to inactive area fraction of about 90 %. The chip's size corresponds roughly to the biggest reticle size available in current production lines which was chosen to maximize the active area fraction while reducing flip chipping costs which scale with the number of flip chips rather than the size of bonded area. By thinning down the chips to a thickness of 150 μm the radiation length can be further reduced. The smaller feature size[3] leads to more radiation hardness due to thinner gate oxide transistors plus more digital complexity in less area.

The analog part of each pixel cell consists of an AC[4] coupled two-stage architecture, optimized for low noise, low power and fast rise time. A schematic of the cell is shown in Figure 3.2. The first charge sensitive amplifier amplifies and shapes the signal. Its feedback current can be trimmed individually by a local DAC, whereas the second stage is steered by global DACs. It provides an additional amplification factor which is defined by the ratio of the coupling capacitor C_c to the feedback capacitor C_{f2} of the second amplifier. The second stage output is coupled to an adjustable discriminator which defines the threshold. The calibration of the analog pixel electronics is performed by a local charge injection circuitry. In the production version of the chip, FE-I4B, a circuitry allowing to measure the sum of both test charge injection capacitances was implemented to simplify the charge calibration. These capacitances were determined on wafer level in the production sites. To ensure a homogeneous response of all pixels to the sensor's analog signal various DAC settings need to be adjusted. This was done several times throughout the production of detector modules and staves to monitor the

[1] **S**ingle **E**vent **U**psets
[2] **F**irst **I**n **F**irst **O**ut
[3] 130 nm CMOS process compared to 250 nm CMOS process in the 3-Layer ATLAS Pixel Detector
[4] **A**lternating **C**urrent

overall chips' state as the absolute values do depend on environmental conditions such as e.g. temperature and humidity.

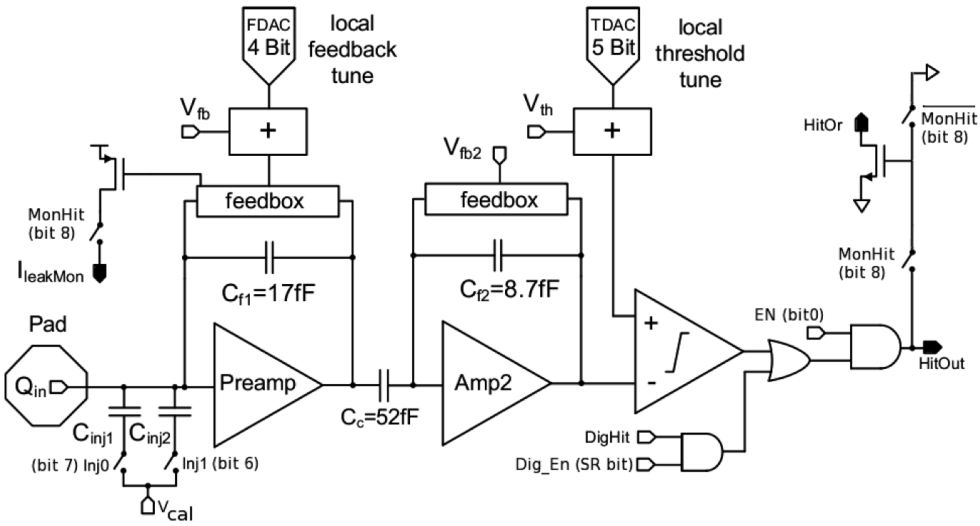

Figure 3.5.: Schematic of the the analog cell in the FE-I4 chip [34].

3.3. From Modules to Staves

To combine the sensors and the readout chips, a special bump bonding process was developed at IZM[1]. In this so-called flip-chip process SnAg solder bump bonds connect the individual pixels. A reflow step operates at a temperature of 260 °C. To avoid bending of the 150 μm thin chips an additional glass carrier was glued to the backside of the chips for mechnical support. Using a polyimide glue it can be released by laser exposure which decomposes the glue. The number of bump bonded modules throughout the IBL production is represented by the blue trend line in Figure 3.6.

The next step was the assembly of a module. An IBL module consists of either one planar n^+-in-n sensor hosting two readout chips (double chip module) or one 3D sensor bump bonded to one readout chip (single chip module). The electrical signals to and from the chips are transported via wire bonds through a flexible PCB[2] (module flex) which is glued on top of the assembly using a tape strip (PPI RD-577F) under the wire bond pads and dots of epoxy glue (UHU EF 300) at several locations. The module flex is a 130 μm thick two copper layer PCB with passive SMD[3] components mounted, e.g.

[1]Fraunhofer-**I**nstitut für **Z**uverlässigkeit und **M**ikrointegration (Berlin, Germany)
[2]**P**rinted **C**ircuit **B**oard
[3]**S**urface **M**ounted **D**evice

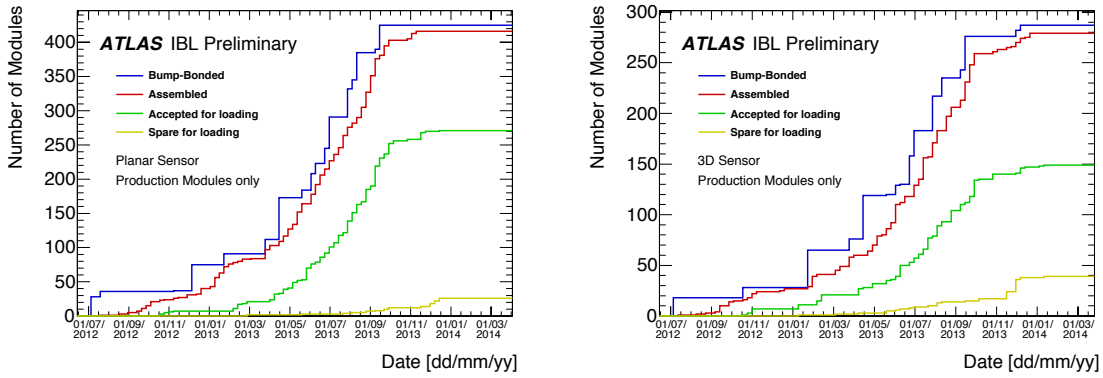

(a) (b)

Figure 3.6.: ATLAS IBL module production trends: for (a) Planar Double Chip modules, IBL production only (up to batch 12) and (b) 3D Single Chip modules, IBL production only (up to batch 13) [29].

HV filter capacitances or LVDS[1] termination resistors. The number of fully assembled modules throughout the IBL production is represented by the red trend line in Figure 3.6. To be accepted for loading, a module had to pass several sets of quality control measures. The assembly of the modules and the quality control measurements were performed at two institutes, namely University of Bonn and INFN Genova. The first basic communication tests were run to reveal and reject non operational modules and those showing severe failures in the bump bonding process. Sorting out defect modules at this stage eventually saved time for upcoming more detailed characterization. All modules passing these short tests were thermally cycled ten times from -40 °C to 40 °C with a rest at each extremity for one hour to apply thermally induced mechanical stress on the modules. Eventually more qualification tests were performed incl. tests and measurements similar to the ones that will be described in more detail in Section 3.4. Module rating and determination of the loading position on each stave were based on these results.

Modules arriving at the stave loading site were dressed as seen in Figure 3.7. Here, a planar module is shown. The assemblies were mounted on an aluminum carrier, along with the full size module flex for mechanical support and a connector for handling and testing. The temporary connector was removed and the remaining module was glued onto a bare stave with high precision alignment. Then the wings, guiding the electrical connections from the stave flex underneath the stave to its face plate, were glued onto the module flexes. For monitoring the wire bonding process, four additional wire bonds every two readout chips were set and pulled afterwards. The average pull strength of the entire production was 6.5 ± 0.6 g while 5 g was the required minimum pull strength. The module alignment was verified in metrology measurements where

[1] **L**ow **V**oltage **D**ifferential **S**ignal

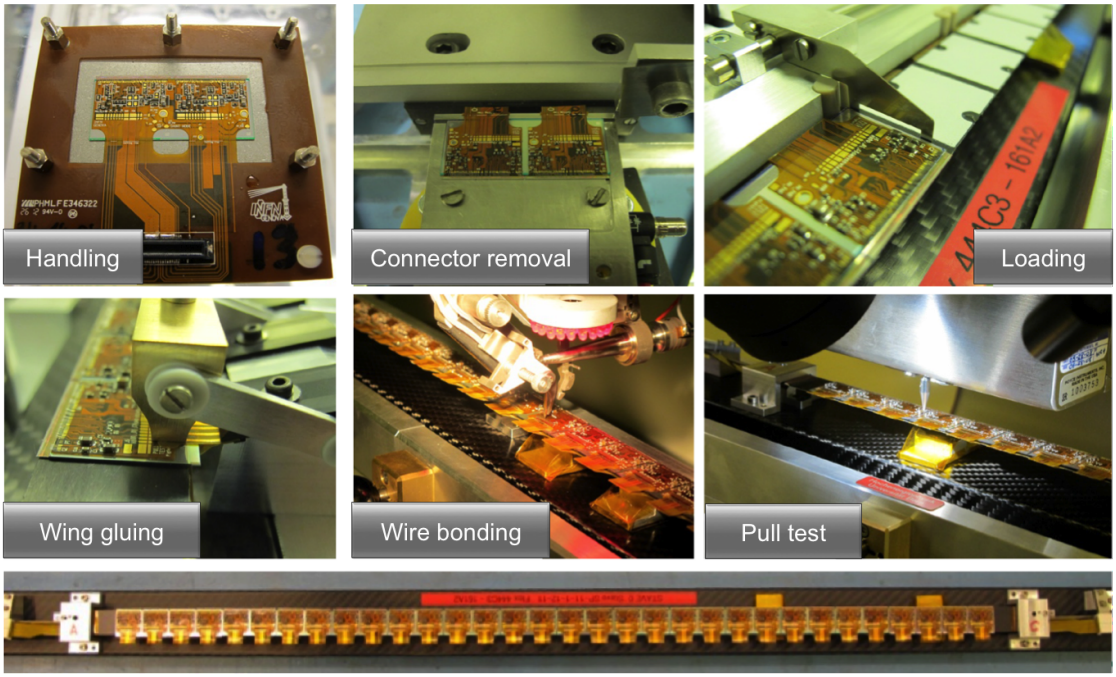

Figure 3.7.: Photo series of the stave loading process.

fiducial marks on the sensors served as reference points. The module positions were verified along and across the stave to avoid mechanical contact between two modules. It was observed that no module deviated more than 150 μm from its nominal position. Thus, all staves fulfilled the mechanical IBL qualification. The subsequent module tests comprised verification of the electrical and logical functionality of the chips and their calibration of deposited charge threshold and time over threshold. If those steps were successfully passed, the staves were shipped to CERN where they were integrated into a dedicated test bench for full qualification. In case of failure, a module not satisfying the requirements was replaced on site, which occurred for about 10 % of the production.

3.4. Production Accompanying Measurements

During the production of the IBL all components were tested several times, individually and eventually as combined objects. In this section the extensive measurements performed on already fully assembled staves will be discussed. First, the SR1 Stave QA bench including its DCS[1] and DAQ[2] components will be described. In the following section the calibration steps including some example plots will be presented. Finally, the rating results and overall performance plots will be shown. It should be noted that two production staves were accidentally exposed to an increased level of humidity. The

[1] **D**etector **C**ontrol **S**ystem
[2] **D**ata **Acq**uisition

resulting chemical reaction lead to rejection of these staves, namely Stave7 and Stave8, for the IBL production. Therefore, only results from the remaining 18 production staves will be discussed in the next sections.

3.4.1. The IBL Stave Testing Setup in SR1

The CERN SR1 ATLAS IBL Stave QA bench consists of two main areas. There is a rack area outside the clean room that holds the main power supplies, the readout system and the interlock crates. Most of the services were adapted from the already existing ATLAS Pixel Detector test setup and pulled to the test stand in the clean room. There is a ca. $2\,\mathrm{x}\,1\,\mathrm{x}\,1\,\mathrm{m}^3$ environmentally controlled aluminum box, insulated with a flexible foam layer, with feed troughs on each short side for cables as well as cooling pipes. Inside that box two staves can be placed into dedicated Delrin supports. The box can be closed with interlocked doors on both long sides and flushed with dry air. In a second upgrade of the box, a nitrogen line was added that flushes the smaller stave volume directly. There is a humidity and temperature interlock switching off the cooling unit in case the dew point is too close to the current stave temperature. In the described setup a transportable CO_2 unit (TRACI[1]), which was developed at

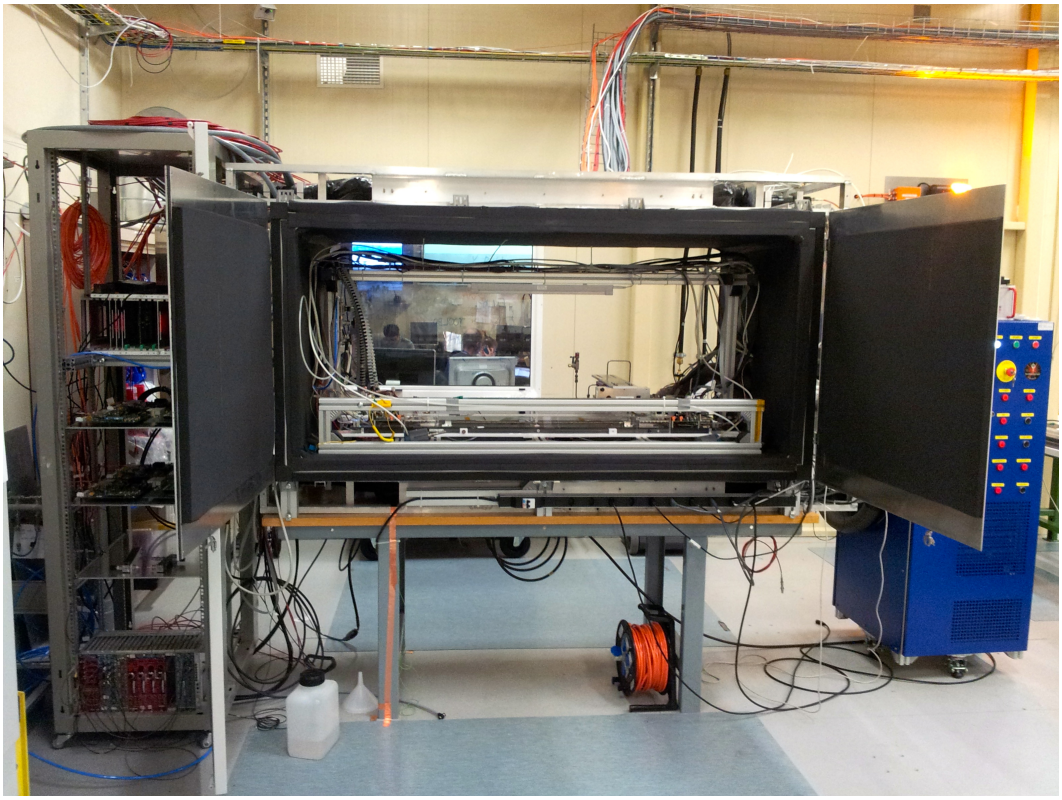

Figure 3.8.: Photo of the environmentally controlled box in the ATLAS IBL stave test bench at CERN [40].

CERN, was used for cooling the staves. The rack close to the environmental box hosts the second stage regulated LV power supplies, readout adapter cards and also a NIM[1] crate for scintillator triggering in case of cosmic tests. Since the cosmics rate is rather low, however, it was decided to mainly use radioactive sources for sensor qualification and disconnected bump studies. For this purpose, two ^{90}Sr and two ^{241}Am sources were available which could be mounted onto a support structure connected to a linear motor. This motor could be steered from the DAQ panel and thus allowed running automated source scans. A photograph of the setup inside the clean room facility in SR1 can be seen in Figure 3.8.

The staves were connected to powering and readout via EoS[2] PCBs which were designed and produced specifically for testing purposes. The services and supplies connecting to these PCBs were chosen as close as possible to the actual detector components, meaning that the cables have the actual lengths and depending on the availability actual supplies and monitoring devices or prototypes were used. For LV powering former ATLAS Pixel PP2[3] regulator boards were integrated into the setup. For each channel two regulators were combined at the EoS PCB to be able to supply a higher current consumed by one DCS group compared to the ATLAS Pixel module. There are sense lines connecting the PP2 to the EoS PCB for each DCS group which consists of four FE-I4 read out chips. The naming convention (A and C side, counting modules from the interaction point to each end of a stave) is in accordance with the ATLAS naming scheme. It is shown in Figure 3.9.

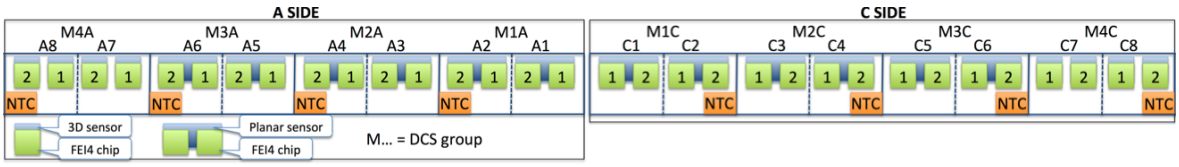

Figure 3.9.: Sketch of the stave layout indicating the naming scheme used in the ATLAS IBL [40].

The PP2 regulator station was supplied by WIENER[4] power supplies located in the rack area in SR1, outside the clean room. For sensor HV a new generation of ISEG[5] supplies were installed: one max. 1000 V version for the planar sensor bias and a max. 500 V version with a slightly better current resolution for the 3D sensor bias. The DCS was accessible to the operator via a dedicated software panel running on the

[1] **T**ransportable **R**efrigeration **A**pparatus for **C**O_2 **I**nvestigation
[1] **N**uclear **I**nstrumentation **M**odule
[2] **E**nd **o**f **S**tave
[3] **P**atch **P**anel **2**
[4] **W**orldwide-**I**ndustrial **E**lectronics-**N**uclear **E**lectronics-**R**esources, W-IE-NE-R, Plein & Baus GmbH (Burscheid, Germany)
[5] iseg Spezialelektronik GmbH, Germany

DCS PC. Voltages could be switched on, changed and limits for the software interlock could be set. Current compliances lead to reduction of supply voltages and warnings were screened. In case of overheat or too much humidity inside the testing box all voltages could be switched off immediately by the IMC[1]. For improved failure safety the IMC was realized purely hardware based, including a flash FPGA[2] with an internal EEPROM[3]. For more details see [41].

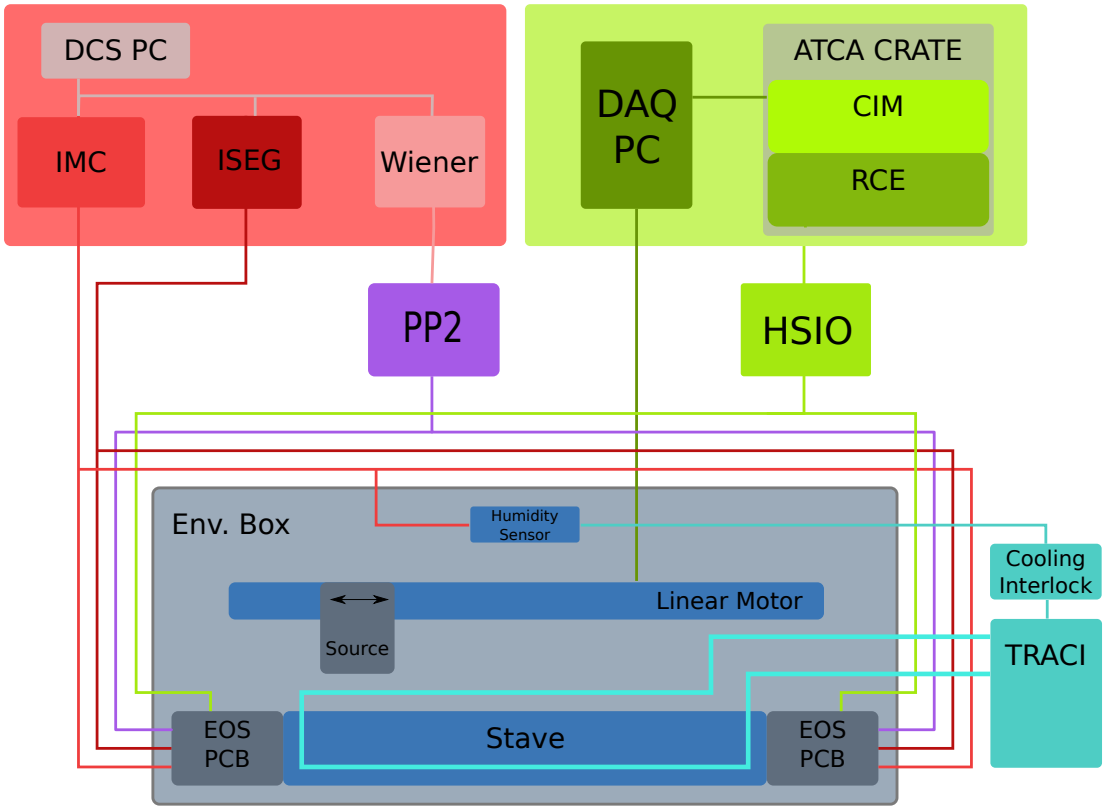

Figure 3.10.: Schematic view of the ATLAS IBL stave test bench at CERN. Original taken from [40] and modified.

Readout wise the modularity is slightly different. To minimize the services inside the active area of the detector two chips share one command line and thus form one readout group. The data is sent out on individual lines. In the case of the Stave QA bench described in this section, a completely new readout system was used because the IBL readout system was not available by the time the QA measurements were performed. It

[1] **I**nterlock **M**atrix **C**rate
[2] **F**ield **P**rogrammable **G**ate **A**rray
[3] **E**lectrically **E**rasable **P**rogrammable **R**ead-**O**nly **M**emory

is a highly modular system developed at SLAC[1], based on the ATCA[2] crate standard. A crate with five slots hosts two CIM[3] and three RCE[4] boards while one RCE board holds two RCEs, which generate commands, receive and chart the data. One RCE can handle up to eight FE-I4s. That means four RCE boards are needed for the IBL Stave QA bench. A CIM is the control unit and communication interface, a 96 channel 10 Gb/s ethernet switch, establishing connections between the DAQ PC and the according RCEs. Customized routing and logic can be implemented in the HSIO[5]s that directly connect to the EoS PCBs. They also translate the electrical signals from the modules into optical signals, which are further transmitted to the RCEs and vice versa. In addition, in the case of the Stave QA bench, the HSIOs provide buffering, multiplexing of commands and 8b/10b decoding of the FE-I4 data as well as generation of the clock and cyclic or external triggers. As can be seen in Figure 3.10 the HSIOs were not hosted in the ATCA crates but in the rack right next to the setup. The calibration and data taking was executed by the operator via a dedicated DAQ panel which collected configuration files, ran scans and displayd the results of each scan. The module configurations were lists in plain text format, holding the FEs register names and individual setting. The results were saved in the ROOT[6] file format.

3.4.2. Quality Control Measurements

Four days were needed for each stave to be tested, including the time for installation, removal and optical inspections. The test flow comprised verification of the electrical and logical functionality of chips and sensors, calibration of all chips to the same (standard) settings, running of source scans for charge calibration, sensor functionality and disconnected bump bond studies and concluded in the determination of the total number of inoperable pixels based on the information from all previous scans. First, high resolution overview pictures were taken followed by detailed inspection of all wire-bonds and critical electrical components. The inspector's comments and pictures were stored in a dedicated QA database. If nothing suspicious was found during the optical inspection, the stave was integrated into the environmental box (Figure 3.8).

In the following pages typical results will be shown using the example of Stave12. Overall results summing up the performance of all production staves will be presented in Section 3.4.3.

At first, the basic electrical functionalities were verified. Since the PP2 regulates based on a sense measurement at the EoS PCB these lines had to be tested properly before power-up. In case of a broken line the maximum regulator output voltage would be

[1]SLAC National Accelerator Laboratory, originally **S**tanford **L**inear **A**ccelerator **C**enter
[2]**A**dvanced **T**elecommunications **C**omputing **A**rchitecture
[3]**C**luster **I**nterconnect **M**odule
[4]**R**econfigurable **C**luster **E**lement
[5]**H**igh-**S**peed **I**nput-**O**utput
[6]C++ based data analysis framework developed at CERN

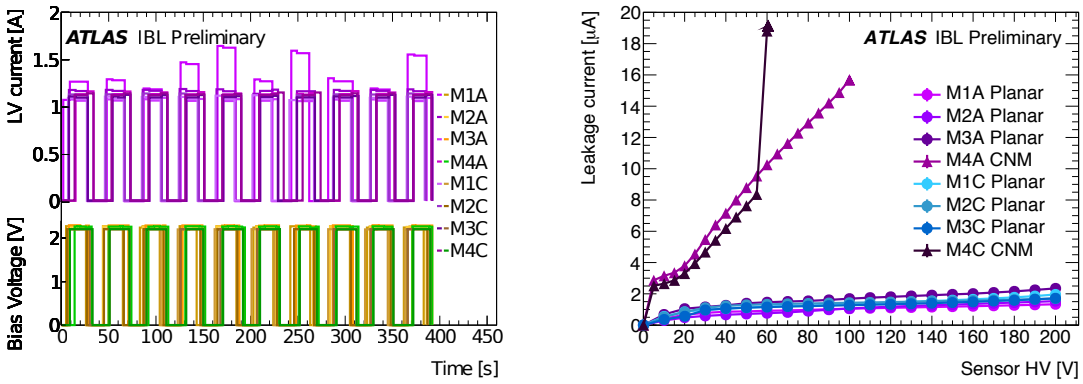

(a) (b)

Figure 3.11.: (a) LV cycles and (b) sensor IV characteristics for all DCS groups of ST12 [29], [40].

applied to the module. Thus, the regulator input voltage needs to be reduced in the first step to avoid destruction of the readout chips. If all sense lines are connected properly, power-up studies at the actual operation settings follow, meaning 7 V WIENER and 2.1 V PP2 output. These studies included ten power cycles of the readout chips as well as reading the current consumption at full bias. In the un-configured state the FE-I4 power consumption can fluctuate slightly which can also be seen in Figure 3.11(a). However, a good module is expected to consume between 1 A and 2 A at operational voltage. A histogram showing all readout chips' currents, in the unconfigured and the configured case, can be found in Section 3.4.3. The last step of the basic electrical functionality checks was measuring the sensors' IV characteristics. The overall shape and absolute current consumptions give hints on mechanical incidents throughout the production, e.g. during handling, assembly or transportation. Hence, the IV results were always compared after each major step. The characteristic of Stave12 obtained in the SR1 Stave QA bench can be found in Figure 3.11(b). The main acception criterium was a stable current, not exceeding several μA, at the operational voltage, namely 80 V for planar modules and 20 V for 3D modules.

As a next step, basic scans were run from the DAQ panel to check the logical parts of the readout chips. To compensate production uncertainties and to adjust the electrical behavior according to the changing sensor signals over the lifetime of the detector, calibration circuits, very similar to the ones used in the FE-I3, were implemented. The registers and DACs mentioned in Section 3.2 were accessible using text based configuration files and were transferred to the chip at the start of each scan. To ensure a stable and reliable performance of the chips some preparative settings had to be entered or determined, respectively. The basic scans include register read back tests, digital and analog tests as well as first threshold and time over threshold scans. The digital test injects pulses in each pixel to an OR element right after the discriminator

(see Figure 3.2). Analog test hits are generated by a calibration voltage that charges the injection capacitors. The injected charge directly translates from that internal calibration voltage and the capacitances to:

$$Q = C_{\text{inj}} \cdot V_{\text{cal}} \quad \text{with} \tag{3.4.1}$$

$$V_{\text{cal}} = \alpha + \beta \cdot \text{PulserDAC} \tag{3.4.2}$$

where α is the offset and β the slope of the linear transfer function. The capacitance values of the two injection capacitors (one big, one small capacitor) as well as the slope of the injection voltage according to the VCAL[1] DAC (PulserDAC) value were measured for each chip on wafer level in the module production sites (University of Bonn and INFN[2] Genova). To determine the VCAL offset a special scan was run for each chip, measuring the discriminator activation curve once using only the small capacitor and once using both. From the differences in the results the offset was calculated and updated in the configuration file. Once these preparative steps had

	Threshold [e^-]	ToT [25 ns]	Temperature
3-Layer Pixel	3 500	30 @ 20'000 e^-	-13 °C
IBL (initial tests)	3 000	10 @ 16'000 e^-	+20 °C
IBL (operation)	1 500	10 @ 16'000 e^-	-15 °C

Table 3.1.: Comparison of 3-Layer Pixel and IBL calibration target settings.

been taken, threshold as well as time over threshold settings were adjusted and noisy pixels were masked in an automated fashion. Contrary to the former 3-layer Pixel detector, which uses a 7 bit DAC, a 5 bit DAC (TDAC) steers each pixel's threshold behavior in the FE-I4. The feedback current of the first preamplifier stage, however, is regulated by a 4 bit DAC (FDAC), just like in the FE-I3 case. The calibration principle stayed basically the same as for the 3-Layer Pixel Detector. In an iterative manner threshold and ToT settings were adjusted alternately for optimization. First, global settings were applied, then pixel wise settings followed. Based on known injected charges the pixel responses were evaluated by the readout system and the optimal settings were automatically saved in the configuration files. Afterwards, cyclic triggers were generated to identify noisy pixels, which were masked in case of a noise occupancy higher than 10^{-6} hits per pixel and bunch crossing. All these basic tests were performed at a module temperature of about 20 °C. All modules were re-calibrated to a threshold target value of 3 000 e^-. The time over threshold range covers up to 14 bunch crossings and a MIP creates a most probable signal of roughly 16 000 e^- in a 200 μm thick silicon sensor. Hence, the ToT calibration point is set to 10 bunch crossings for that reference charge in order to better resolve low charge signals. The target calibration values for

[1] **CAL**ibrated **V**oltage input line
[2] **I**nstituto **N**azionale di **F**isica **N**ucleare

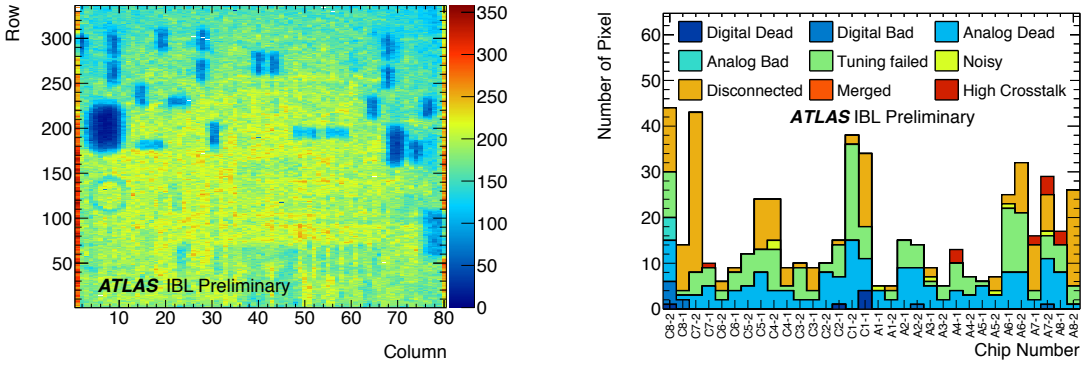

(a) (b)

Figure 3.12.: (a) 2D hit map of one chip on a planar module and (b) bad pixel analysis output for Stave12 [29], [40].

the ATLAS IBL in operation are 1 500 e^- threshold with identical ToT settings. A comparison to the 3-Layer ATLAS Pixel Detector values is depicted in Table 3.1. The calibration results were verified by running scans injecting various kinds of pulses and charges.

Eventually source scans (in some cases even cosmic runs) were performed to verify the functionality of the sensors, the calibration quality of the readout chips and to check the interconnections of both. A radioactive ^{90}Sr source illuminated each chip for 400 s to verify the sensor functionality and to identify disconnected bumps. The apparently low efficiency regions seen in the 2D hit map in Figure 3.12(a) correspond to the passive components mounted on the module flex (Figure 3.7). The increased number of hits in the outer columns corresponds to longer pixels (see slim edge design in Section 3.1.1). A 2D hit map of Stave12 is shown in Figure 3.13.

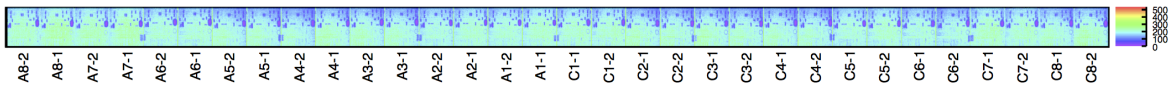

Figure 3.13.: Occupancy map from ^{90}Sr source scans on the entire Stave12.

Based on the digital and analog test results combined with the threshold and ToT calibration capabilities, crosstalk, noise and source scan performance, the number of bad pixels was evaluated for each module. In Table 3.2 the different failure modes are stated along with the corresponding scan types for identification and the criteria applied. The classification is exclusive, meaning that a pixel was defined as bad, as soon as one of the criteria applied, and it was deactivated for all following measurements. The failures are sorted by the execution of scans. Most of the failure modes are readout

chip specific, mostly resulting in a hit deficit or excess. Disconnected bumps were identified using source scans. Merged bumps and sensor failures are more challenging to identify. Here, the crosstalk scan was used in addition. This scan injects a rather high charge ($\sim 25\,000\,e^-$) into one pixel and triggers the readout of the neighboring pixels. In case of a fully depleted sensor and well isolated bump bonds no crosstalk is expected. In case of a merged bump it is likely to see many hits in a neighboring pixel combined with hit deficits or excesses in those pixels. An overview of all bad pixels in the case of Stave12 is shown in Figure 3.12(b).

Failure Name	Scan Type	Criteria
Digital Dead	Digital Scan	Occupancy $< 1\%$ of injections
Digital Bad	Digital Scan	Occupancy $< 98\%$ or $> 102\%$ of injections
Merged Bump	Analog Scan	Occupancy $< 98\%$ or $> 102\%$ of injections
	Crosstalk Scan	Occupancy $> 80\%$ of 25 k,e^- injections
Analog Dead	Analog Scan	Occupancy $< 1\%$ of injections
Analog Bad	Analog Scan	Occupancy $< 98\%$ or $> 102\%$ of injections
Tuning Failed	Threshold Scan	s-curve fit failed
	ToT Test	ToT response is 0 or 14 BCs
Noisy	Noise Scan	Occupancy $> 10^{-6}$ hits per BC
Disconnected Bump	Source Scan (^{90}Sr)	Occupancy $< 1\%$ of mean occupancy
High Crosstalk	Crosstalk Scan	Occupancy > 0 with 25 k,e^- injection

Table 3.2.: Classification of pixel failures [40].

In order to mimic possible conditions in the ATLAS Detector the most important operation was the calibration to a threshold of $1\,500\,e^-$ at a module temperature of -12 °C while the time over threshold setting is held constant. After the successful calibration to $1\,500\,e^-$, three thermal cycles were performed within the operable range of the TRACI, i.e. from -20 °C to +20 °C. Basic functionality checks (Digital, Analog, Threshold, ToT Scans) were performed after each cycle to look for changes due to mechanical stress, but all modules remained unaffected.

3.4.3. Stave Rating and Results Overview

In this section the QA results for all 18 staves are shown. Based on those the 14 best were chosen to build the IBL. The number of working channels was the major criterium for choosing a stave for installation along with stave planarity and sensor IV stability. The planarity is defined as the difference between the minimum and maximum height of a stave and did not exceed 340 μm in the IBL production which is within the envelope requirements of the carbon fibre (CF-K13C) IST inside the 3-Layer ATLAS Pixel Detector. A ranking and loading order overview of the ATLAS IBL staves can be found in Table A.1 in the Appendix.

LV and IV results of the production stave DCS groups (see Section 3.4.1) are shown in Figure 3.14. Figure 3.14(a) shows the DCS groups' power consumption in the unconfigured (blue) and configured (red) case. The distribution of values for unconfigured chips is wider due to not well defined settings in the FE-I4 when being powered up. The mean unconfigured current of a DCS group is 1.1 A ± 0.1 A. Configuring, however, resets the chips. Starting with a standard set of parameters, the distribution becomes narrower and the mean current consumption shifts to 1.5 A ± 0.1 A. These values are important for state monitoring and will serve as reference points for detector operation.

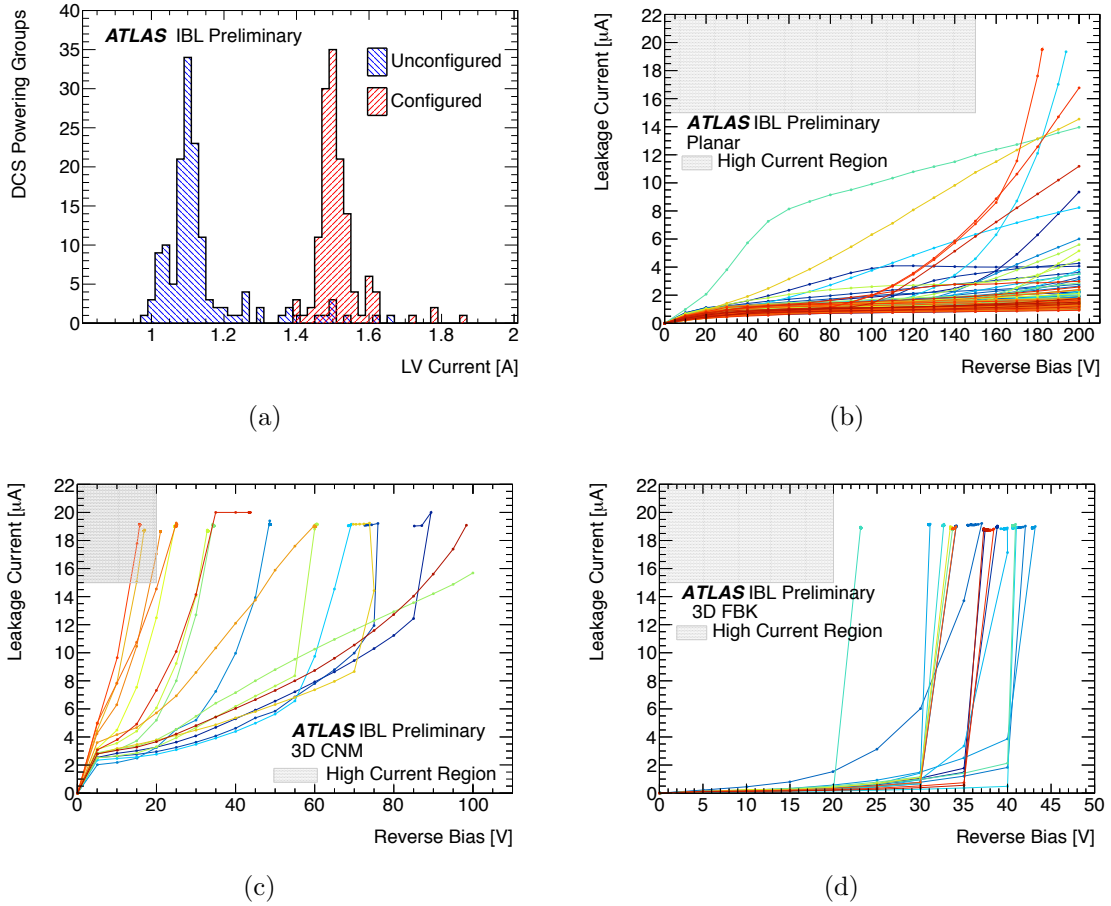

Figure 3.14.: (a) DCS groups' LV current consumption of all 18 staves and IV characteristics of (b) planar, (c) CNM and (d) FBK sensors of 17 staves at a module temperature of 20 °C [40]. The data set from Stave20 is missing due to a recording failure.

Figures 3.14(b), (c) and (d) show the IV characteristics of the sensor groups sorted by technology (see Section 3.1). By design the planar sensors have a rather high break down voltage of more than 200 V. For 3D sensors this is naturally lower because of

the pillars penetrating the bulk, resulting in a much shorter distance between the electrodes. In both cases high current regions were defined, represented by the grey boxes in Figures 3.14(b), (c) and (d). A leakage current of more than 15 μA was considered problematic at bias voltages lower than 150 V for planar and 20 V for 3D sensors, respectively. The depletion voltages are known to be smaller than that ($<$ 50 V for planar and $<$ 10 V for 3D), which leaves an adequate safety margin. The main focus here was to ensure a stable operation (i.e. current consumption of a few μA) and reliable operation of the sensors at the operational voltages of 80 V (planar) and 20 V (3D), respectively. The depletion was verified for all sensors with source scans as described in the previous section. The absolute current consumption scales with temperature and thus drops drastically for the operational temperature of -12 °C.

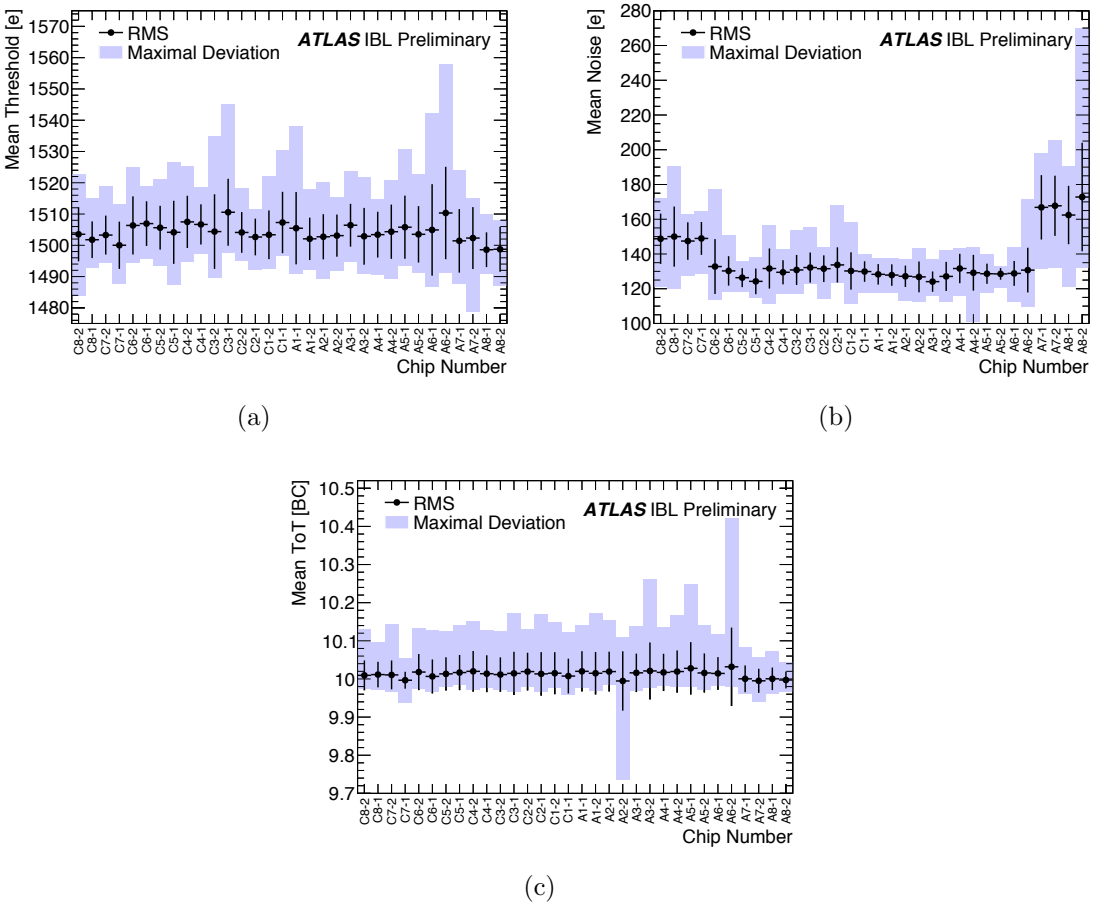

Figure 3.15.: Average (a) threshold, (b) threshold noise and (c) time over threshold distributions for all 18 staves as a function of chip number at a module temperature of -12 °C [29], [40].

In Figure 3.15 the threshold, derived noise and time over threshold distributions of all 18 production staves as a function of chip position are shown. The error bars represent

the RMS, the blue bars represent the minimum and maximum values found among the 18 staves. It is shown that all modules could be reliably calibrated to a relatively low threshold of 1 500 e^- with a maximal deviation of 40 e^-. The derived noise stayed below 200 e^- as was required for IBL production modules. The overall slightly higher noise (Figure 3.15(b)) on the 3D sensors was expected due to a higher sensor capacitance. The significantly increased noise on A8-2 comes from a module on one of the staves. However, this particular stave was not chosen for the IBL.

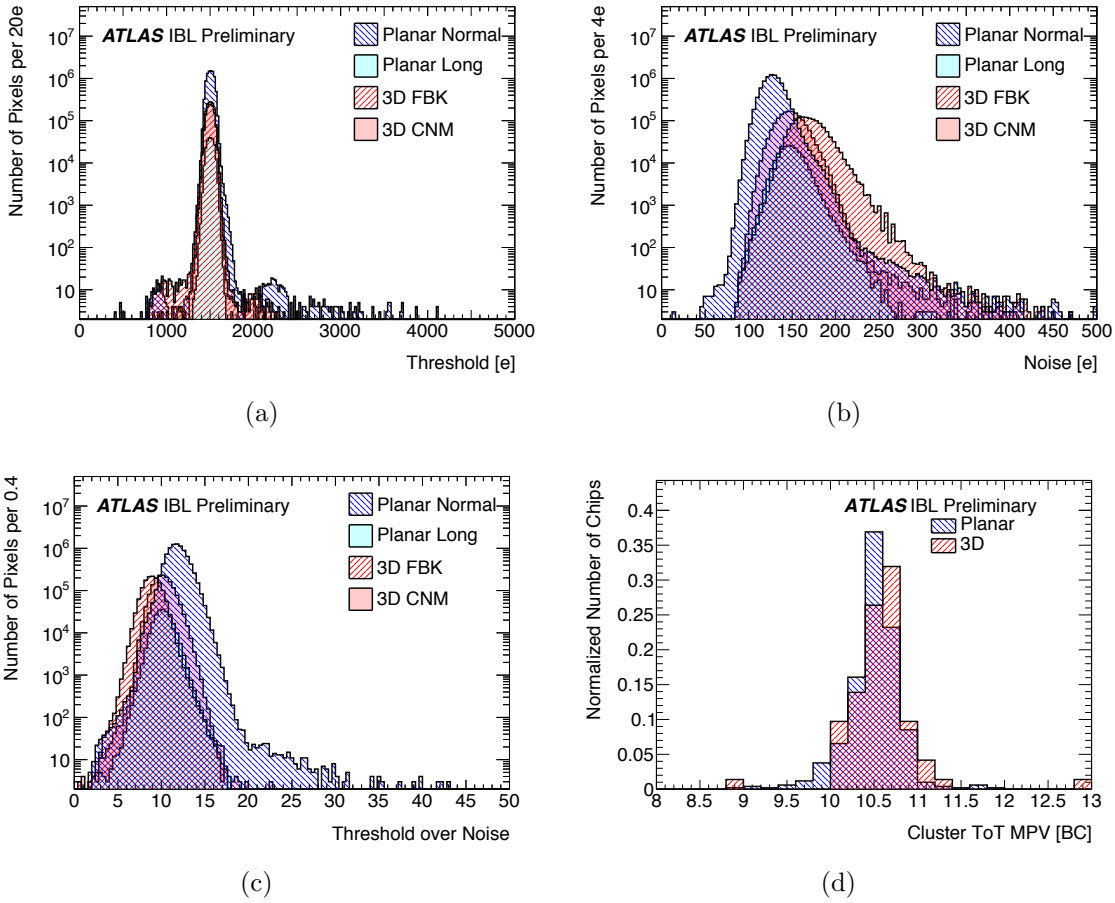

Figure 3.16.: (a) Threshold, (b) threshold noise, (c) threshold over noise distributions per pixel at a module temperature of -12 °C and a threshold calibration target of 1 500 e^-. (d) Chip wise time over threshold response for the 14 IBL staves at a module temperature of 20 °C and a threshold calibration target of 3 000 e^- [29], [40].

In Figure 3.16 the IBL calibration performance before integration is summarized. Figure 3.16(a) shows the overall pixel thresholds for the different pixel types. All types peak at 1 500 e^- threshold in a very narrow distribution with a dispersion of less than 50 e^-. Planar outer column and inter chip pixels are listed separately because of their longer size as can be seen in the derived noise plot (Figure 3.16(c)). The threshold over

Tuned Threshold	Pixel Type	Std. Dev. [e^-]	Noise [e^-]	Threshold over Noise
3 000 e^- at 22°C	Planar Normal	37	123 ± 10	25 ± 2
	Planar Long	58	146 ± 15	21 ± 2
	3D FBK	39	171 ± 25	18 ± 2
	3D CNM	40	149 ± 15	20 ± 2
1 500 e^- at -12°C	Planar Normal	42	129 ± 13	12 ± 1
	Planar Long	47	149 ± 16	10 ± 1
	3D FBK	46	171 ± 25	9 ± 1
	3D CNM	41	146 ± 16	10 ± 1

Table 3.3.: Threshold calibration summary for different pixel types for 18 staves. Listed values are the standard deviation of the threshold, mean noise and its standard deviation, and mean threshold over noise and its standard deviation [40].

noise is a key parameter in determining the quality of the IBL modules with respect to their operability at a given discriminator setting. The bigger this factor the less likely is contamination of noise hits in the sample of physics hits recorded during collisions. However, there is always a trade-off between fake hit reduction and hit efficiency, while the latter is increased for lower thresholds. A threshold over noise value higher than 5 was achieved for the majority of all pixels for a target threshold setting of 1 500 e^-, as can be seen in Figure 3.16(c). An overview of the standard deviation of the threshold, mean noise and its standard deviation, and mean threshold over noise and its standard deviation can be found in Table 3.3.

The physics occupancy in the ATLAS Pixel Detector b-layer was $\sim 5 \cdot 10^{-4}$ hits per pixel per bunch crossing at the end of Run 1 while the expected physics occupancy for the IBL is 10^{-3} hits per pixel per bunch crossing in early operation and higher in later years. In both cases, pixels with a noise occupancy rate higher than 10^{-6} hits per pixel per bunch crossing are referred to as noisy pixels and are disabled from data taking to ensure noise contamination in physics hits from collisions to be less than 0.5%. The fraction of noisy IBL pixels is less than 0.03% for the 1 500 e^- reference threshold calibration at -12 °C module temperature. The rate of noisy pixels in the 3-Layer Pixel Detector is twice as high at 0.06% for the 3 500 e^- operational threshold at the same module temperature. In Figure 3.16(d) the most probable values of the cluster ToT distributions per chip as responses to the electrons from the ^{90}Sr source are presented. It shows a very homogeneous signal response over all chips in the detector. For 3D sensors a slightly higher signal is expected and also observed since their thickness is around 230 μm compared to 200 μm thickness of planar sensors.

All 18 staves successfully passed the QA cut of 1% bad pixels. In fact, no stave showed more than 0.3% bad pixels. Figure 3.17(a) shows the average bad pixel fraction in blue for the installed 14 and in red for the 4 remaining staves as a function of η. It can be

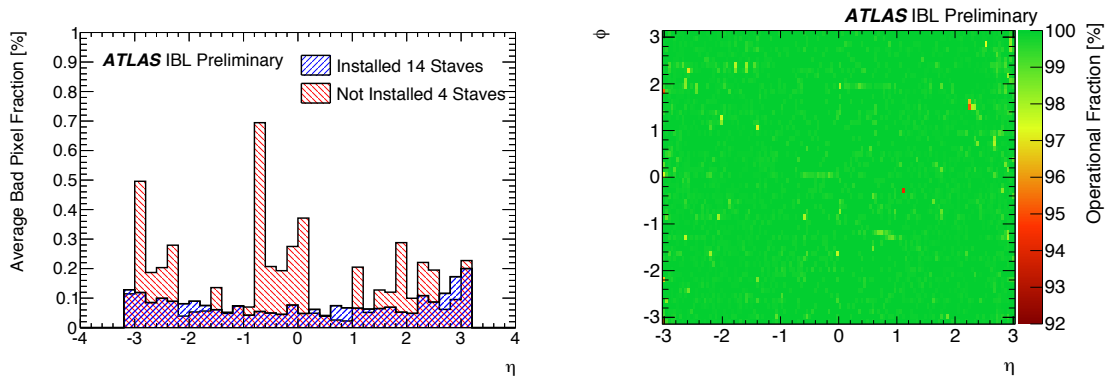

(a) (b)

Figure 3.17.: (a) Average bad pixel ratio distribution as a function of η for installed and not installed production staves and (b) the operational fraction of pixels in the η-ϕ plane for the 14 installed staves. Resolution: 128 bins in η from -3.03 to 3.03 that correspond to a bin width of 0.0473, 56 bins in ϕ from 0 to $2\,\pi$ that correspond to a bin width of 0.112 [29], [40].

clearly seen that already in the step of mounting modules onto staves the low η regions were covered with the best modules available. Based on the choice of the 14 staves with the lowest number of bad pixels, the number of operational channels in the ATLAS IBL is 99.9 % in total. The few defect channels are preferably distributed homogeneously in the η-ϕ plane. Thus, an η weighted ranking was applied on all staves. The resulting picture of the operational fraction of pixels in the η-ϕ plane for the 14 installed staves is displayed in Figure 3.17(b). More detailed QA results and a selection of encountered issues during the production, specifically double trigger responses, noise sensitivity on 3D sensors, charge calibration, weak differential driver output, oscillations on the low voltage supply lines and noise coupling on double chip sensors, can be found in [40].

3.4.4. ATLAS IBL Commissioning

At the beginning of 2014, the stave QA was finished and within one month 14 staves were integrated onto the IPT[1]. The entire IBL Detector package was fully assembled around the new beam pipe including all services one month later and was lowered into the ATLAS cavern beginning of May 2014. Once the detector was fully connected to all supplies, cooling and readout, it was re-calibrated stave by stave with the same readout system as in the clean room for the stave QA (RCE), whereas the QA module configuration files were used as starting points. All chips were operational and the calibration results, as shown in Figure 3.18, were comparable to the ones obtained in the QA setup. A comparison plot can be found in Figure A.1 in the Appendix. The

[1] **I**BL **P**ositioning **T**ube

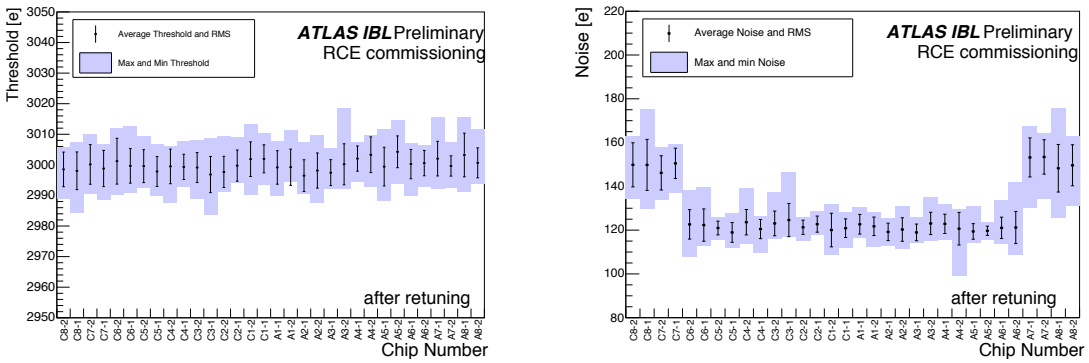

(a) (b)

Figure 3.18.: Average (a) threshold and (b) threshold noise distributions for all IBL staves as a function of chip number at a module temperature of 20 °C integrated into ATLAS [29].

next steps towards Run 2 of the LHC were the cold operation of the Inner Detector, the bake-out of the new beam pipe and combined cosmics data taking of all subsystems of the ATLAS Detector. One IBL stave was integrated into combined ATLAS cosmic data taking in the 5th Milestone Week (08 - 12th September 2014) which was the first big step for the DAQ chain commissioning. In the 6th Milestone Week (13 - 16th October 2014) all staves were participating in the data taking, although not simultaneously. 3-Layer ATLAS Pixel Detector hits were seen on tracks already in the online monitoring. ATLAS IBL hits were associated after reconstruction, multi bunch crossing read out for the IBL was shown to be functional. However, the data taking stopped earlier for the 3-Layer Pixel Detector and the IBL due to the beam pipe bake out.

3.4.5. Beam Pipe Bake-out and first Cosmic Results

The new beam pipe, which is integrated in the IBL package, needed to be baked out to reduce later thermal outgassing and to activate the NEG[1] (2 μm sputtered Ti-Zr-V) coating on the inside. This was a crucial procedure for the targeted LHC vacuum. To understand the conditions during the beam pipe bake-out, CFD[2] simulations were run (see Figure 3.19(b)). In addition to those, a real size IBL thermal mock-up (Figure 3.19(a)) was built and installed in CERN SR1 clean room. It was operated with a 1 000 W CO_2 cooling plant connected to stainless steel pipes running in aluminum staves in the mock-up.

Various heaters as well as temperature and humidity sensors were largely distributed over the entire mockup. To be as comparable as possible to the actual detector, also

[1] **N**on **E**vaporable **G**etter
[2] **C**omputational **F**luid **D**ynamics

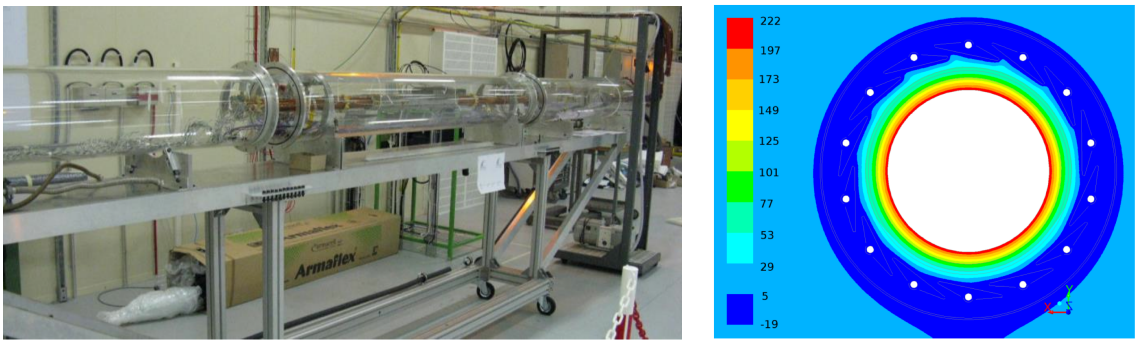

(a) (b)

Figure 3.19.: (a) Photograph of the thermal mock-up at CERN and (b) CFD simulations of the temperature distribution in IBL for the foreseen beam pipe bake-out [42].

the aerogel between the dummy beam pipe and the dummy IPT was removed over the length of the detector volume, namely 622 mm. In the detector, this was done to further reduce the radiation length. Only every second stave could be cooled in that setup. However, comparing the results from the cold staves to the CFD simulation during bake-out, one can see that they are in very good agreement (see Tab. 3.4). The beam pipe bake-out happened in two steps. First, a high temperature bake-out of the non-NEG coated components was done to degas impurities from their surfaces, while NEG coated regions stayed between 120-180 °C to avoid contamination of the material. Then, a second cycle was performed to activate the NEG coated regions at 220-230 °C. The stave temperatures, however, were not meant to exceed +35 °C (based on the adhesives' properties), which resulted in a substantial temperature gradient over just a few mm. With the help of the simulations and the mock-up it could be shown that the detector will remain unharmed during the bake-out if the coolant is set to -20 °C.

	Measurements	CFD calculations
Cooling lines	-19.2 °C	-19.2 °C
Cold staves	-18.7 °C	-17.7 °C
T_{IPT} at Z_0, north	+92.5 °C	+92.7 °C
T_{IST} at Z_0, north/south	+18.5 °C/+9.2 °C	+13.4 °C/+5.3 °C
Central heater dissipation at Z_0	212 W/m	154 W/m

Table 3.4.: Comparison of CFD calculations and measurements performed with the thermal mock-up [42].

Basic scans after the bake out showed no measurable change of the IBL's behavior. In

the 7th Milestone Week (27th November - 8th December 2014) the main goals were the consolidation of data taking, to provide good cosmics data for all 4 pixel layers and to test shift operation in Run 2 conditions. This time all 14 IBL staves had been routinely integrated into data taking. 3-Layer ATLAS Pixel and IBL hits on tracks were recorded with and without the presence of the ATLAS solenoid magnetic field. An event display showing SCT and 4-Layer Pixel hits is shown in Figure 3.20. The online monitoring is becoming operational and data quality flags for shift operation are being evaluated. However, one IBL 3D module stopped responding during that Milestone Week 7 (LI_S06_A7 chip 2). An LV supply current drop of 250 mA of the corresponding DCS group was observed. The time of current decrease is in coincidence with the start-of-run step of the ATLAS Detector, the moment that the configurations were sent to all modules. The module temperature was -25 °C, the magnetic field was on. This particular stave had been reworked before integration, but no module had been replaced in vicinity. Since the ATLAS Detector is fully closed, there is no physical access to the IBL. Thus, the investigational options are very limited. A possible cause for the communication loss could be a defect wire bond on the chip. It was found in earlier studies that transient currents in the various stages of IBL operation, i.e. module configuration, charge injection or triggering can cause a non-negligible amplitude excitation of the corresponding wire bonds in the presence of an external magnetic field, which can eventually lead to their destruction. Hence, it was decided to avoid a certain frequency trigger range in order to avoid any (further) possible damage. The fixed frequency trigger veto includes all frequencies from 2 kHz to 40 kHz. As a result the calibration scans will take longer and it is favored to take data with the lowest possible number of consecutive triggers. Run 2 is scheduled for March 2015 with first collisions being expected in May 2015.

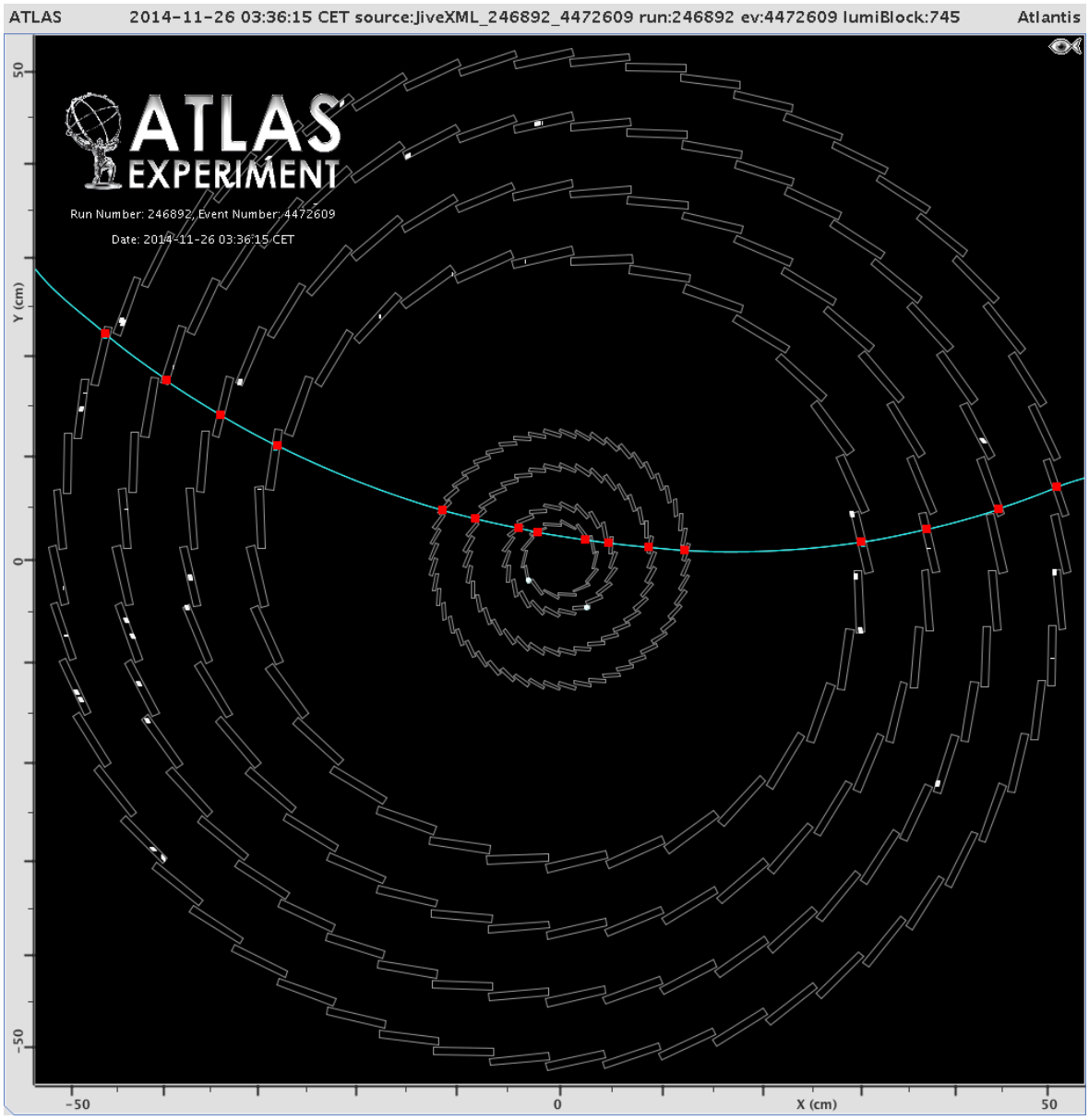

Figure 3.20.: Atlantis event display of cosmic ray event 4472609 from run 246892. A cosmic ray is shown passing through the IBL, the newly installed pixel layer of the ATLAS detector, in the presence of a solenoidal magnetic field. The IBL is the inner-most layer in the display. The three layers surrounding the IBL are the other layers of the Pixel detector, and the four outer-most layers seen are the Semiconductor Tracker (SCT). These data were recorded during milestone run 7 (M7) which is being used to re-commision the ATLAS detector for Run2 startup [43].

Somewhere along the line you gave up askin'
When it got a little too complex
But if you don't question what has been
Does it mean that you don't care what's coming next.
- Tina Dickow

Chapter 4

Sensor Characterization in Testbeam Measurements

Calibration capabilities of the readout chips as described in Section 3.4 are crucial for a reliable detector performance. However, the sensors' functionality can only be verified by incident particles. Source measurements (as shown in Section 3.4) are common since radioactive sources are available in most laboratories. For proper efficiency and tracking studies, however, preferably high energetic particles provided by accelerators, such as the PS[1] and SPS[2] at CERN, are used. In the scope of this thesis a 3D CNM sensor was investigated in a beam line at CERN SPS using the Timepix telescope. In the following section the experimental setup at CERN SPS North Area will be described. Subsequently, the characteristics of the Timepix telescope will be introduced in Section 4.2. The analysis framework used to evaluate the telescope's as well as the DUT[3]'s performance will be described in Section 4.3, including the merging of telescope and device under test data, track fitting and finally the corresponding performance measurements. The properties and calibration settings of the device under test will be depicted in Section 4.5. Finally, in Section 4.6 a new sensor characterization method based on the idea of Computed Tomography, evaluating the charge collection efficiency in a three dimensional manner, will be introduced.

4.1. Testbeam Setup at CERN SPS

The SPS is not only a pre-accelerator for the LHC but also serves various other experiments. It is operated in different run modes, so-called super cycles, which typically last around 40 s and usually provide beam to the North Area as well as the COMPASS[4] Experiment and the LHC. Here, the extraction of protons from the second long straight section via a transfer line with a 11 % slope to the surface into the North Area, an experimental hall 40 m above the main ring with a number of multi-purpose beam lines, will be depicted.

[1] **P**roton **S**ynchrotron
[2] **S**uper **P**roton **S**ynchrotron
[3] **D**evice **U**nder **T**est
[4] **CO**mmon **M**uon **P**roton **A**pparatus for **S**tructure and **S**pectroscopy

A single septum magnet as shown in Figure 4.1 is used in order to deliver high energetic particles at a constant rate for roughly 10 s . There, a vertically widened beam is separated into three parts. The main part travels through the vertical magnetic field and stays in the machine while the upper part enters a field free gap and continues straight on. The third fraction is lost in the magnet between the two gaps. This mechanism is called slow ejection [44], resulting in a spill over several thousand turns.

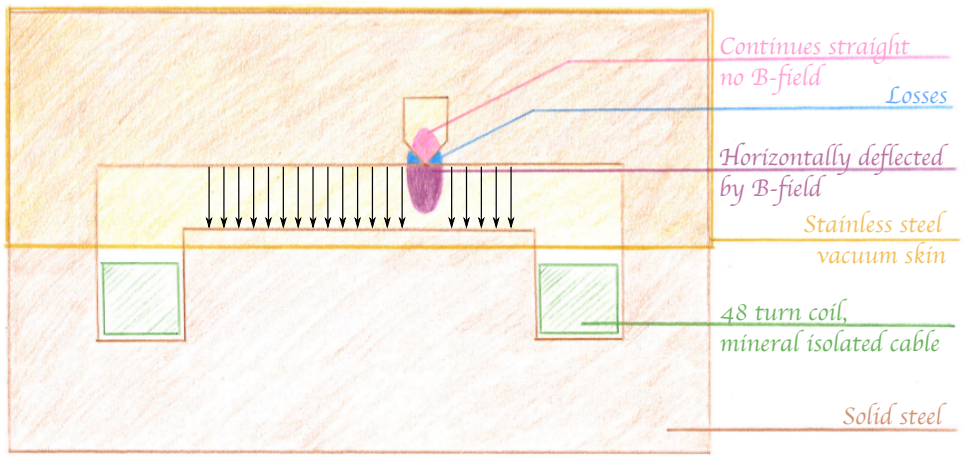

Figure 4.1.: Schematic view of a single septum magnet used at CERN SPS for proton ejection to the North Area. The black arrows show the direction of the magnetic field. The purple/blue/pink object represents the primary proton beam. Original taken from [44] and modified.

The 400 GeV proton beam is then split in three parts hitting the targets T2, T4 and T6. The resulting secondary beams consist mainly of attenuated protons from the primary beam (at $\sim$ 40 % of the initial intensity), hadrons (mostly pions) produced in hadronic interactions inside the Beryllium target, electrons from electromagnetic interactions as well as muons, originating from pion decays. Particle and momentum selection and thereby further splitting up into various beam lines is achieved by wobbling the beam, i.e. the primary beam hitting the target at a variable angle. In Figure 4.2 a wobbling example of the T4 target station is shown.

The measurements described in the following pages were performed at the H8 beam line which received pions at 180 GeV momentum from the T4 target. Inside the experimental area a beam telescope, namely the LHCb VELO[1] Timepix telescope [45], was installed to provide track information. In-between the planes a device under test was placed on a rotation stage. The device was tilted on that stage such that it would be rotated around the long pixel direction. The measurements were performed in May 2012, before the Long Shutdown 1.

[1] **VE**rtex **LO**cator

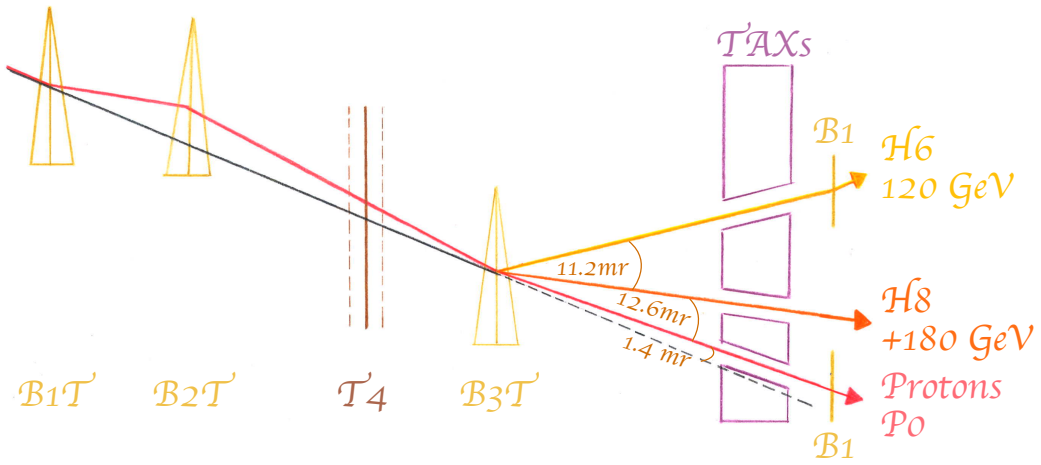

Figure 4.2.: T4 target station wobbling example splitting the proton beam in an attenuated proton beam P0 and two high energy hadron beams, namely H6 (120 GeV) and H8 (180 GeV). Original taken from [46] and modified.

4.2. The Timepix Telescope

For the LHCb VELO upgrade a fast, high resolution, shutter based beam telescope was developed for testing new generation sensors, supported by the Medipix collaboration and the AIDA[1] framework. Combining the two capabilities of the 300 μm thick Timepix silicon hybrid ASIC[2]s (providing information about either the deposited charge or the timing of the tracks) a pointing resolution of below 2 μm with a time stamping resolution of 1 ns can be achieved at a rate of reconstructed tracks of up to 7.5 kHz during an SPS spill. The Timepix telescope consists of nine planes hosting a 14 x 14 mm^2 matrix of 55 x 55 μm^2 pixels organized in 256 rows and columns. Eight planes operate in charge collection mode (ToT planes) and the last one in time of arrival mode (ToA[3] plane). The ToT planes are tilted by an angle of nine degrees in both horizontal and vertical axes in order to optimize the spatial resolution of the telescope. By that tilt an incident particle leaves a cluster signal of three hits which allows a sub-pixel pointing resolution at the position of the device under test. The ToA plane, however, is mounted perpendicularly to the beam to reduce charge sharing and thus minimize the discriminator response time. The telescope is arranged in two arms, the upstream one hosting four spatial planes and the downstream one hosting the other four spatial planes along with the timing plane. Each arm holds one RELAXd[4] [47] readout system, synchronized by an externally generated shutter trigger induced by scintillators at the extremities of the telescope.

The scintillator trigger is also provided to the devices under test to maximize flexibility.

[1] **A**dvanced European **I**nfrastructures for **D**etectors at **A**ccelerators
[2] **A**pplication **S**pecific **I**nterated **C**ircuit
[3] **T**ime **o**f **A**rrival
[4] high **RE**solution **L**arge **A**rea **X**-ray **d**etector

The device under test readout, on the other hand, can provide a busy signal to the telescope readout. Furthermore, the external trigger can by synchronized with an arbitrary clock which is essential for LHC-type detectors, i.e. not running in shutter mode but sampling at a fixed frequency. All triggers generated by the system will be collected and acquired by a high precision TDC[1] to enable offline synchronization of events. The data streams of the telescope and the device(s) under test are merged in a software step, the so-called amalgamation which will be described in Section 4.3.1. A schematic view of the telescope is shown in Figure 4.3.

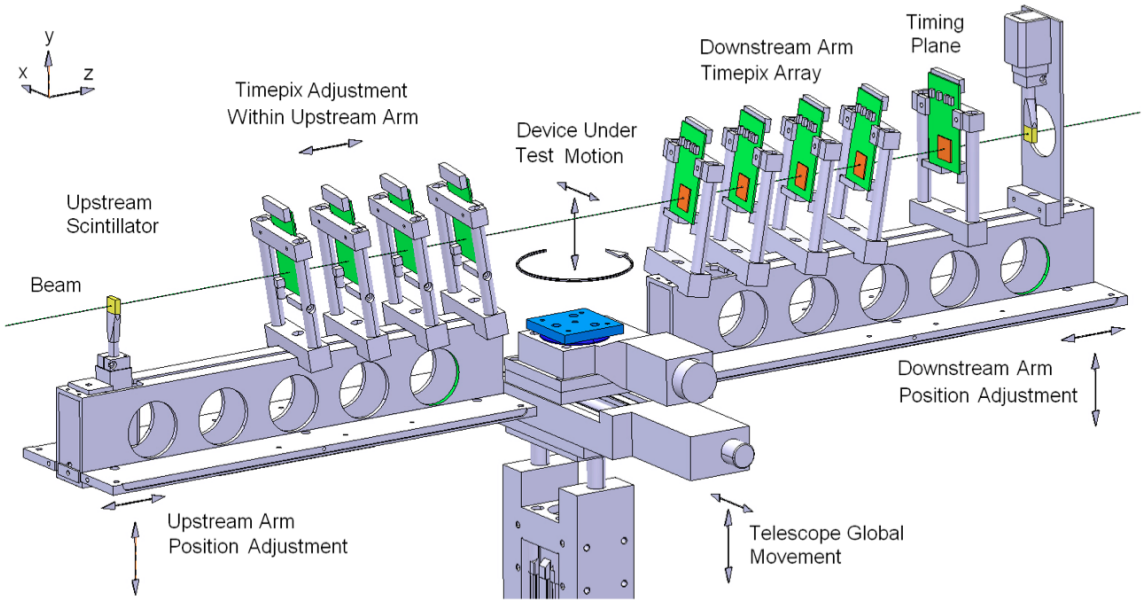

Figure 4.3.: Layout of the Timepix Telescope mechanics, pixel planes and scintillators with respect to the beam axis [48].

4.3. Testbeam Analysis Framework

The raw data from the telescope and the DUT is processed within the ROOT/C++ based Timepix analysis framework in two steps. First, a low-level event building and conversion to a ROOT based format is performed. This step is called amalgamation and will be described in Section 4.3.1. Then, in the second step, the formatted data is read in and clustering as well as track finding are performed on a frame-by-frame basis. Based on those reconstructed tracks analysis algorithms can be implemented to investigate the telescope's as well as the DUT's properties. The track reconstruction will be introduced in Section 4.3.2.

[1] **T**ime to **D**igital **C**onverter

4.3.1. Amalgamation

The only logical connection between the Timepix telescope and the DUT is a trigger signal (TTL) from the telescopes trigger logic, which is provided to the FE-I4 DAQ system. The matching of tracks using timestamps is then done offline in the amalgamation step.

To index the FE-I4 data a function is called that first reads in all converted FE-I4 raw files that correspond to the considered telescope run. Each raw file contains all FE-I4 hits (trigger data, data header and data records) from one SPS spill and contains a timestamp at the beginning of the file. The lines containing trigger data in that file come with an assigned trigger ID. For each trigger 4 consecutive bunch crossings are read out to include all hits, which occurred within the expected time window. Each hit comes with a bunch crossing ID (BCID) that defines the hits' timestamp. The data record lines contain the row and column of each hit as well as the ToT response of the corresponding pixel. Once all files are read in, the timestamps of the first and the last file are compared to the corresponding telescope timestamps. If there is an overlap the amalgamation goes on by trying to match FE-I4 frames to TDC frames. For this purpose, the times between the TDC triggers need to be identical to the times between triggers received by the FE-I4. If that is the case the frames are considered as matched and the data from the FE-I4 is considered as indexed. Based on that data the event files in the ROOT tree format are built. Example plots of the amalgamation output can be found in Figure B.5 in the Appendix.

4.3.2. Track Reconstruction

Based on hits in the telescope planes available in the event file so-called tracks are built, which can be projected onto the DUT. This is done in three steps: the clustering of raw hits, then the pattern recognition and eventually the track fitting.

The clustering algorithm identifies hits in neighboring pixels and combines them to clusters. Hits are not binary but associated with a ToT value depending on the amount of deposited charge by a traversing particle. Hence, the actual hit position is calculated for each cluster based on the center of gravity by applying ToT based weighting factors to each pixel hit. From preceding calibration scans a linear relationship between ToT and deposited charge was found. Pixels with ToT counts that significantly deviate from the expected MIP induced Landau mean, i.e. with ADC counts smaller than 85 or higher than 925, were excluded as these are usually caused by hadronic interaction, δ rays (compare Section 1.3.1) or noisy pixels.

The pattern recognition searches in adjacent telescope planes for nearest neighbors in a fixed radius. Instead of investigating all possible combinations it is implemented in a binary search manner [49] to reduce computation time. In addition, it takes multiple scattering in the telescope material into account. Thereby, the radiation length of each telescope plane ($\approx 2.6\,\%$) and the track momentum (here 180 GeV) have to be

considered. Typically, the tracks get deviated by up to 10 μm between the two telescope arms in case they are 300 mm apart. The algorithm stores all cluster candidates and then selects the ones with the smallest χ^2 to assign to the track. A cut of 14 on the maximum cluster size is applied. Finally, the resulting clusters are handed over to the Track Fitter.

The track fitting is based on the least squares technique. In the xy plane at $z = 0$ (z being the beam direction) a four dimensional state vector $\vec{v}$ represents the tracks. It is defined as:

$$\vec{v} = \begin{pmatrix} x \\ t_x \\ y \\ t_y \end{pmatrix} \tag{4.3.1}$$

with x and y being the horizontal and vertical coordinates (compare Figure 4.3) and t_x and t_y being the corresponding slopes of the track with respect to the beam axis. To obtain a clean residual distribution a probability cut on the χ^2 per number of degrees of freedom (n_{dof}) can be applied. The number of degrees of freedom can be calculated as:

$$n_{\text{dof}} = 2n - 4 \tag{4.3.2}$$

where n is the number of points included in the fitting in the xy plane. The constant 4 is subtracted due to the four fit parameters x, t_x, y and t_y.

4.4. Telescope Performance Results

To provide the best possible tracking resolution on the DUT plane, the telescope position and configuration has to be verified and understood. The alignment of the individual planes needs to be adjusted in software to obtain an optimal track fitting. A measure of alignment quality is the residual, the difference between the calculated track intercept projected onto a plane and the measured hit position of the corresponding sensor. For a well aligned sensor the residual distribution should peak around 0 while the standard deviation σ of the distribution should be

$$\sigma = p/\sqrt{12} \tag{4.4.1}$$

with p being the pitch (pixel size), according to Equation 1.3.2. In the case of the Timepix chip used here, the pitch is 55 μm in both directions which yields in an expected residual width ($\sigma_{x,y}$) of around 16 μm. This is the case for the ToA plane (I10-W0108) as this one is mounted perpendicularly to the beam. The other eight planes show much smaller standard deviations as they are tilted such that larger cluster sizes enable accurate ToT weighted clustering and thus improve the telescopes spatial resolution.

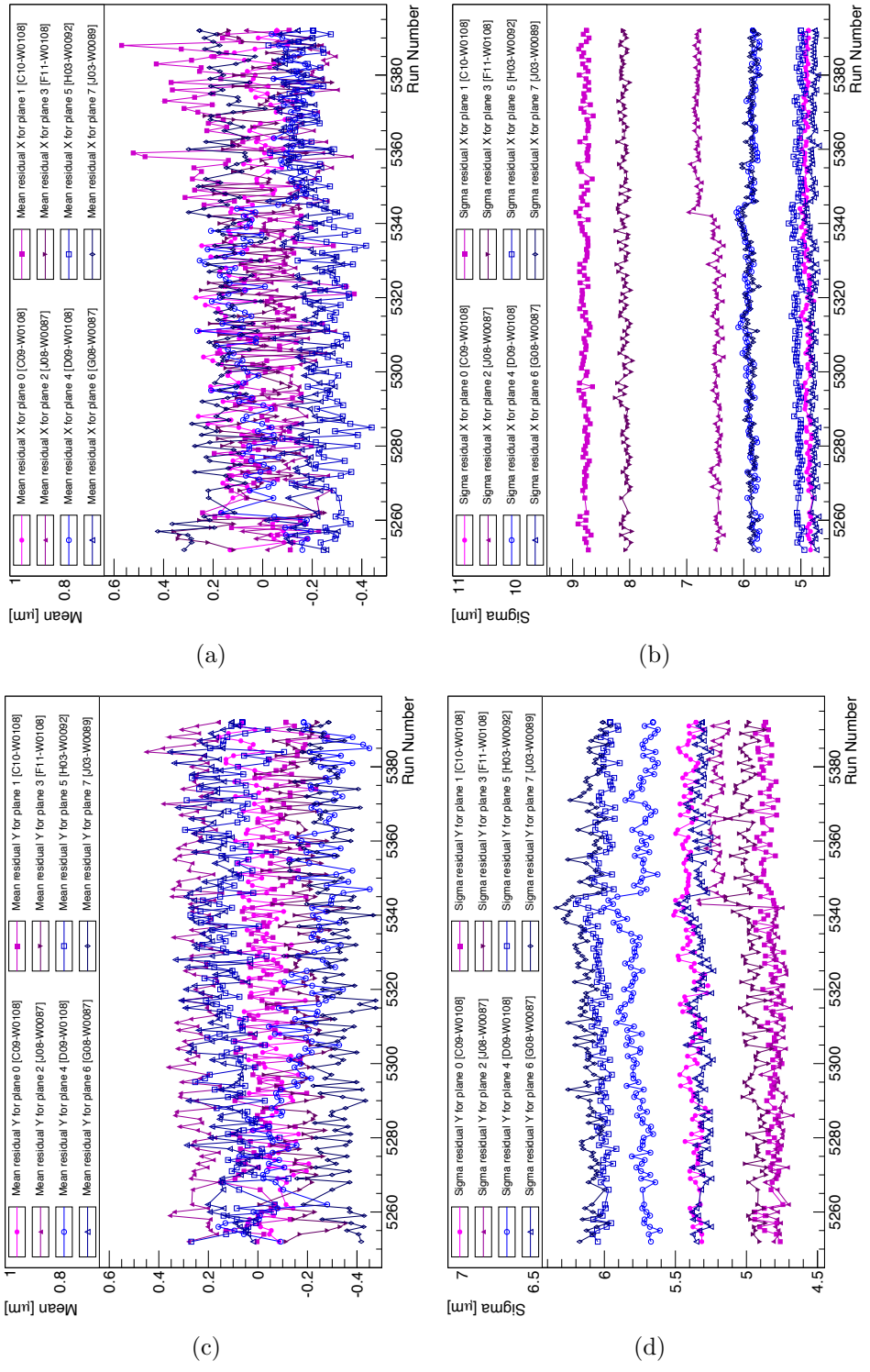

Figure 4.4.: Timepix telescope residuals (a) mean in x, (c) mean in y, (b) σ_x and (d) σ_y over entire data set. The deviation after Run 5343 can be explained by a modified setup configuration for taking data in the other angle direction.

An overview of all nine planes and their measured z positions can be found in Table 4.1. Since the beam is almost perfectly parallel the z position is not part of the automated alignment procedure but kept fix at the measured value. In general, one differentiates between biased and unbiased residuals. Is the corresponding plane included in the process of track fitting, the calculated residual is called biased while projections on planes excluded from the track fitting are unbiased. For the sake of computing time and effort only biased residuals are presented here, all the more so since the scope of this thesis is not the full characterization of the Timepix telescope.

1st Telescope Arm		2nd Telescope Arm		ToA Plane	
Name	z [mm]	Name	z [mm]	Name	z [mm]
C09-W0108	0	D09-W0108	520	I10-W0108	635
C10-W0108	23	H03-W0092	543		
J08-W0087	46	G08-W0087	566		
F11-W0108	69	J03-W0089	589		

Table 4.1.: Names and z positions of the nine Timepix telescope planes used.

However, studies about the residuals' stability were carried out. The alignment was not perfectly stable over the entire data taking period due to several interventions and the conditions in the testing hall, e.g. moving ceiling cranes and other experiments. Therefore, a new telescope alignment was performed for each run individually. The results can be found in Figure 4.4. The mean of the residuals varied by less than $0.6\,\mu$m around 0 and the σ of the distributions was between $4.8\,\mu$m and $9.0\,\mu$m for the spatial planes. Some planes show a very small jump in their residual σ's between Run 5342 and Run 5343. That can be explained by a major intervention carried out between the two arms, namely remounting of the DUT to alter the rotation direction for upcoming runs. The data for the ToA plane is not shown in Figure 4.4 as the σ of the residual distribution deviates significantly from the ones of the spatial planes due to its orientation as described above. The corresponding residual distributions of the individual planes using the example of the first run (Run 5252) can be found in Figure B.3 and Figure B.4 in the Appendix.

4.5. The Device Under Test

As device under test a $230\,\mu$m thick 3D CNM sensor was used, bump bonded to an FE-I4A readout chip. It was part of the prototyping runs for the ATLAS IBL project. Details on the sensor were described in Section 3.1. The assembly was glued and wire bonded to a single chip carrier card (SCC), hence the name SCC99. An example picture of such a card hosting a single FE-I4A chip and a sensor is shown in Figure 4.5. The

Figure 4.5.: Photograph of an FE-I4A Single Chip Card.

card was connected via an ethernet cable to a modified HSIO board attached to an RCE crate, the same kind as was used for the quality control measurements during the IBL production as described in Section 3.4.1. The reverse sensor bias (-30 V) was applied via a LEMO connector, the upper left connector in Figure 4.5. The supply voltages for the FE-I4A readout chip (1.5 V for the analog and 1.2 V for the digital circuits) were applied via a Molex connector.

4.5.1. Calibration of the DUT

The RCE system was used to calibrate the module in the same fashion as described in Sections 2.2 and 3.4.2. An iterative calibration of global and pixel specific settings lead to the results shown in Figure 4.6. The target values for the discriminator threshold and the time over threshold response during the prototyping phase for the ATLAS IBL can be found in Table 4.2. The successful threshold calibration of SCC99 is

	Threshold [e^-]	ToT [25 ns]	Reference Charge [e^-]
SCC99 (3D CNM)	1500	10	20'000

Table 4.2.: Calibration target settings for SCC99 during the testbeam data taking period.

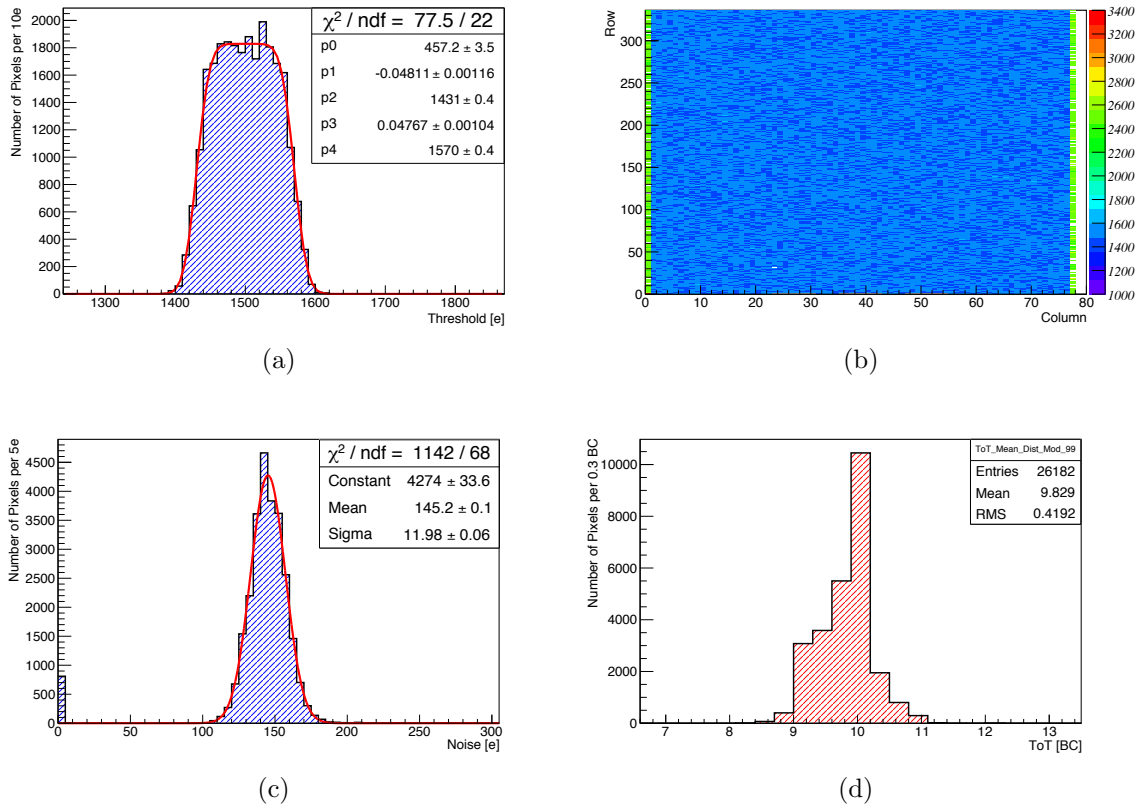

Figure 4.6.: SCC99 (a) threshold distribution, (b) threshold 2D map, (c) noise and (d) ToT distributions at room temperature.

shown in Figure 4.6(a). The distribution is well centered around the target value of 1 500 electrons with a σ of 70 electrons. It is not Gaussian but box-shaped according to the step width of the pixel threshold calibration DAC (TDAC) in the FE-I4A (LSB[1]). Deviation from the exact box-shape come from slight variations in the pixel registers. Hence, the step function is convoluted with Gaussian error functions on the edges of the distribution. The resulting fit function ends in:

$$f(x) = p_0 \cdot (1 + \mathrm{erf}(p_1 \cdot (p_2 - x))) \cdot (1 + \mathrm{erf}(p_3 \cdot (p_4 - x))) \quad (4.5.1)$$

$$\text{with} \quad \mathrm{erf}(x) = \frac{2}{\sqrt{\pi}} \cdot \int_0^x e^{-t^2}\, \mathrm{d}t. \quad (4.5.2)$$

The fit parameters are shown in the statistics box in the histogram. Figure 4.6(b) shows a 2D map of the pixels' threshold values. One can clearly see the homogeneous distribution in the center of the chip. The outermost columns show much higher values.

[1]**L**east **S**ignificant **B**it

This is a feature of the prototype version of the readout chip which had various analog pixel flavors implemented in different columns. Those outermost columns will not be taken into account for the following analysis of the testbeam measurements. The noise derived from the threshold s-curve fitting (compare Equation 2.2.1) can be found in Figure 4.6(c). It follows a Gaussian distribution

$$g(x) = p_0 \cdot \exp\left(-\frac{(x-p_1)^2}{2p_2^2}\right) \tag{4.5.3}$$

with p_0 being the height (constant), p_1 the mean (145 electrons) and p_2 the σ (12 electrons) of the distribution. The time over threshold evaluation is rather coarse due to the limited ToT resolution in the FE-I4. However, the pixel-wise ToT response peaks clearly around the target value of 10 bunch crossings as shown in Figure 4.6(d).

4.5.2. Recorded Data

During one of the last testbeam periods before the Long Shutdown 1 of the CERN accelerator complex a ten hour slot was made available at the H8 beamline of the SPS. In total 140 data sets which contain between 30 455 and 273 437 timestamped tracks at various DUT rotation angles were recorded. The DUT (SCC99) was mounted such that the long pixel direction was oriented along the y axis and the short pixel direction along the x axis, respectively (compare coordinate system in Figure 4.3). The device was successively rotated around the long pixel direction from 0 ° to 90 ° in 1 ° steps and for comparison also in the other direction from 0 ° to -90 ° in 2 ° steps. The goal was to collect one million track segments in the DUT for in depth charge collection efficiency studies. A detailed overview of all runs, rotation angles, total numbers of tracks, tracks in time overlap, timestamped tracks and tracks containing FE-I4 data can be found in Table B.1 in the Appendix.

In general, not all scintillator triggers correspond to valid tracks through the telescope. In addition, a false shutter open setting in the telescope lead to a partial saturation of the ToA plane for a significant fraction of tracks. The rate of successfully timestamped tracks was 53 % over all runs on average while the average track association rate within the timing overlap was 82%. Furthermore, only a fraction of collected triggers holds valid DUT information on track, especially at high rotation angles where the DUT incidence plane becomes smaller than the trigger window. It varies from 300 for rotation angles close to 90 ° up to 147 000 for the 0 ° run. The total numbers of tracks, tracks in time overlap, timestamped tracks and tracks containing FE-I4 data for all DUT rotation angles are shown in the upper plot in Figure 4.7. A curve representing the estimated number of track segments in the DUT was added. It assumes perfectly efficient particle detection based on the pixel's geometry (see next section). From that curve it can be seen that the number of track segments is quite stable over all runs, but a factor 5 smaller than aimed for. The lower plot in Figure 4.7 shows the ratios of tracks in time overlap, timestamped tracks and tracks containing FE-I4 data with respect to the total number of tracks.

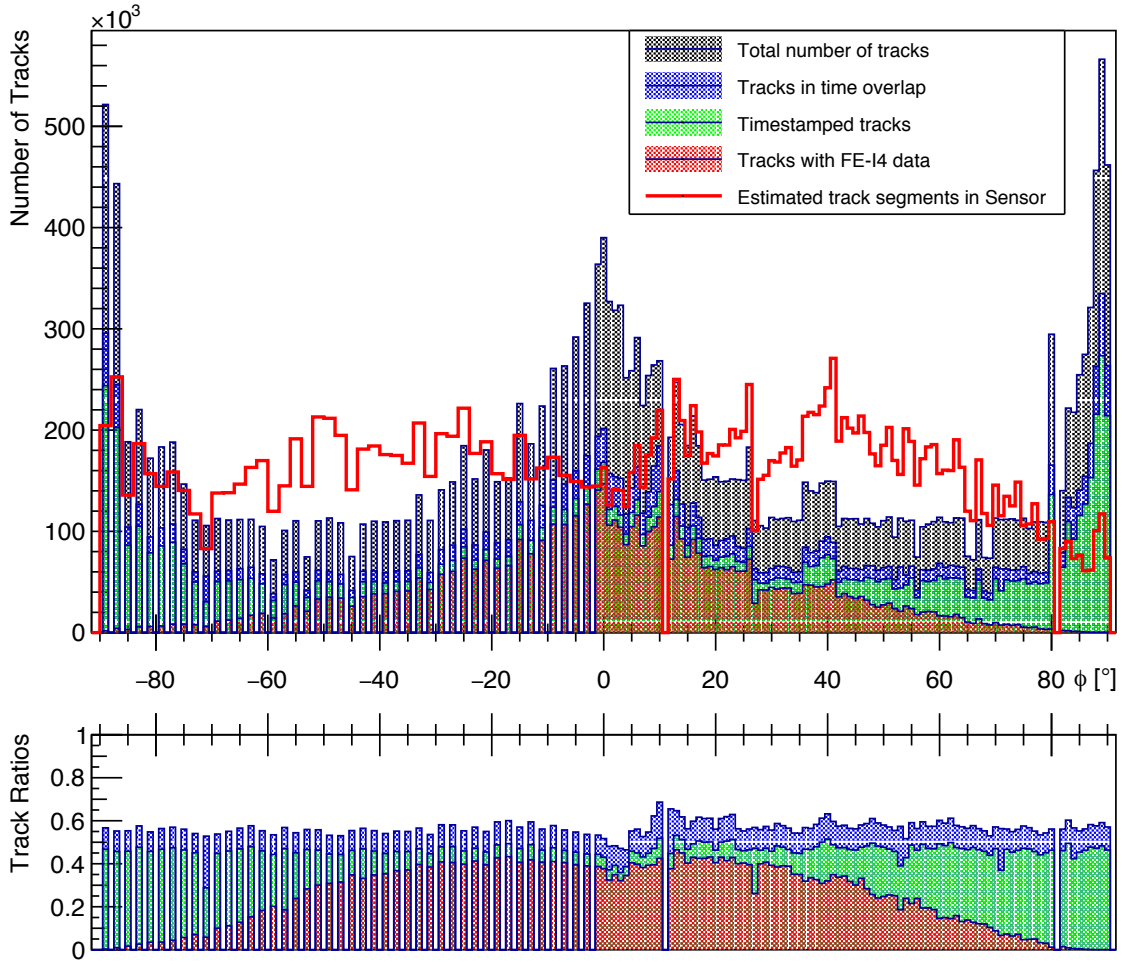

Figure 4.7.: Total numbers of tracks, tracks in time overlap, timestamped tracks, tracks containing FE-I4 data for all DUT rotation angles and an estimation on track segments in the DUT, collected in May 2012 testbeam campaign (upper plot), and ratios of tracks in time overlap, timestamped tracks and tracks containing FE-I4 data with respect to the total number of tracks (lower plot).

4.5.3. Clustering Algorithm

Depending on the incident angle φ of a traversing particle and due to charge sharing more than one pixel can register the created charge signal. The resulting pixel clusters have to be identified as such and their charge responses have to be combined in order to reasonably analyze the data. Basic predictions on the expected cluster sizes can be made based on the sensor's geometry. In Figure 4.8 an example trajectory of an incident particle inside a pixel sensor is shown. From that sketch various parameters can be derived. One is the total track length l_{track} inside the sensor:

$$l_{\text{track}} = t \cdot \cos\varphi \tag{4.5.4}$$

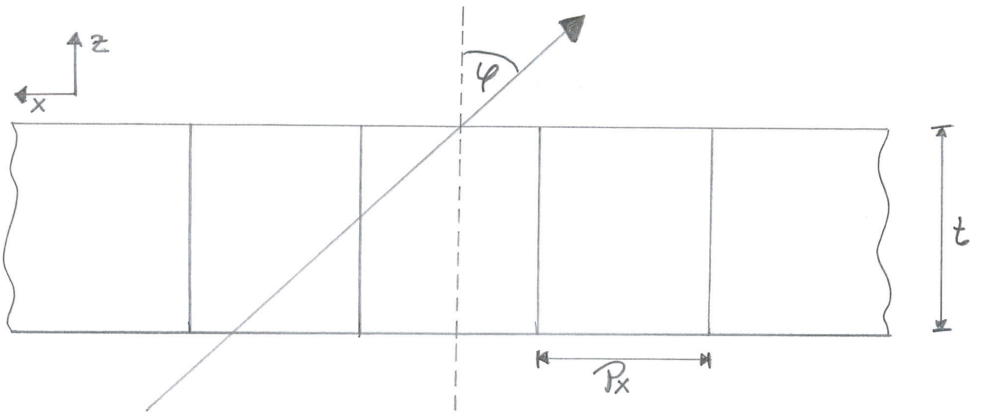

Figure 4.8.: Sketch of the geometry of a track inside a pixel sensor. Not to scale.

with t being the thickness of the sensor. The resulting expected cluster size l_{cluster} can be calculated to

$$l_{\text{cluster}} = \left\lfloor \frac{t \cdot \tan \varphi}{P_x} \right\rfloor + 1 \tag{4.5.5}$$

with P_x being the pixel pitch in x. The pixel dimensions of the DUT used for these measurements are summarized in Table 4.3.

	P_x [μm]	P_y [μm]	t [μm]
SCC99 (3D CNM)	50	250	230

Table 4.3.: Pixel geometry values for SCC99 (3D CNM).

First, as a preparative step for following analyses, only the DUT data was evaluated. For this purpose, a standard clustering algorithm was used: It collects all hits from the hit map and stores them in a list. The first entry serves as a seed for the first cluster. If there is a hit in a direct neighbor to that pixel it is associated to the cluster. The corresponding hit is then deleted from the hit list. This is repeated until there are no more neighboring hits. The resulting cluster is stored. If there are remaining hits in the hit list, the next hit serves as a new seed for a new cluster. This procedure is repeated until the hit list is empty.

For small incident angles this way of simple clustering is sufficient. However, for larger angles two challenges emerge: It may occur that not all pixels along the particle's trajectory detect the corresponding charge signal, because of short travel distances in each pixel (row direction) and charge sharing effects. This results in what will be called split clusters. In the simple clustering algorithm those would falsely be recognized as individual clusters. Another effect that distorts proper clustering are

hadronic interactions and δ-electrons, which also leave long tracks in the detector but are not to be accounted for the original track signal. Example DUT hit maps showing long split clusters and a hadronic interactions can be found in Figures B.6 and B.7 in the Appendix. Since the particle beam at CERN SPS is almost perfectly parallel, split clusters can be differentiated from δ-electrons by simply requiring a maximum cluster height (in this case number of FE-I4 columns) of 3. The remaining split clusters are merged in a recursive manner: First, a simple cluster is built. If that first cluster is seemingly complete, the algorithm searches for an additional hit within a certain range, in that case 7 pixels in the row direction and 2 pixels in the column direction. If there is another hit, a second cluster will be built around that new seed. If the second cluster is seemingly complete, the algorithm goes on searching for additional hits in the defined range, etc. This is done until there are no more hits in range of any of the previous clusters. Finally, all found small clusters will be merged into one. The cluster width is then defined as the distance between the two outermost pixels. A plot showing the number of cluster fragments per angle can be found in Figure B.8 in the Appendix.

In Figure 4.9 the determined cluster widths depending on the incident angle are shown. The result of the simple clustering algorithm can be found in Figure 4.9(a). It can be seen that the cluster widths do not increase anymore at incident angles higher than $70\,^\circ$ due to split clusters. In the result shown in Figure 4.9(b) the modified clustering algorithm was used. There, a much better agreement with the theoretical function (see Equation 4.5.6) can be found. The deviation from the theoretical curve can be explained by various impact factors. First of all, the theoretical function does not take the pixel calibration threshold into account and thus overestimates the expected cluster width. Furthermore, the cluster widths per angle follow a distribution rather than a concrete value due to charge sharing and non-linear charge deposition. It was also found that the distributions are not perfectly symmetric in the two directions. The angles stated for each run correspond to the settings on the rotation stage. However, the setup, including the telescope, the rotation stage and the DUT on the rotation stage, was not perfectly aligned with the beam. Thus, a phase shift of $\phi = 1.3\,^\circ$ was determined based on the results seen in Figure 4.9(b). The eventual expected cluster width function was implemented as:

$$l_{\text{cluster}} = \left| \frac{t \cdot \tan\left(\varphi + \phi\right)}{P_x} \right|. \tag{4.5.6}$$

The maximum possible number of rows are 336 in the case of the FE-I4. That is true for an adjusted rotation angle of $\varphi = 89\,^\circ$ as can also be seen in Figure 4.9(b). After that the cluster width decreases again. An obscurity visible in Figure 4.9(b) is a remaining accumulation of smaller clusters between $80\,^\circ$ and $90\,^\circ$. Those are no data taking artifacts but can be explained by multiple scattering on PCB components and connectors mounted on the SCC[1] (compare Figure 4.5). Since the particles creating these clusters are highly deviated from the original trajectory, they will not be detected by the second telescope arm. Hence, they will not be counted as valid tracks.

[1] **S**ingle **C**hip **C**ard

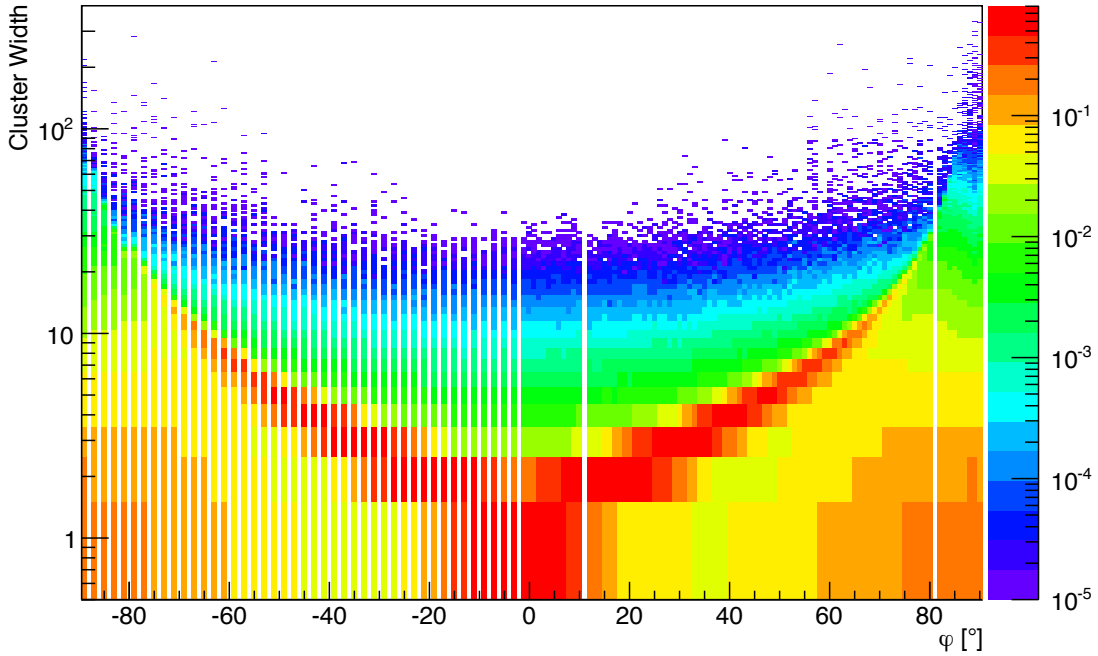

(a) Simple clustering algorithm.

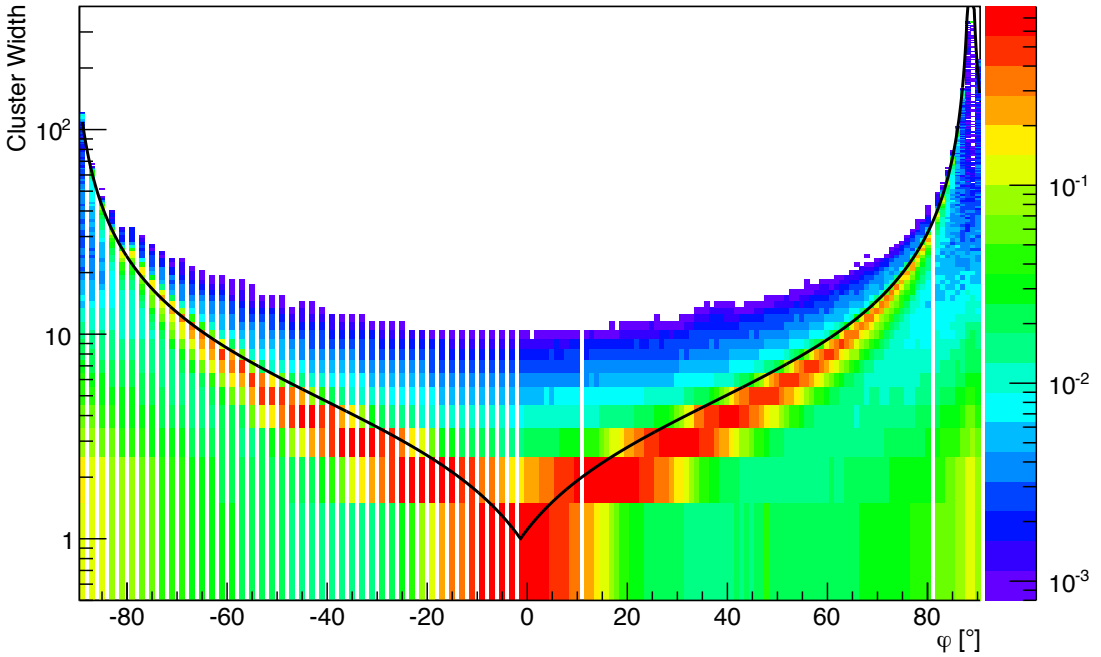

(b) Modified clustering algorithm accounting for split clusters.

Figure 4.9.: SCC99 cluster widths over entire data set showing the results of (a) a simple clustering algorithm and (b) an algorithm which merges split clusters with a radius of 7 pixels in the row direction and 2 pixels in the column direction. In addition, an expectation curve is shown.

4.5.4. DUT Performance Results

During data taking an online monitor was available, counting the number of collected triggers and showing a 2D hit map of the DUT as well as the Level 1 distribution, in order to verify a stable recording of data. A DUT 2D hit map is shown in Figure 4.10(a) using the example of the first run (perpendicular incident), Run 5252. Only a fraction of the DUT shows hits as the trigger scintillators attached to the Timepix telescope cover an area of roughly $1\,\mathrm{cm}^2$ while the active area of the DUT is around $4\,\mathrm{cm}^2$. The Level 1 trigger (see Section 3.2) distribution of all recorded hits can be

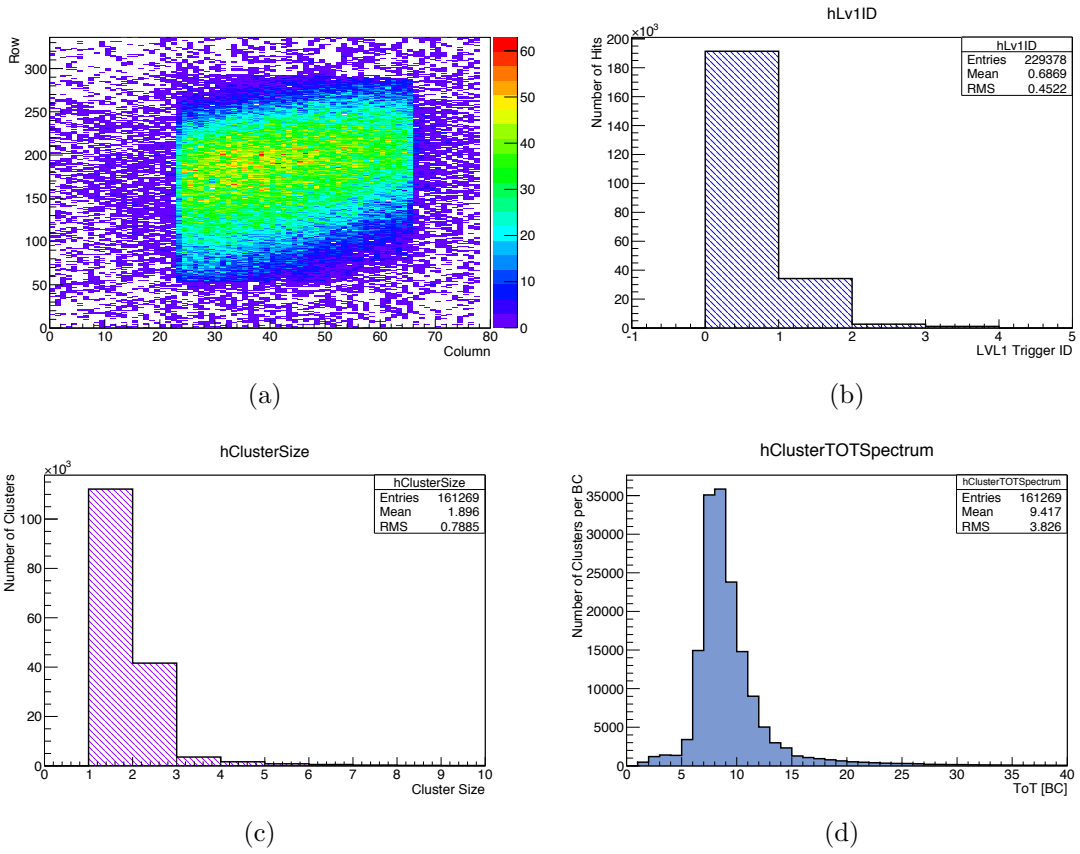

Figure 4.10.: SCC99 (a) hit map, (b) LVL1 trigger, (c) cluster size and (d) cluster ToT distributions in Run 5252, perpendicular incident, FE-I4 data on track.

found in Figure 4.10(b). In all runs, four consecutive triggers were sent to the chip for each scintillator trigger in order to collect all hits within the expected trigger window. The timing parameters were adjusted such that most particle hits correspond to the first trigger signal. In later analysis steps single hits were associated to clusters. Figure 4.10(c) holds the cluster size distribution for Run 5252. As expected for particles traversing the sensor perpendicularly, mostly one-hit clusters occur. Due to charge sharing also two-hit clusters were likely. The associated cluster ToT is presented in

Figure 4.10(d). The calibration setting was 10 bunch crossings response for a reference charge of 20 000 electrons. However, the expected number of created charge carriers of a MIP passing through 230 μm silicon is 18 000 electrons. Thus, the most probable value of the Landau distribution was expected to be around 9 bunch crossings which is the case here.

4.5.5. DUT Residuals and Alignment

The spatial position of the DUT was determined in a dedicated alignment step. In particular, the z position was fixed, as it also was for the telescope planes, to a measured value (280 mm) as the beam is almost parallel. The track angles deviate less than 0.007 ° from 0 ° in x and in y. The parameters used for the alignment are the x and y directions as well as the rotation angles around all three axes, α_x, α_y and α_z. A Minuit/MIGRAD minimizer scans these alignment parameters, ± 4 cm in the spatial coordinates and $\pm 2\pi$ for the angles, and thereby searches for the smallest possible residuals in x and y.

The quality of the alignment can be deducted from the sensor residuals in the same fashion as described in Section 4.4. Figures 4.11(a) and 4.11(b) show the DUT's residual distributions in x and y, respectively. The width in x is relatively small (short pixel pitch 50 μm) and the shape can be approximated by a Gaussian distribution as in the case of the Timepix telescope residuals. The width in y is significantly bigger since that is the long pixel direction (250 μm). The distribution follows a box shape with Gaussian distributions convoluted on the edges caused by charge diffusion. The function can be approximated in the same manner as the threshold distribution in Equation 4.5.1. Both fit functions are shown in Figures 4.11(a) and 4.11(b), respectively.

The result in y generally meets the expectations for an incident angle of $\varphi = 0\,°$. The width of the distribution corresponds to the size of a pixel while the standard deviation is 76 μm. As can be seen from Figures 4.11(d) and 4.11(f) the y residuals do not depend on the tracks' global positions after alignment. However, there is a visible skew in the correlation plots of the x residuals and the tracks global x and y positions (see Figures 4.11(c) and 4.11(e)), which results in a wider residual distribution than expected for the short pixel direction.

Several approaches were pursued to improve the alignment: Since the automated alignment procedure always yielded similar results independently of start parameters, a manual angle adjustment was attempted. There it was found that optimizing one correlation inevitably lead to worsening of the others. Example residual distributions and correlations with the global coordinates for rotating the DUT +1 ° around the z axis can be found in Figure B.9 in the Appendix. Even combined variations of all three angles did not lead to an optimal set of alignment parameters. A possible explanation could be vibration or instabilities in the setup, which would result in constant DUT movements and thus smearing of residuals. Considering the mounting structure of the DUT, a holder attached to a base plate on the rotation stage, one would expect the distribution to fan out in one direction. However, this was not discovered in the data

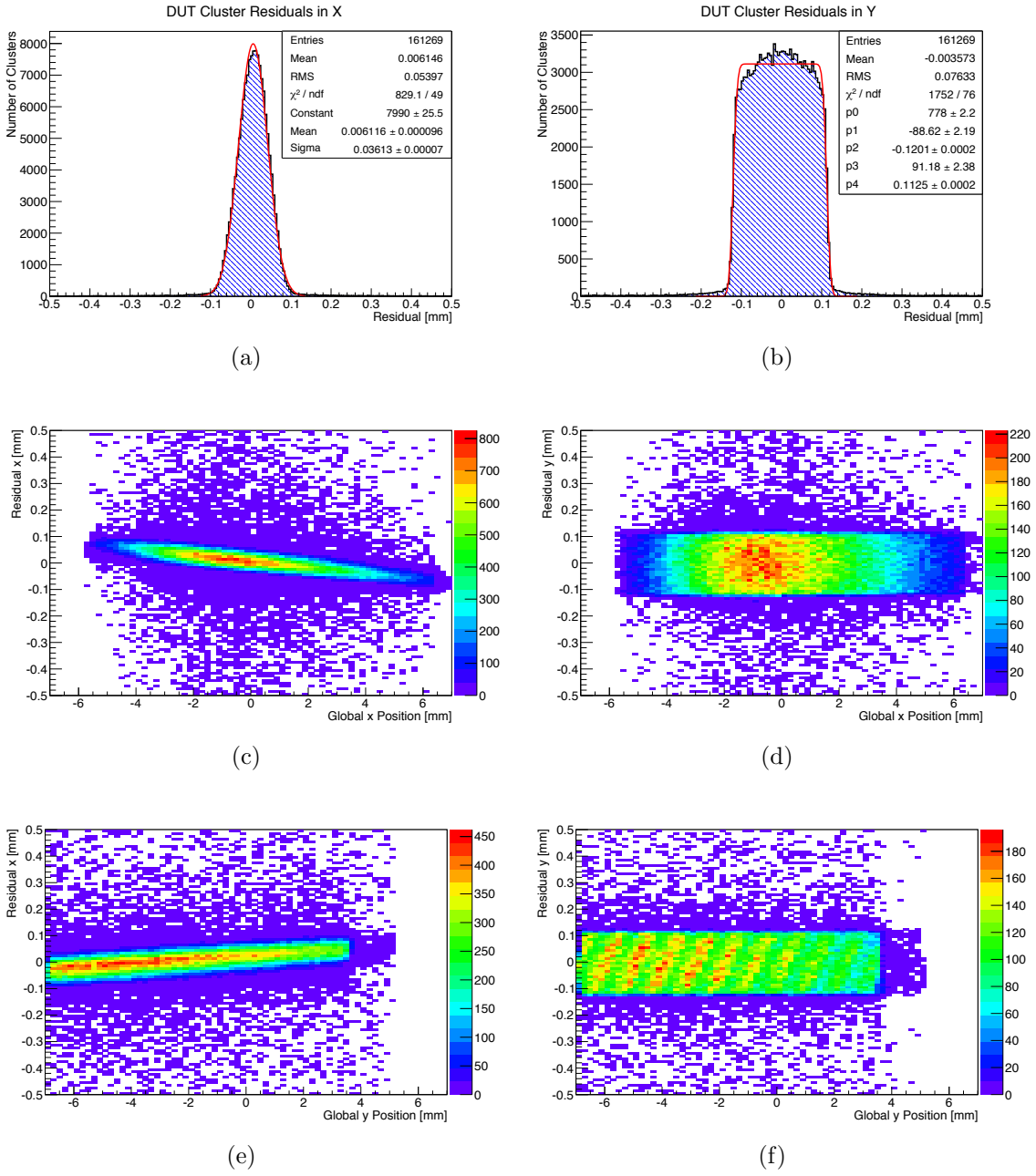

Figure 4.11.: SCC99 (a) x and (b) y residual distributions and the corresponding correlations with global track coordinates in Run 5252, perpendicular incident.

and therefore excluded as a possible explanation. Another cause could be mechanical deformation of the sensor due to thermal stress and tension, induced during the sensor production or flip-chipping process. In order to investigate a possible time dependent change of positioning, the data set (Run 5252) was split into different sub-sets as the stripes in Figure 4.11(f) indicate a regular dependence, which might have been correl-

ated with the spill structure of the SPS beam. However, no time dependence on the residuals was observed. Finally, a shift along the z direction of 5 mm was applied to the DUT in order to cover the possibility of track angle effects. In Figure B.10 in the Appendix a comparison of both x and y residual distributions for both cases are shown and no significant change is observed.

4.5.6. Charge Collection within a Pixel Cell

The track information provided by the Timepix telescope was used to determine the tracks' entry points in the DUT plane at a sub-pixel resolution. The collected charge signals were evaluated for 500 sub-pixel regions for Run 5252, where the DUT was mounted perpendicularly to the beam. This division yielded in a statistic of roughly 300 ToT entries for each sub-pixel. The numbers of hits for each sub-pixel are shown in Figure 4.12(b). The resulting ToT distributions were fitted with a convolution of a Landau and a Gaussian function to achieve the best possible approximation. The MPV[1]s of the ToT distributions can be found in Figure 4.12(c). They varied between 6.4 and 7.9 bunch crossings. The regions showing less collected charge match with the regions of smaller electrical fields created by the bias electrodes, which are displayed in Figure 4.12(a).

The resolution in the row direction, however, is limited by the distortion in the x residual (see Figure 4.11(a)). Thus, the lower efficient regions are smeared out, appearing as columns rather than dots as would be expected from the lithography sketch. A projection of the most probable charge values onto the column direction is shown in Figure 4.12(d) to level out this smearing effect. It can be seen that the collected charge drops in the regions of the bias electrodes. Towards the pixel edge there is a dip in collected charge which recovers partly at the extremity of the pixel cell. The dip can be explained by the increased charge sharing probability close to the edge, which leads to the signal being collected also by the neighboring cell. If the collected charge in one of the pixels is below the adjusted threshold, it will not be registered in that pixel, which results in a one-hit cluster. At the outermost part of the pixel, the charge shared between the two exceeds the threshold in both pixels and thus the entire induced signal is detected.

[1] **M**ost **P**robable **V**alue

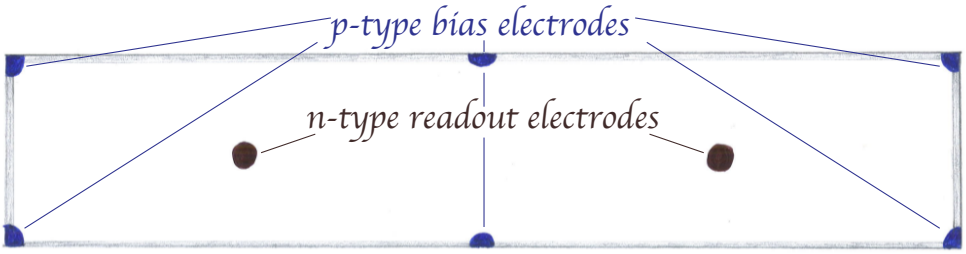

(a) Lithography sketch of a 3D pixel showing the electrodes' positions.

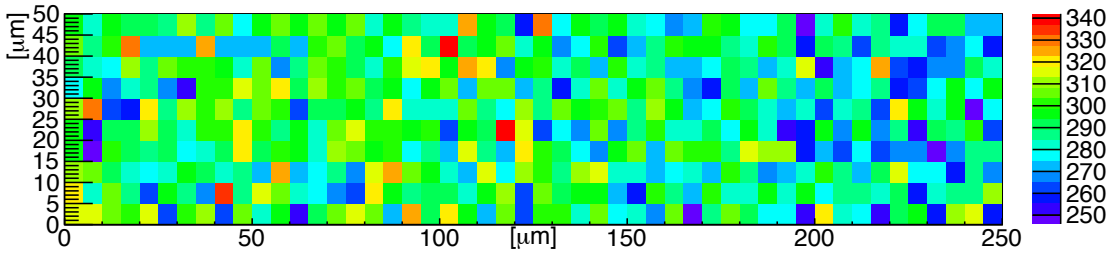

(b) 2D Pixel Hit Map

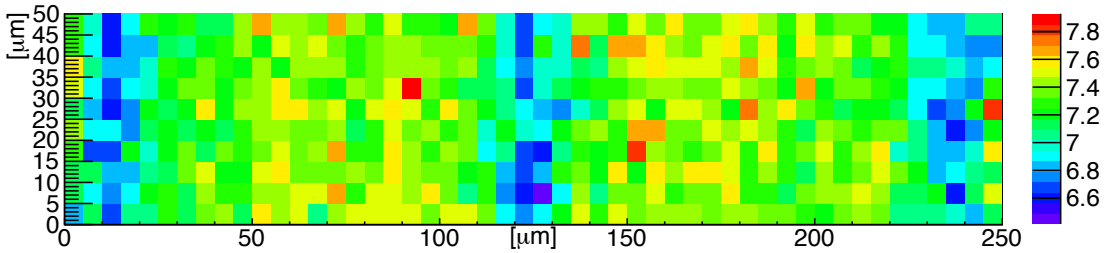

(c) 2D Pixel ToT MPV Map

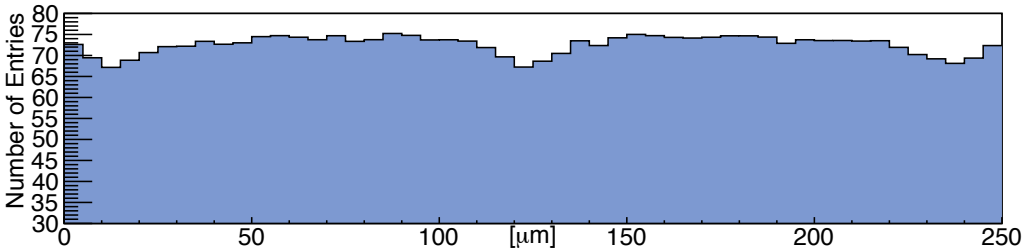

(d) Projection of Pixel ToT MPV Map

Figure 4.12.: SCC99 pixel cell results: (a) lithography sketch, (b) 2D hit map, (c) most probable collected charge values and (d) projection of most probable collected charge values. Results from Run 5252, perpendicular incident.

4.6. 3-Dimensional Charge Collection Efficiency Studies

Up to now the main sensor characterization criterium were the 2-dimensional hit and charge collection efficiencies. However, these are not sufficient for fully understanding sensors with a more complex electrical field, e.g. 3D or diamond sensors. Thus, a new method of investigating a sensor's properties in depth was evaluated. The concept of these 3D charge collection efficiency (3DCCE) studies will be depicted in the following sections.

4.6.1. The Basic Idea

The idea is based on the principle of Computed Tomography (CT) scans, which are widely used in medical applications. 2-dimensional absorption images from x-rays are recorded by specialized detectors in order to measure an object's density. Multiple absorption images at various angles are collected by rotating the source as well as the detector around the object. Those are collected and merged into a 3-dimensional picture, a so-called sinogram. This representation of absorption functions plotted against the rotation angle and distances along the detector is then filtered in a next step. Finally, in the step of the back projection, the original 3-dimensional image of the object's density is reconstructed. This principle using the example of a 2-dimensional object is shown in Figure 4.13(a), while the rotation of source and detector is drafted in Figure 4.13(b).

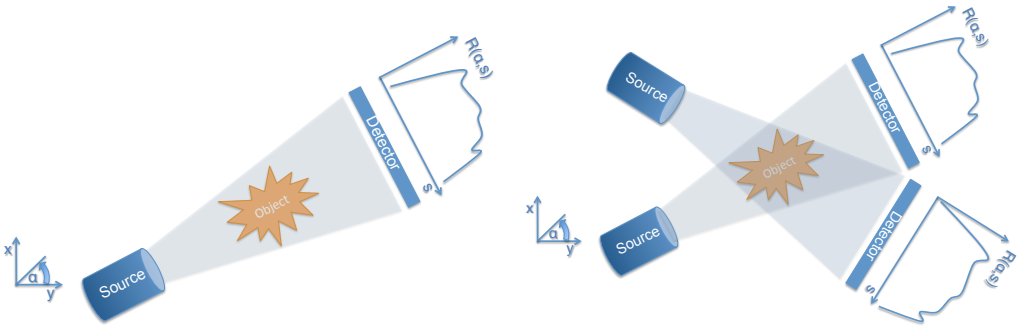

Figure 4.13.: Sketch of the basic principle of Computed Tomography measurements.

In general, absorption images from x-rays are sufficiently obtained with very low statistics as the photons are generated following a narrow Gaussian distribution. That is beneficial in terms of exposure time and image quality. In the case of silicon sensor characterization, however, the interesting parameter is not the density of the material but the charge collection efficiency in individual regions. Thus, the measurement principle was adapted such that the DUT is object and detector at the same time, collecting

charge signals instead of absorption images, while the parallel high energetic particle beam (here 180 GeV) provided by CERN SPS served as the source. Information on the incident position of the particle tracks was provided by the beam telescope. A sketch of the setup is shown in Figure 4.14.

The charge deposited in silicon sensors follows a distribution which is a convolution of the Landau distribution and a Gaussian function. This is taking into account the fact that, in silicon, the electrons are not free but are bound to the atoms of the crystal. Thus, a high level of statistics is required to obtain appropriate fit results.

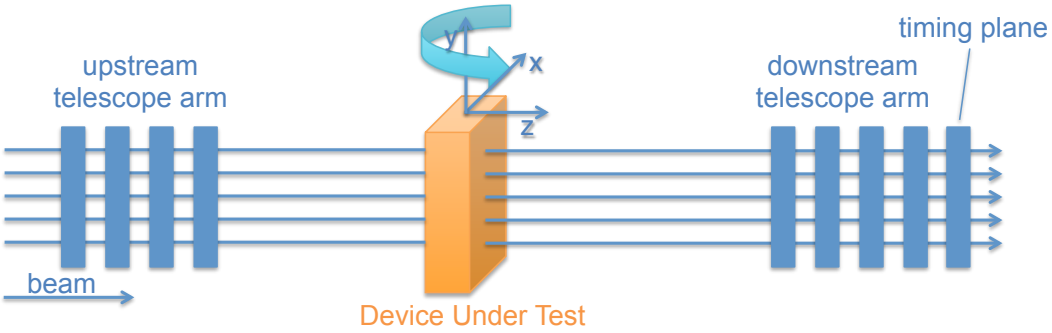

Figure 4.14.: Sketch of the testbeam setup including the rotation of the DUT for tomography-like measurements.

As a first attempt for this new method, data as described in Section 4.5.2 at various rotation angles of the DUT was taken. The idea was to project the data from the entire pixel matrix into one standard pixel to improve the statistics. This standard pixel is to be divided further into several sub-pixels, also called voxels. The sub-pixel ToT information is then to be filled into a sinogram, filtered and the resulting image is to be projected back in order to obtain a 2-dimensional projection of local charge collection inefficiencies inside the sensor bulk.

4.6.2. First Simulation Approaches

As a preparative step a simple and basic custom simulation software was developed, based on C++ and Root, in order to understand the analysis chain and the required resolution on the DUT information. For medical applications several simulation tools are already available. However, these tools assume x-rays penetrating an object, projecting the absorption images onto a detector. The goal of this work was to calculate the theoretical charge deposition based on knowledge of beam parameters and detector (e.g. silicon) properties. For test purposes a 2-dimensional case of a plane detector with regions of varying efficiencies as shown in Figure 4.16(a) was examined. The sample is a bulk piece of silicon with 100% efficiency containing 100 voxels of variable sizes (ranging from 2 to 20 μm) and variable efficiencies (ranging from 90% to 99%), useful to test the precision of the reconstruction.

A sketch of the simulated setup is shown in Figure 4.15. The angle α is scanned in the interval of [0, 180] in steps of 0.5 ° while x was variated between -213 μm and 213 μm in steps of 2 μm. Various numbers of events per voxels were investigated. The sinogram shown in Figure 4.16(b) was built based on the most probable values of the collected charge distributions containing 100 events per voxel. The reconstructed results for 1 000 and 10 000 events can be found in Figure 4.16(c) and Figure 4.16(d), respectively.

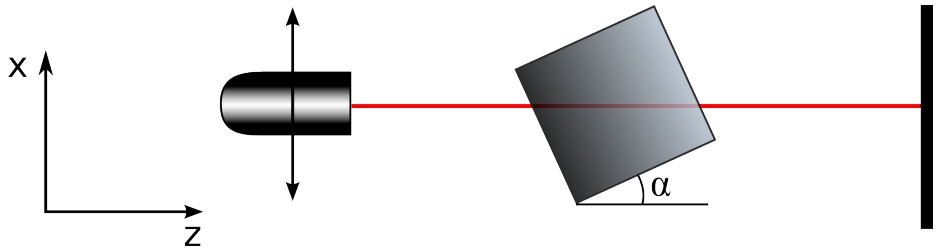

Figure 4.15.: Sketch of the tomography simulation setup [50].

It was found that the numerical calculations, e.g. the various convolutions of histograms, which are used to mimic actual data, are computationally intensive and the back projections are very susceptible to the filter settings. The complex chain of analysis steps, especially on the reconstruction part demands a much deeper examination than was achievable in the scope of this thesis. Thus, the results presented here serve as premature studies that give hints on the required statistics. However, it could be shown that the approach of signal reconstruction using convolutions of the Landau distribution and a Gaussian function is feasible, as well as the method of using the detections capabilities of the DUT.

4.6.3. Issues and Lessons Learned

It appeared that this new method of sensor characterization bears more challenges than expected, on the simulation as well as on the data analysis side. The computing effort for high resolution simulation studies is immense in case the convolutions are not performed analytically. The numerical calculations, however, might be improved by using Fast Fourier Transforms.

The main obstacles in the data reconstruction are statistics, alignment issues and ToT resolution. At an incident angle of $\varphi = 0\,°$ roughly 147 000 tracks containing FE-I4 data were collected, which permitted a 2-dimensional sub-pixel resolution ToT evaluation (see Figure 4.12) with a 5 μm resolution. For an investigation in all angle an even finer sub-division of a pixel would be necessary as the projected area increases by tilting the sensor. However, the number of tracks per voxel in the data taken in that campaign is not sufficient for such a study. Furthermore, the FE-I4 alignment is a

crucial part of the analysis. However, it turned out that this particular sensor seems to have physical features, which challenge a proper alignment in x and y at the same time. In general, it is advisable to first investigate the DUT with respect to common testbeam characterization techniques to ensure a stable data taking for following in depth studies. The third challenge will be the ToT resolution of the FE-I4. Individual regions of slightly lower charge collection efficiencies will be difficult to distinguish due to the 4-bit resolution, where one ToT count corresponds to roughly 2 000 electrons charge signal.

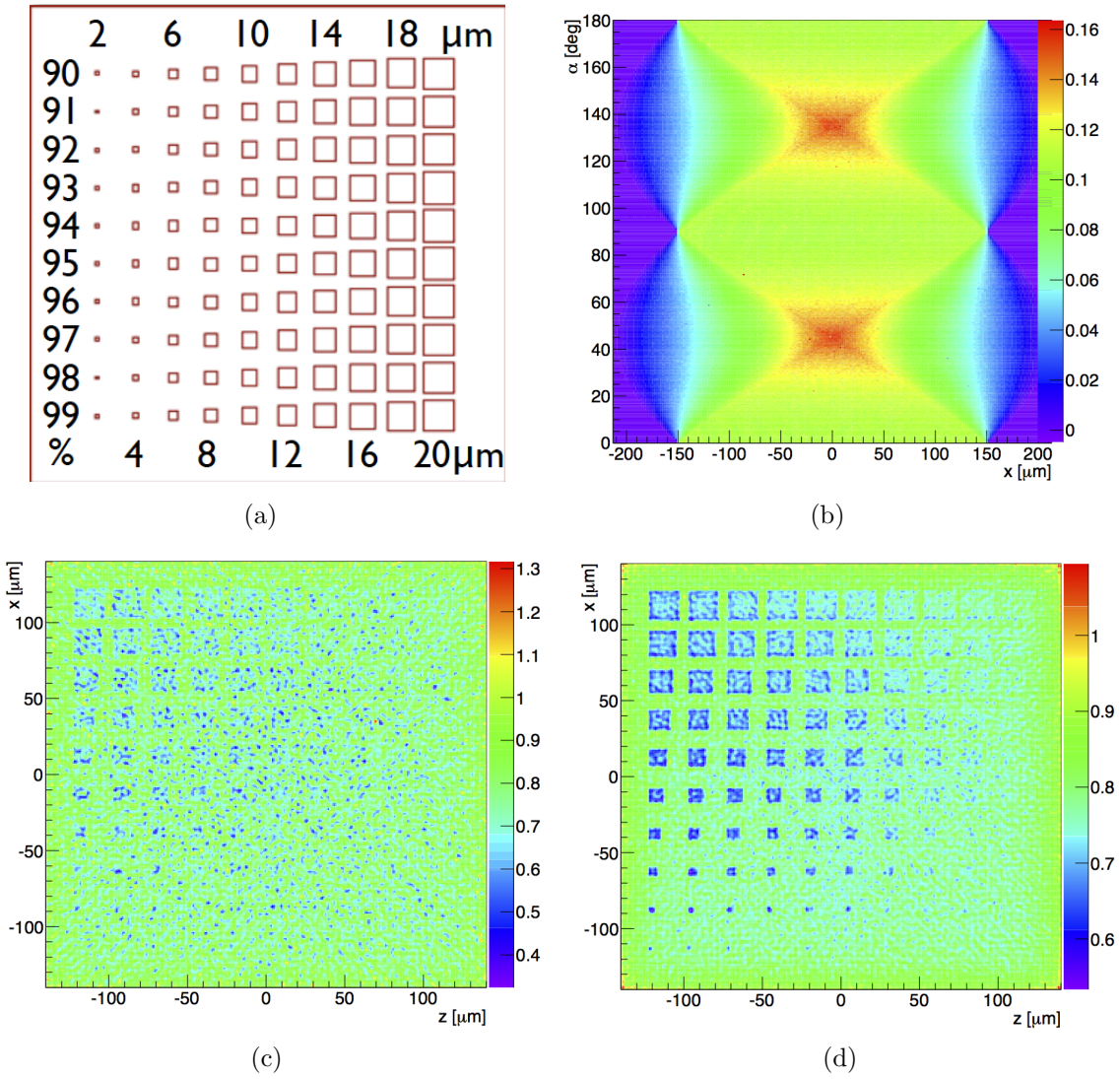

(a) (b)

(c) (d)

Figure 4.16.: (a) Sketch of the sample used for the simulation [50], (b) a sinogram obtained by simulating 100 events, (c) a back projected image of the sample using 1000 events and (d) a back projected image of the sample using 10000 events.

Fortuneteller, what do you see?
Future in a card
Share your secrets, tell them to me
Under a Violet Moon.
- Blackmore's Night

Chapter 5

Conclusions

During the Long Shutdown 1 of the LHC, the 3-Layer ATLAS Pixel Detector was refurbished and equipped with new Service Quarter Panels as well as a new Diamond Beam Monitor. Up to 92% of failing Pixel modules from Run 1 were recovered. The detector was re-installed into the ATLAS Experiment and re-integrated into its data acquisition. The LHC is about to restart operation and provide proton-proton collisions with single beam energies of up to 6.5 TeV in Run 2.

The IBL is the fourth layer of silicon pixel detectors in the ATLAS Experiment, foreseen to take data in Run 2 and Run 3 up to the high luminosity upgrade of the LHC. As a major part of this thesis, a quality assurance test bench was planned, commissioned and successfully operated, serving as the first major checkpoint for each newly built ATLAS IBL stave. A procedure ensuring electrical and logical functionality as well as calibration capability and particle detection in conditions expected inside the ATLAS Experiment was developed. The results obtained in that test bench serve as reference points for the on-going commissioning of the ATLAS IBL Detector and are essential for the understanding of up-coming physics results.

All components used for the ATLAS IBL were successfully built and found to meet the demanding requirements with respect to engineering constraints, operational stability, calibration performance and radiation hardness. Eventually the 14 best staves were chosen to build the ATLAS IBL. All modules were functional after integration and 99.9 % of the pixels were operational. The installation into the ATLAS Detector was successful and no damages were observed. Also the beam pipe bake out left the detector unharmed and first data using cosmic rays was taken in combination with other ATLAS sub-detectors.

The second part of the thesis was the investigation of a new sensor characterization method. During a dedicated testbeam data taking campaign in 2012 a 3D prototype sensor from the ATLAS IBL production was studied at various rotation angles to investigate its charge collection properties. A total of 140 runs at DUT rotation angles between -90 ° and 90 ° in varying step sizes were acquired. It was shown that the cluster properties follow the prediction after properly merging split clusters at high angles, which occur due to charge signals close to the threshold and charge sharing effects.

Furthermore, it was found that the estimated number of track segments was stable over the entire data taking period, which was one of the main goals for that testbeam campaign. However, due to a saturation of the Timepix timing plane, the total number of usable tracks was too low for in depth studies, especially at high incident angles. A possibility to improve the number of tracks holding valid FE-I4 data in future testbeam studies could be to define a region-of-interest trigger, which follows the FE-I4 acceptance window. In addition, not fully understood residual distributions were observed in the DUT alignment. In particular, proper alignment was only possible in one spatial coordinate. A number of potential effects could be ruled out while a few possibilities are still open, but none of them was found to be corrigible in software in the scope of this thesis. Thus, solely preliminary results on sub-pixel resolution studies were presented.

Despite being extraordinarily complex to accomplish, the 3-dimensional charge collection efficiency studies bear the possibility of becoming a future sensor characterization technique, complementing studies carried out in laboratories and two dimensional hit and charge collection efficiency evaluations from conventional testbeam measurements. The main achievements in the scope of this thesis are the proof of principles, that the approach of signal reconstruction using convolutions of the Landau distribution and a Gaussian function is feasible, as well as the method of using the detection capabilities of the device under test in order to obtain projections of the collected charges inside the device. Additional studies depending on threshold, ToT and sensor bias settings could reveal effects introduced as a consequence of production steps, which may not be covered in simulations. Statistics, computing and charge resolution requirements are still demanding. State-of-the-art beam telescopes provide either high trigger rates or high pointing resolutions. However, future developments in the rapidly evolving field of beam telescopes may reveal measurement capabilities providing both at the same time to acquire more suitable data for the above described studies.

List of Figures

List of References

[1] The Noble Prize Foundation. The Nobel Prize in Physics 2013, 2013. http://www.nobelprize.org/nobel_prizes/physics/laureates/2013/.

[2] ATLAS Collaboration. Observation of a New Particle in the Search for the Standard Model Higgs Boson with the ATLAS Detector at the LHC. *Physics Letters B, CERN-PH-EP-2012-218*, 2012.

[3] CMS Collaboration. Observation of a new boson at a mass of 125 GeV with the CMS experiment at the LHC. *Physics Letters B, CERN-PH-EP/2012-220*, 2013.

[4] CERN Technology Department. The CERN accelerator complex, 2015. http://te-dep-epc.web.cern.ch/te-dep-epc/machines/pagesources/Cern-Accelerator-Complex.jpg.

[5] L. Evans et al. LHC Machine. *JINST 3 S08001*, 2008.

[6] M. Bajko et al. Report of the Task Force on the Incident of 19 September 2008 at the LHC. *LHC-PROJECT-REPORT-1168*, 2009.

[7] CERN Technology Department. The LHC underground facilities, 2015. http://te-epc-lpc.web.cern.ch/te-epc-lpc/machines/lhc/pagesources/LHC-Underground-Layout.png.

[8] ATLAS Collaboration. The ATLAS Experiment at the CERN Large Hadron Collider. *JINST 3 S08003*, 2008.

[9] CMS Collaboration. The CMS Experiment at the CERN Large Hadron Collider. *JINST 3 S08004*, 2008.

[10] CMS Collaboration. CMS Detector Design, 2015. http://cms.web.cern.ch/news/cms-detector-design.

[11] ALICE Collaboration. The ALICE Experiment at the CERN Large Hadron Collider. *JINST 3 S08002*, 2008.

[12] LHCb Collaboration. The LHCb Detector at the LHC. *JINST 3 S08005*, 2008.

[13] R. Ostojić. Overview of LHC interaction region upgrade - Phase 1. *CERN-ATS-2010-026*, 2010.

[14] A. Abdesselam, P. Allport. The ATLAS Experiment - High Luminosity Upgrade, 2010. http://atlas.web.cern.ch/Atlas/GROUPS/UPGRADES/.

[15] W. R. Leo. *Techniques for Nuclear and Particle Physics Experiments*. Springer-Verlag, second revised edition, 1994.

[16] G. Lutz. *Semiconductor Radiaton Detectors*. Springer-Verlag, 2001.

[17] V. Cindro et al. The ATLAS Beam Conditions Monitor. *2008 JINST 3 P02004*, 2008.

[18] R. Wunstorf. *Systematische Untersuchungen zur Strahlenresistenz von Silizium-Detektoren fuer die Verwendung in Hochenergiephysik-Experimenten*. PhD thesis, U. Hamburg, DESY FH1K-92-01, 1992.

[19] G. Troska. *Development and operation of a testbeam setup for qualification studies of ATLAS Pixel Sensors*. PhD thesis, U. Dortmund, http://hdl.handle.net/2003/29351, 2012.

[20] H. Feick. Recent Results by the ROSE/CERN RD 48 Collaboration, 2000. `http://www.physics.purdue.edu/vertex/talks/feick.pdf`.

[21] D. Dobos. *Commissioning Perspectives for the ATLAS Pixel Detector*. PhD thesis, U. Dortmund, http://hdl.handle.net/2003/25125, 2007.

[22] G.Aad et al. ATLAS pixel detector electronics and sensors. *JINST 3, P07007*, 2008.

[23] I. Perić et al. The FEI3 readout chip for the ATLAS pixel detector. *Nucl.Instrum.Meth. A565 178-187*, 2006.

[24] J. Jentzsch. Operational Performance and Status of the ATLAS Pixel Detector at the LHC. *WSPC*, 2013.

[25] M. Backhaus. Development of an USB-based test system for the FE-I3 readout chips of the ATLAS pixel detector and Noise Occupancy Studies. Master's thesis, U. Bonn, BONN-IB-2009-14, 2009.

[26] ATLAS Collaboration. ATLAS Pixel Public Results, 2013. `https://twiki.cern.ch/twiki/bin/view/AtlasPublic/ApprovedPlotsPixel`, `https://twiki.cern.ch/twiki/bin/view/AtlasPublic/PixelPublicResults`.

[27] S. Welch, J. Dopke. The ATLAS Pixel nSQP Readout Chain. *ATL-INDET-PROC-2012-018*, 2012.

[28] K. Lantzsch. Status and performance of the ATLAS Pixel Detector at the LHC after three years of operation. *ATL-INDET-PROC-2014-001*, 2014.

[29] ATLAS Collaboration. ATLAS Public Results, 2014. `https://twiki.cern.ch/twiki/bin/view/AtlasPublic/ApprovedPlotsPixel`.

[30] I. Dolenc. ATLAS Diamond Beam Conditions Monitor. *PoS (VERTEX 2008) 012*, 2008.

[31] M. Červ. The ATLAS Diamond Beam Monitor. *JINST 9 C02026*, 2014.

[32] A.J. Edwards et al. Radiation monitoring with CVD diamonds in BaBar. *Nucl. Instrum. Meth. A 552 176.*, 2005.

[33] ATLAS IBL Collaboration. ATLAS Insertable B-Layer Technical Design Report, CERN-LHCC-2010-013, ATLAS-TDR-019, Addendum CERN-LHCC-2012-009, ATLAS-TDR-019-ADD-1. Technical report, CERN, 2010.

[34] ATLAS IBL Collaboration. Prototype ATLAS IBL modules using the FE-I4A front-end readout chip. *JINST 7 P11010*, 2012.

[35] M. Garcia-Sciveres et al. The FE-I4 pixel readout integrated circuit. *Nucl.Instrum.Meth. A636 S155-S159*, 2011.

[36] S. Altenheiner et al. Planar slim-edge pixel sensors for the ATLAS upgrades. *JINST 7 C02051*, 2012.

[37] D. Muenstermann C. Gossling, R. Klingenberg and T. Wittig. Evaluation of the breakdown behaviour of ATLAS silicon pixel sensors after partial guard-ring removal. *Nucl. Instrum. Meth. A 624 410*, 2010.

[38] J. Weingarten et al. Planar pixel sensors for the ATLAS upgrade: beam tests results. *JINST 7 P10028*, 2012.

[39] T. Wittig. *Slim edge studies, design and quality control of planar ATLAS IBL pixel sensors*. PhD thesis, TU Dortmund, http://hdl.handle.net/2003/30362, 2013.

[40] ATLAS Collaboration. ATLAS Pixel IBL: Stave Quality Assurance. *ATL-INDET-PUB-2014-006*, 2014.

[41] S. Kersten et al. Detector Control System of the ATLAS Insertable B-Layer. *HAL Id: in2p3-00636348*, 2011.

[42] J. Jentzsch on behalf of the ATLAS Collaboration. Performance tests during the ATLAS IBL Stave Integration. *JINST 10 C04036*, 2015.

[43] ATLAS Collaboration. ATLAS Public Results, 2014. `https://twiki.cern.ch/twiki/bin/view/AtlasPublic/`.

[44] L. Evans et al. The External Proton Beam Lines and the Splitter Systems of the CERN SPS. *IEEE Transactions on Nuclear Science*, NS-24(3), 1977.

[45] K.Akiba et al. Charged particle tracking with the Timepix ASIC. *Nucl. Instr. A 661*, pages 31–49, 2011.

[46] E. Gschwendtner. CNGS and North Area Operation. *Shutdown Lectures*, 2008.

[47] Z.Vykdyal et al. The RELAXd project: Development of four-side tilable photon-counting imagers. *Nucl. Instrum. Meth. A 591 241-244*, 2008.

[48] K.Akiba et al. The Timepix Telescope for High Performance Particle Tracking. *Nucl. Instrum. Meth. A 723 47-54*, 2013.

[49] M. Kennel. KDTREE 2: Fortran 95 and C++ Software to Efficiently Search for Near Neighbours in a Multi-Dimensional Euclidean Space. *http://arxiv.org/abs/physics/0408067v2*, 2004.

[50] T. Humair. Simulation tool for 3D charge collection efficiency tomography. *CERN-STUDENTS-Note-2013-225*, 2013.

Appendix A

Auxiliary Stave QA Table and Commissioning Plots

Position	Stave	Number of bad pixels	Score	Planarity [μm]	Reworked
#01	ST17	1052	1.01	114	no
#02	ST02	579	0.44	205	yes
#03	ST19	971	1.13	266	no
#04	ST09	1110	1.00	229	yes
#05	ST18	1266	0.94	336	no
#06	ST04	799	0.69	235	yes
#07	ST13	718	0.56	224	no
#08	ST10	646	0.62	243	yes
#09	ST11	565	0.58	298	no
#10	ST12	542	0.62	314	yes
#11	ST16	879	0.82	329	no
#12	ST06	734	0.79	290	yes
#13	ST15	864	0.84	325	no
#14	ST05	601	0.68	189	yes
n/a	ST01	1011	1.04	224	yes
n/a	ST03	1235	2.48	223	yes
n/a	ST14	1877	1.11	218	no
n/a	ST20	2139	2.01	237	no

Table A.1.: Ranking and loading order overview of the 14 IBL staves. The cooling pipe of the stave in position 01 is at $\phi = -6.1°$, subsequent staves are displaced by 25.7° in ϕ. The score is determined by the number of bad pixels, each of which is weighted according to the position on a stave. A lower score thus translates into a higher quality stave. The planarity shows the difference between the minimum and maximum height of a stave. The last column indicates whether a stave has been reworked at the CERN DSF bond lab. For completeness, the bottom four lines show numbers for the staves that were not chosen for installation. For the stave loading around the beam pipe, not only this score but a uniform $\eta - \phi$ bad pixel distribution and engineering constraints are also taken into account [40].

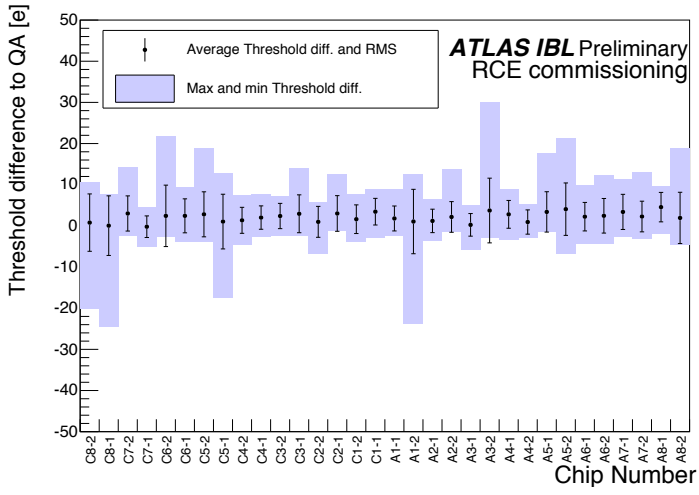

(a)

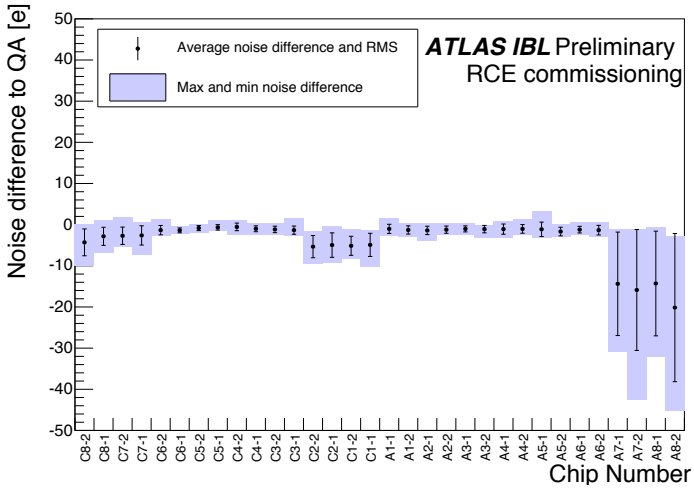

(b)

Figure A.1.: (a) Threshold and (b) threshold noise chip-to-chip difference of the values obtained in the RCE measurements and the QA among the 14 ATLAS IBL production staves after retuning all pixels to a target threshold of 3 000 e^- and to a 10 ToT target response for 16 000 e^-. The individual pixel data have first been averaged over each chip. The plots show, for each chip position on the stave, the mean and scatter of the 14 data points (one from each stave). The error bars show the RMS spread, while the solid boxes show the minimum and maximum values. The higher noise on the A-side in the QA measurements was caused by a small noise on the HV line of the setup and the sensitivity of FBK modules, which were more frequently chosen for loading on A-side, to such noise. The noise on the outer 3D modules is generally higher than on the planar modules [29].

Appendix B

Auxiliary Testbeam Table and Plots

Run	Angle [°]	Tracks			
		total	in time overlap	timestamped	with FEI4 data
5252	0	390062	201680 (52%)	168023 (43%)	146979 (38%)
5253	1	326994	157250 (48%)	121592 (37%)	106048 (32%)
5254	2	318323	153923 (48%)	124807 (39%)	111220 (35%)
5255	3	323276	152381 (47%)	116133 (36%)	104062 (32%)
5256	4	251682	116949 (46%)	97335 (39%)	86926 (35%)
5257	5	258633	142862 (55%)	118585 (46%)	104637 (40%)
5258	6	291383	163488 (56%)	131214 (45%)	115958 (40%)
5259	7	224239	118012 (53%)	96797 (43%)	85770 (38%)
5260	8	253910	139025 (55%)	114034 (45%)	99807 (39%)
5261	9	264347	164548 (62%)	124605 (47%)	104500 (40%)
5262	10	268423	184316 (69%)	139132 (52%)	114147 (43%)
5266	12	192843	126342 (66%)	86356 (45%)	72598 (38%)
5268	13	247206	159878 (65%)	131485 (53%)	114901 (46%)
5269	14	205506	127004 (62%)	105231 (51%)	92574 (45%)
5270	15	184802	103966 (56%)	86276 (47%)	74470 (40%)
5271	16	213983	127933 (60%)	105375 (49%)	91975 (43%)
5272	17	184514	113763 (62%)	93336 (51%)	78451 (43%)
5273	18	150616	91907 (61%)	75382 (50%)	63993 (42%)
5274	19	151498	92662 (61%)	75957 (50%)	65354 (43%)
5275	20	153842	86281 (56%)	71291 (46%)	62361 (41%)
5276	21	148987	90938 (61%)	74624 (50%)	64130 (43%)
5277	22	149527	92588 (62%)	75563 (51%)	62044 (41%)
5278	23	151682	95436 (63%)	77794 (51%)	65131 (43%)
5279	24	151096	85017 (56%)	70348 (47%)	60512 (40%)
5280	25	150395	83096 (55%)	69211 (46%)	60643 (40%)
5281	26	183194	102870 (56%)	85129 (46%)	72521 (40%)
5282	27	110717	62982 (57%)	52251 (47%)	28938 (26%)
5283	28	105612	58996 (56%)	48875 (46%)	42222 (40%)
5284	29	103253	59215 (57%)	48765 (47%)	42069 (41%)
5285	30	113685	63297 (56%)	52116 (46%)	44672 (39%)
5286	31	111817	65656 (59%)	53999 (48%)	43036 (38%)
5287	32	112758	65070 (58%)	53769 (48%)	44049 (39%)
5288	33	113463	64178 (57%)	52921 (47%)	44098 (39%)
5290	34	109759	59571 (54%)	49417 (45%)	38556 (35%)
5291	35	110998	60182 (54%)	49720 (45%)	38885 (35%)
5292	36	148502	84375 (57%)	69454 (47%)	47375 (32%)
5293	37	139918	78963 (56%)	65207 (47%)	46887 (34%)
5294	38	138199	80569 (58%)	66242 (48%)	45111 (33%)
5295	39	147588	90323 (61%)	73907 (50%)	45595 (31%)
5296	40	149569	94546 (63%)	76960 (51%)	47901 (32%)

Continued on next page

Run	Angle [°]	Tracks			
		total	in time overlap	timestamped	with FEI4 data
5297	41	149272	89091 (60%)	72930 (49%)	52167 (35%)
5298	42	104926	60320 (57%)	49756 (47%)	35391 (34%)
5299	43	112698	65274 (58%)	53556 (48%)	38623 (34%)
5300	44	112297	63403 (56%)	52313 (47%)	35698 (32%)
5301	45	112491	63275 (56%)	52187 (46%)	33868 (30%)
5302	46	107244	62236 (58%)	51120 (48%)	35688 (33%)
5303	47	112691	66141 (59%)	54390 (48%)	32028 (28%)
5304	48	108001	65915 (61%)	53550 (50%)	27765 (26%)
5305	49	104438	61599 (59%)	50347 (48%)	25160 (24%)
5306	50	110529	64113 (58%)	52685 (48%)	27406 (25%)
5307	51	114177	65200 (57%)	53419 (47%)	29105 (25%)
5308	52	94242	52295 (55%)	43095 (46%)	23673 (25%)
5309	53	113043	64879 (57%)	44090 (39%)	21073 (19%)
5310	54	109959	56805 (52%)	47110 (43%)	26300 (24%)
5311	55	110948	65577 (59%)	53984 (49%)	23870 (22%)
5312	56	74588	42052 (56%)	34519 (46%)	17812 (24%)
5313	57	104467	62165 (60%)	51245 (49%)	20297 (19%)
5314	58	107169	61523 (57%)	50517 (47%)	20930 (20%)
5315	59	109584	62908 (57%)	51456 (47%)	20450 (19%)
5316	60	113857	68522 (60%)	56078 (49%)	16675 (15%)
5317	61	109447	64453 (59%)	52989 (48%)	16409 (15%)
5318	62	108531	66391 (61%)	54098 (50%)	15743 (15%)
5319	63	113286	65510 (58%)	53811 (48%)	18003 (16%)
5320	64	113024	64638 (57%)	53226 (47%)	14813 (13%)
5321	65	75439	42609 (56%)	35114 (47%)	10425 (14%)
5322	66	71948	41526 (58%)	34176 (48%)	9198 (13%)
5323	67	111542	62828 (56%)	51883 (47%)	13551 (12%)
5324	68	74166	41018 (55%)	33954 (46%)	8911 (12%)
5325	69	73486	38930 (53%)	32314 (44%)	7626 (10%)
5326	70	113080	64589 (57%)	53180 (47%)	9957 (8.8%)
5327	71	111632	62893 (56%)	41270 (37%)	7465 (6.7%)
5328	72	111836	62807 (56%)	52188 (47%)	8219 (7.3%)
5329	73	112320	61687 (55%)	50974 (45%)	7184 (6.4%)
5330	74	110961	62122 (56%)	51332 (46%)	7992 (7.2%)
5331	75	112930	64996 (58%)	53281 (47%)	5293 (4.7%)
5332	76	102876	58389 (57%)	48211 (47%)	4991 (4.9%)
5333	77	109303	60319 (55%)	49937 (46%)	5460 (5.0%)
5334	78	109444	58472 (53%)	48306 (44%)	3625 (3.3%)
5335	79	108924	59169 (54%)	49116 (45%)	3313 (3.0%)
5336	80	294653	165440 (56%)	136344 (46%)	3508 (1.2%)

Continued on next page

Run	Angle [°]	Tracks			
		total	in time overlap	timestamped	with FEI4 data
5337	82	140181	78643 (56%)	64628 (46%)	2055 (1.5%)
5338	83	221725	133640 (60%)	109708 (49%)	1892 (0.9%)
5339	84	217613	123318 (57%)	92124 (42%)	1270 (0.6%)
5340	85	254670	140715 (55%)	115657 (45%)	1050 (0.4%)
5341	86	274796	154408 (56%)	127093 (46%)	609 (0.2%)
5342	87	321116	186907 (58%)	153149 (48%)	384 (0.1%)
5343	88	456512	263088 (58%)	215579 (47%)	300 (0.1%)
5344	89	566254	334805 (59%)	273437 (48%)	349 (0.1%)
5345	90	461872	263721 (57%)	214169 (46%)	376 (0.1%)
5346	-89	521584	295777 (57%)	243954 (47%)	1808 (0.3%)
5347	-87	443406	244930 (55%)	202730 (46%)	4109 (0.9%)
5348	-85	188459	104267 (55%)	86395 (46%)	3208 (1.7%)
5349	-83	220274	126889 (58%)	105021 (48%)	5772 (2.6%)
5350	-81	172258	94431 (55%)	78781 (46%)	5993 (3.5%)
5351	-79	183343	103361 (56%)	85621 (47%)	6561 (3.6%)
5352	-77	188150	107254 (57%)	89229 (47%)	8357 (4.4%)
5353	-75	146710	82262 (56%)	68089 (46%)	8419 (5.7%)
5354	-73	110995	60003 (54%)	50045 (45%)	7883 (7.1%)
5355	-71	105771	55887 (53%)	30455 (29%)	6188 (5.9%)
5356	-69	112656	60627 (54%)	50500 (45%)	11311 (10%)
5357	-67	111181	61237 (55%)	51059 (46%)	12379 (11%)
5358	-65	111678	63175 (57%)	52394 (47%)	14256 (13%)
5359	-63	111813	64476 (58%)	53619 (48%)	17126 (15%)
5360	-61	104839	58037 (55%)	48221 (46%)	19182 (18%)
5361	-59	71845	38409 (53%)	31838 (44%)	14502 (20%)
5362	-57	100921	57384 (57%)	47448 (47%)	18749 (19%)
5363	-57	89401	50468 (56%)	41611 (47%)	18503 (21%)
5365	-55	110451	60107 (54%)	49774 (45%)	26396 (24%)
5366	-53	74797	41840 (56%)	34828 (47%)	21198 (28%)
5367	-51	110363	61578 (56%)	51142 (46%)	33206 (30%)
5368	-49	113186	60266 (53%)	50358 (44%)	35006 (31%)
5369	-47	108383	57492 (53%)	48050 (44%)	34144 (32%)
5370	-45	75138	41652 (55%)	34690 (46%)	26173 (35%)
5371	-43	107159	60520 (56%)	50266 (47%)	35598 (33%)
5372	-41	110003	60935 (55%)	50500 (46%)	38302 (35%)
5373	-39	109344	59113 (54%)	48989 (45%)	38652 (35%)
5374	-37	110550	60985 (55%)	50517 (46%)	40700 (37%)
5375	-35	110935	61013 (55%)	50648 (46%)	41184 (37%)
5376	-33	136009	76964 (57%)	63851 (47%)	53972 (40%)
5377	-31	110789	59393 (54%)	49502 (45%)	42636 (38%)

Continued on next page

Run	Angle [°]	Tracks			
		total	in time overlap	timestamped	with FEI4 data
5378	-29	140970	81950 (58%)	67535 (48%)	57621 (41%)
5379	-27	148813	86445 (58%)	71419 (48%)	60434 (41%)
5380	-25	184582	102121 (55%)	84813 (46%)	73523 (40%)
5381	-23	151774	86548 (57%)	71671 (47%)	62626 (41%)
5382	-21	180409	99263 (55%)	82045 (45%)	71317 (40%)
5383	-19	148982	88578 (59%)	72654 (49%)	63706 (43%)
5384	-17	152640	91641 (60%)	75305 (49%)	66101 (43%)
5385	-15	226208	129066 (57%)	106555 (47%)	92034 (41%)
5386	-13	186419	110859 (59%)	91171 (49%)	77940 (42%)
5387	-11	223751	125626 (56%)	103707 (46%)	91213 (41%)
5388	-9	260903	150683 (58%)	123714 (47%)	107021 (41%)
5389	-7	263379	146746 (56%)	121578 (46%)	106684 (41%)
5390	-5	291921	159832 (55%)	132467 (45%)	115406 (40%)
5391	-3	325341	174613 (54%)	144779 (45%)	126933 (39%)
5392	-1	363855	194014 (53%)	161453 (44%)	140764 (39%)

Table B.1.: Overview of all valid runs taken with the Timepix telescope and SCC99 as DUT. All fractions refer to the total number of tracks.

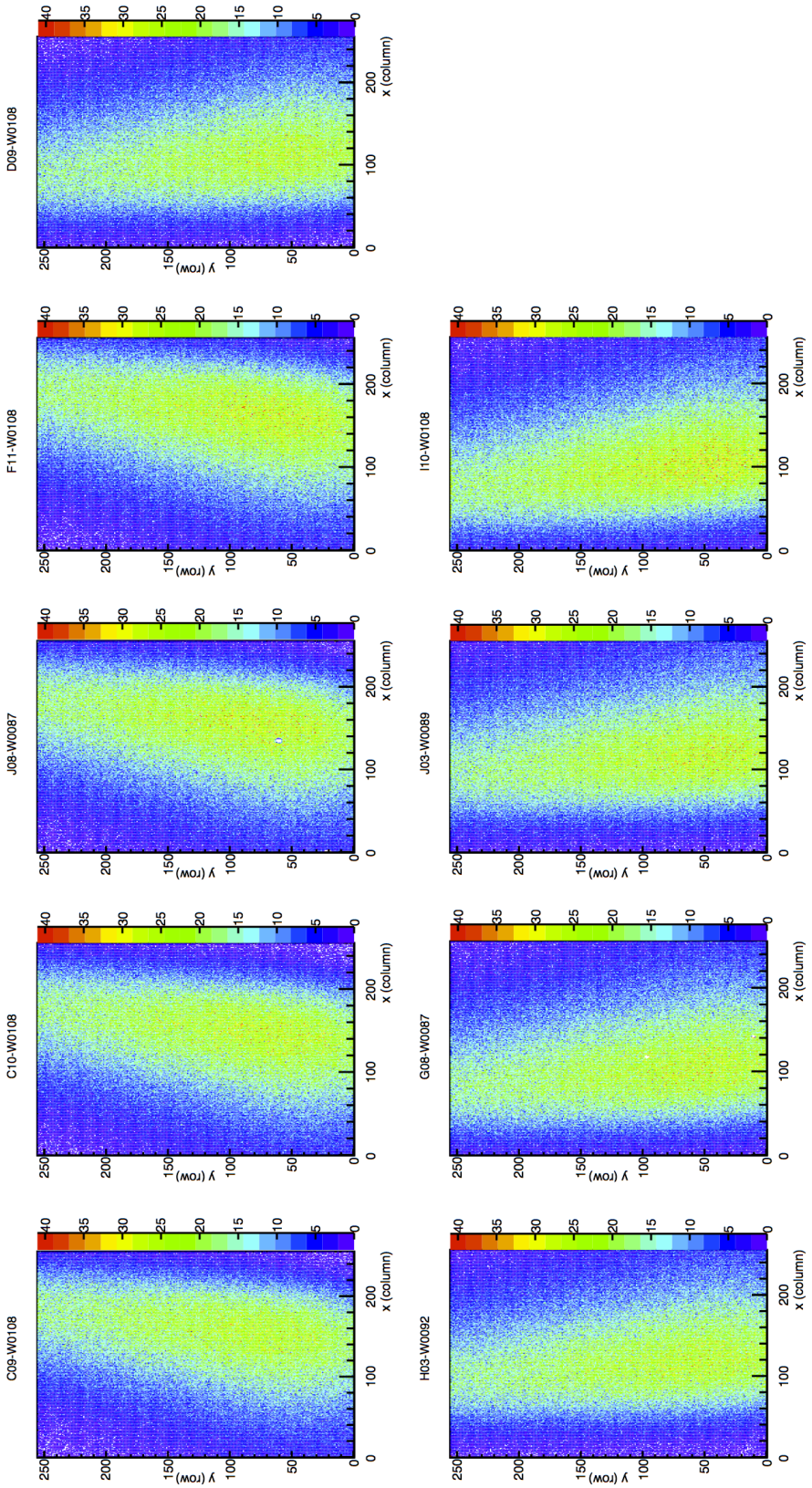

Figure B.1.: Timepix telescope local cluster positions using the example of Run 5252. It can be seen that the planes in the first arm are tilted in the opposite direction compared to the second arm.

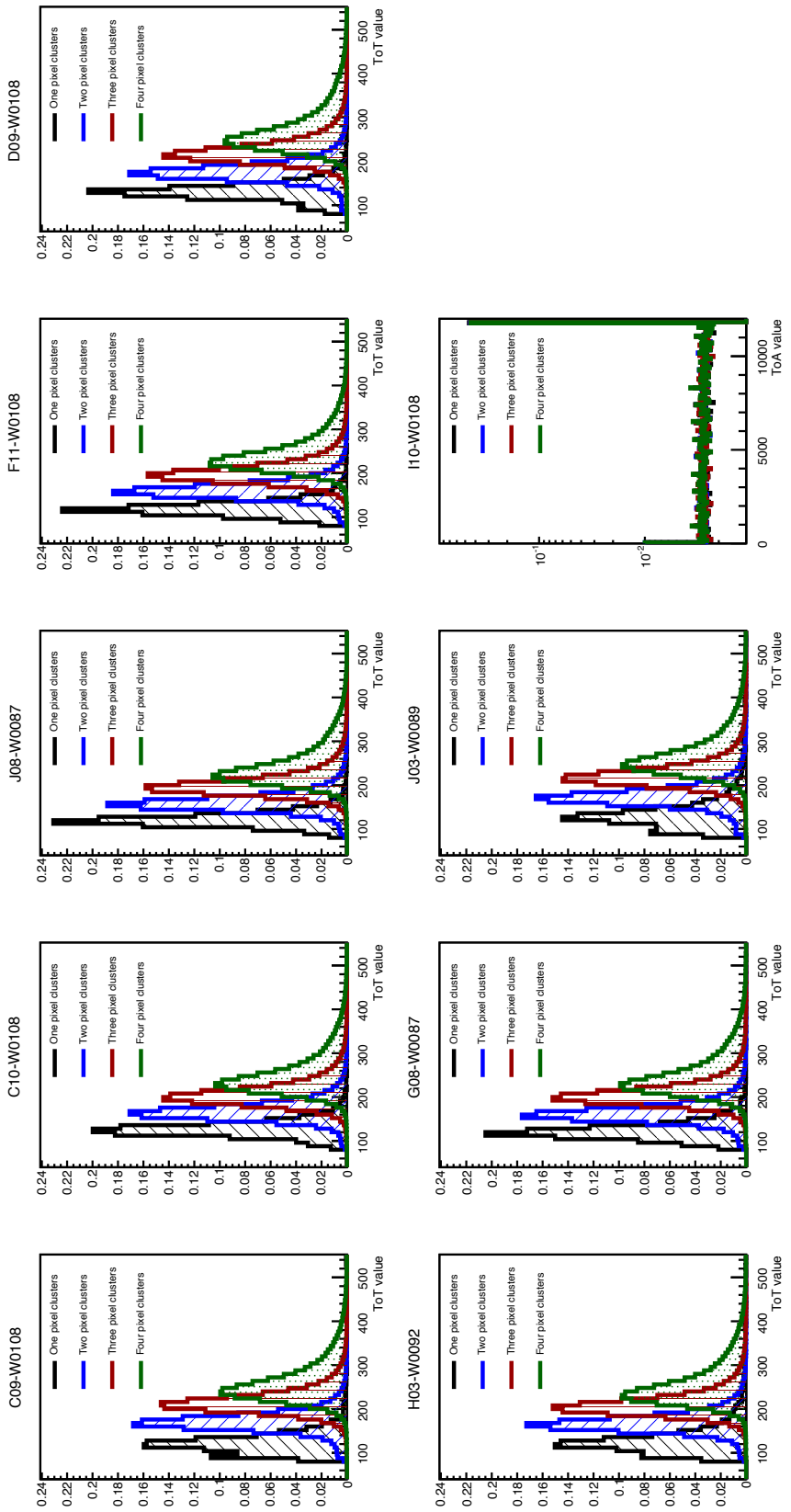

Figure B.2.: Timepix telescope ToT spectra (in ADC counts) for one, two, three and four pixel clusters using the example of Run 5252. The saturation of the ToA plane (I10-W0108) for about 50 % can clearly be seen.

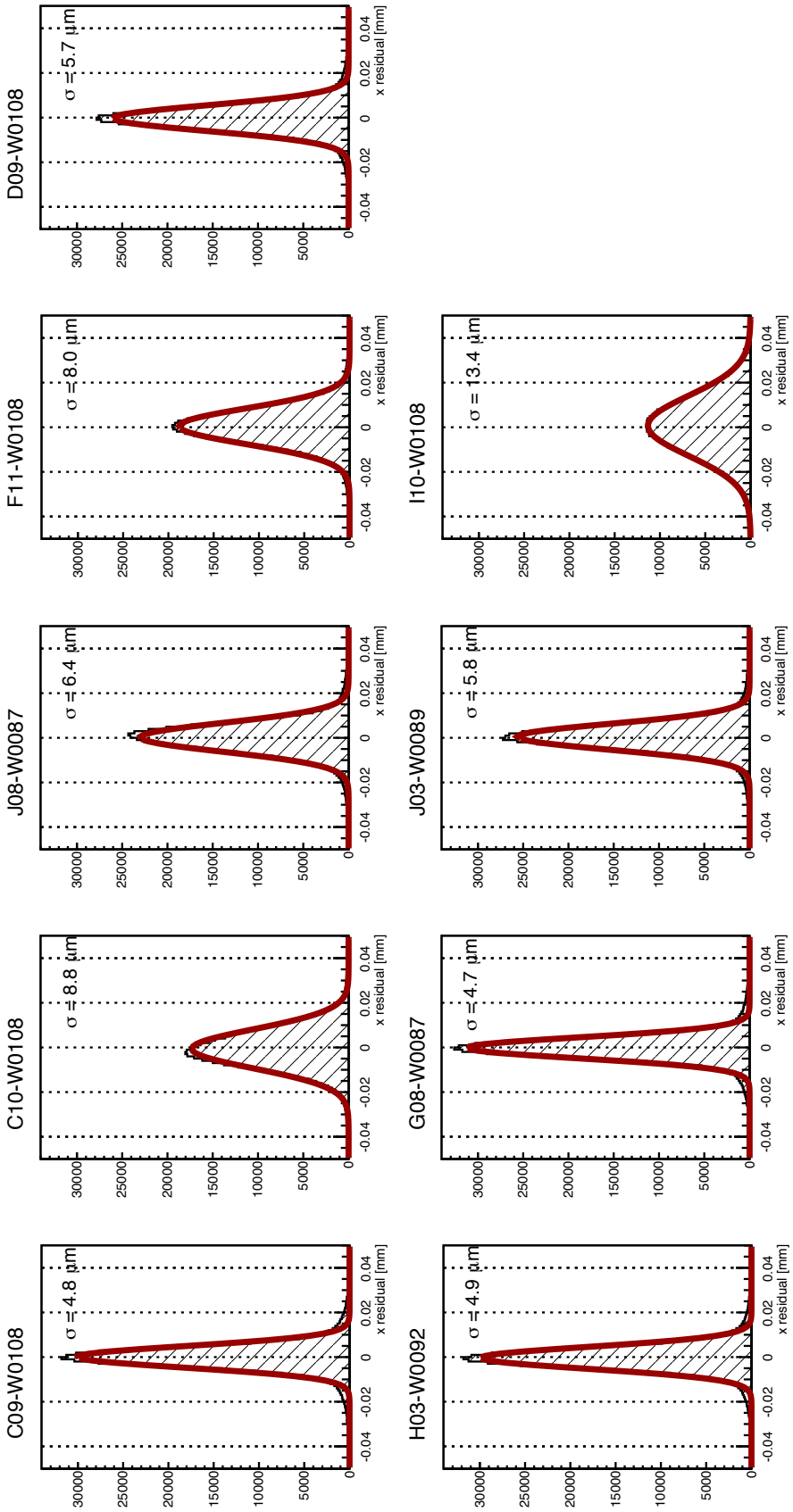

Figure B.3.: Timepix telescope biased residuals in x using the example of Run 5252.

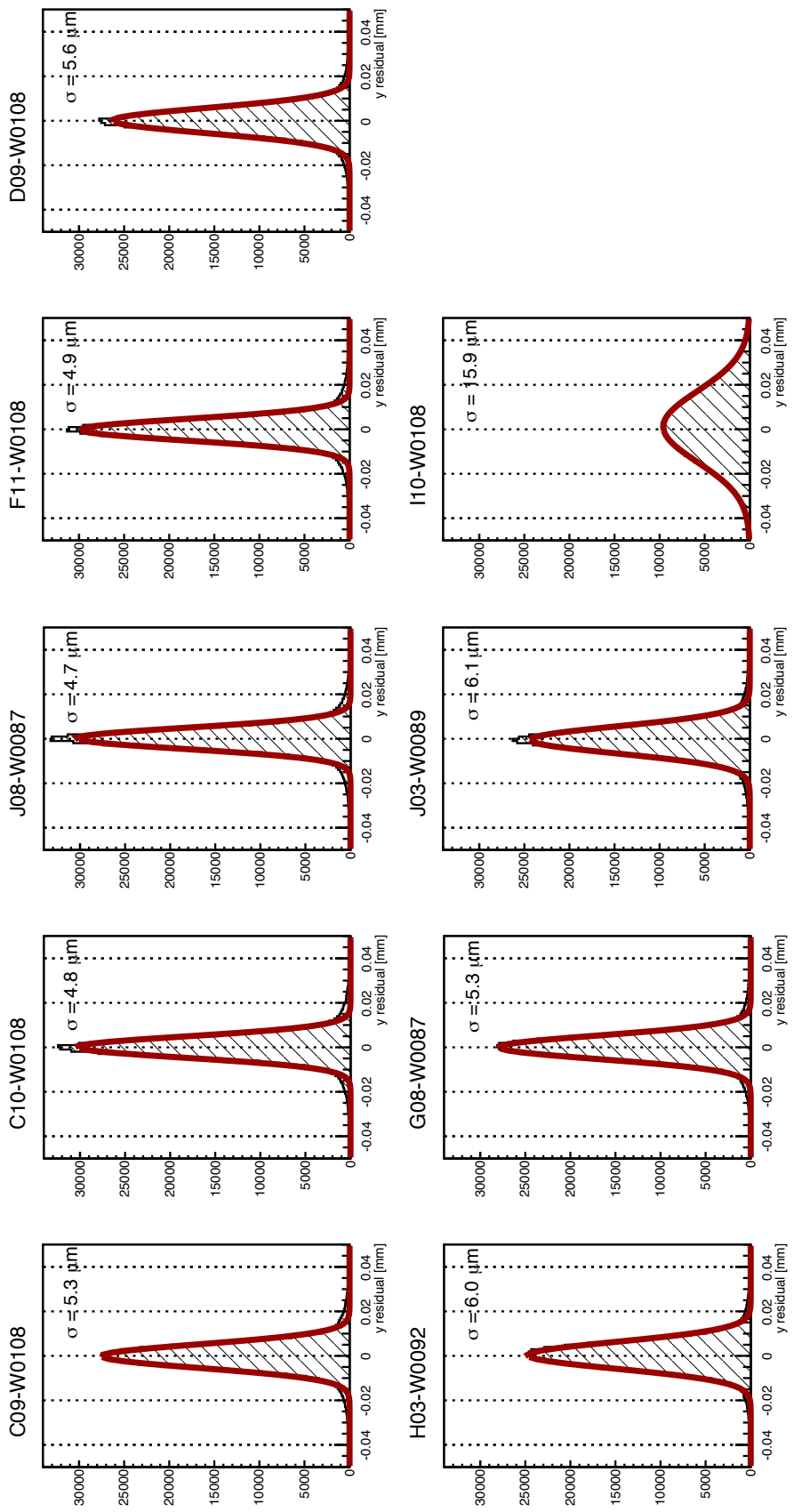

Figure B.4.: Timepix telescope biased residuals in y using the example of Run 5252.

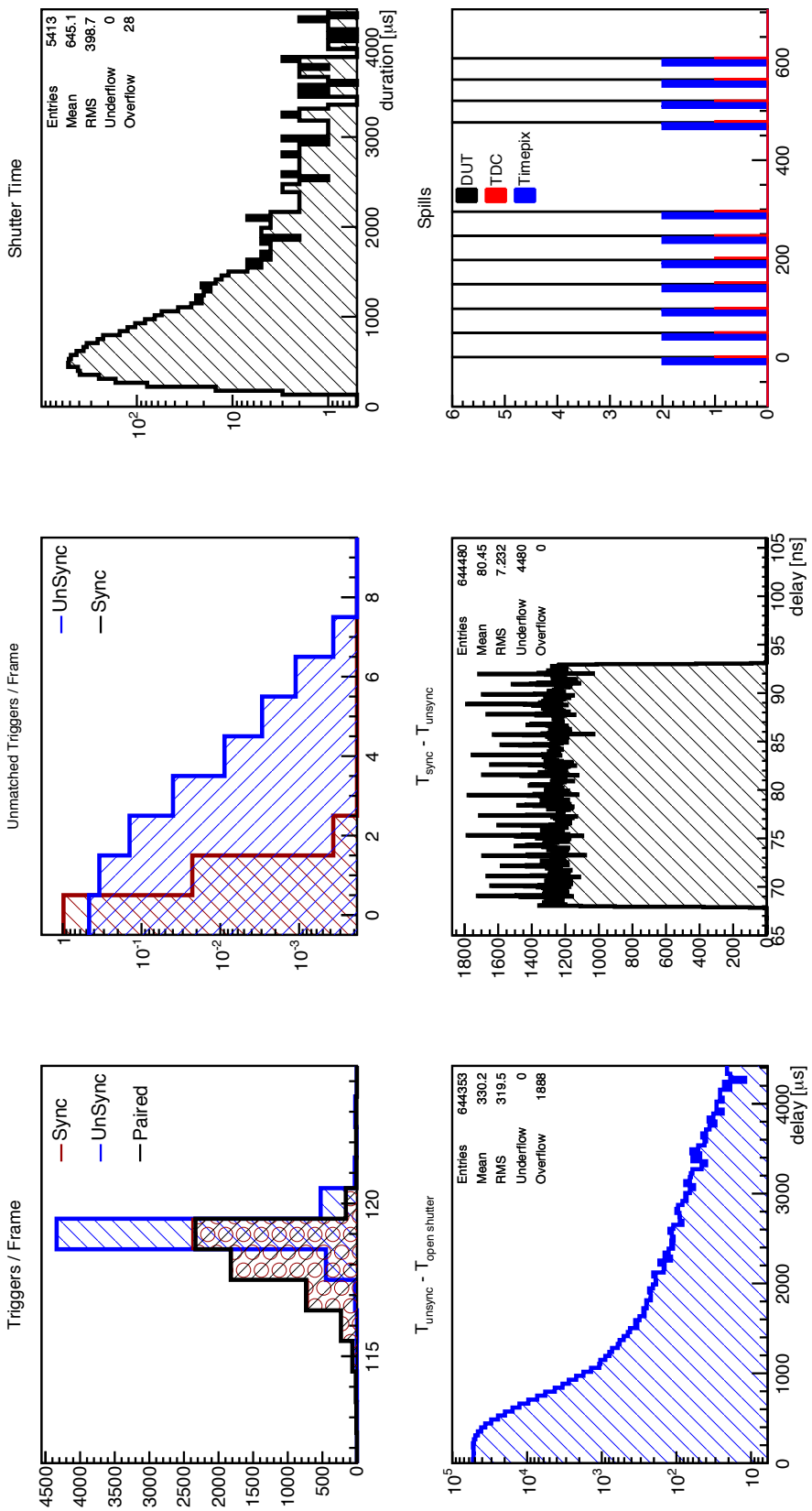

Figure B.5.: Timepix telescope amalgamation plots using the example of Run 5252.

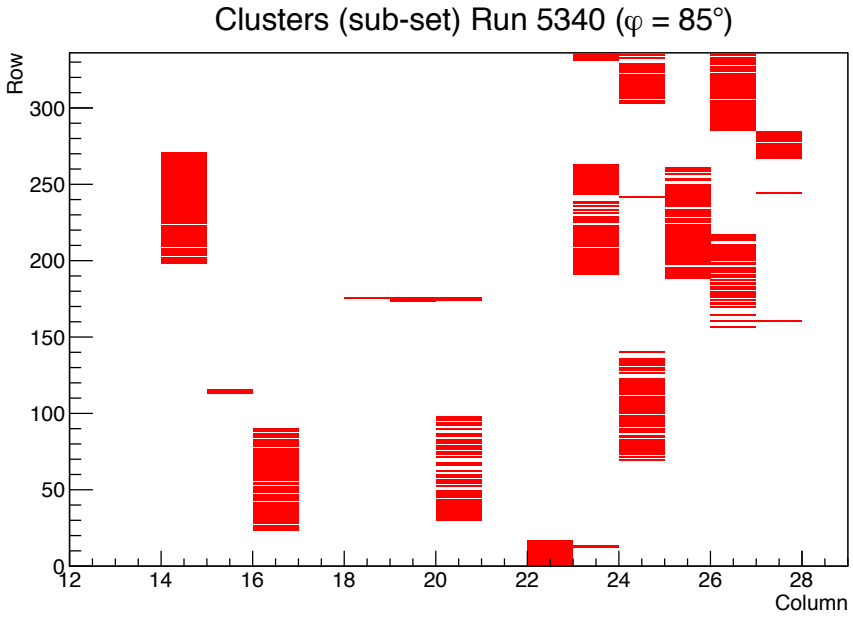

Figure B.6.: Example DUT hit map showing long split clusters within a sub-set of events taken from Run 5340 which corresponds to an angle of 85 °. The beam passes along the row direction.

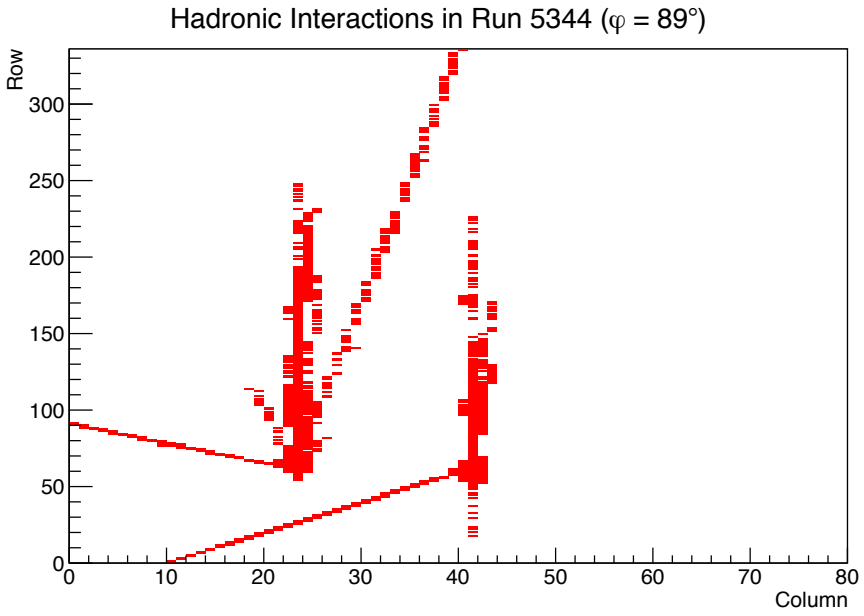

Figure B.7.: Example DUT hit map showing hadronic interactions within two independent events taken from Run 5344 which corresponds to an angle of 89 °. The primary beam passes along the row direction.

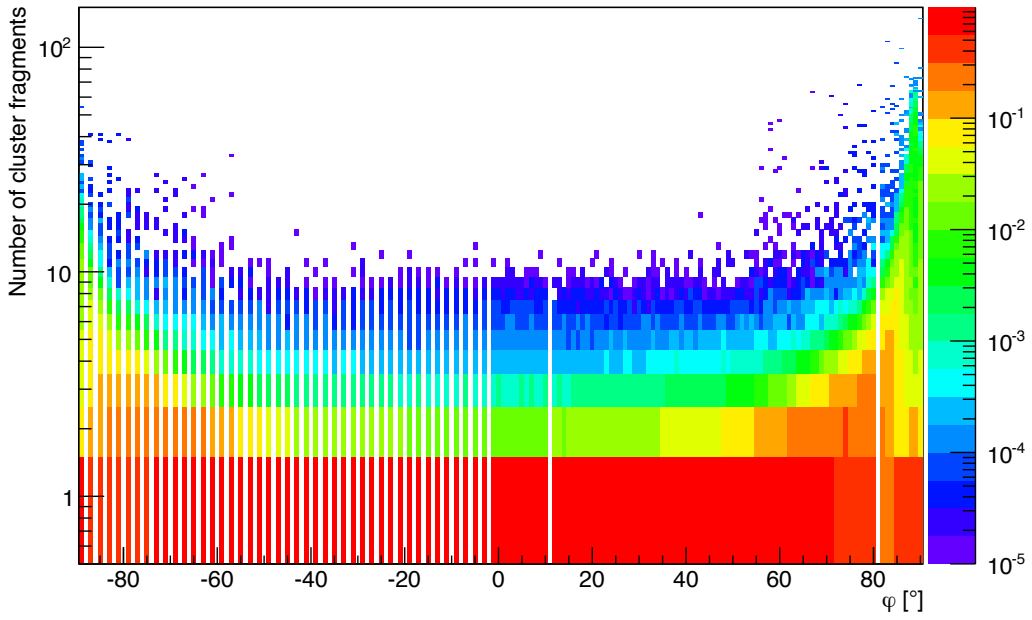

Figure B.8.: Number of DUT cluster fragments per angle.

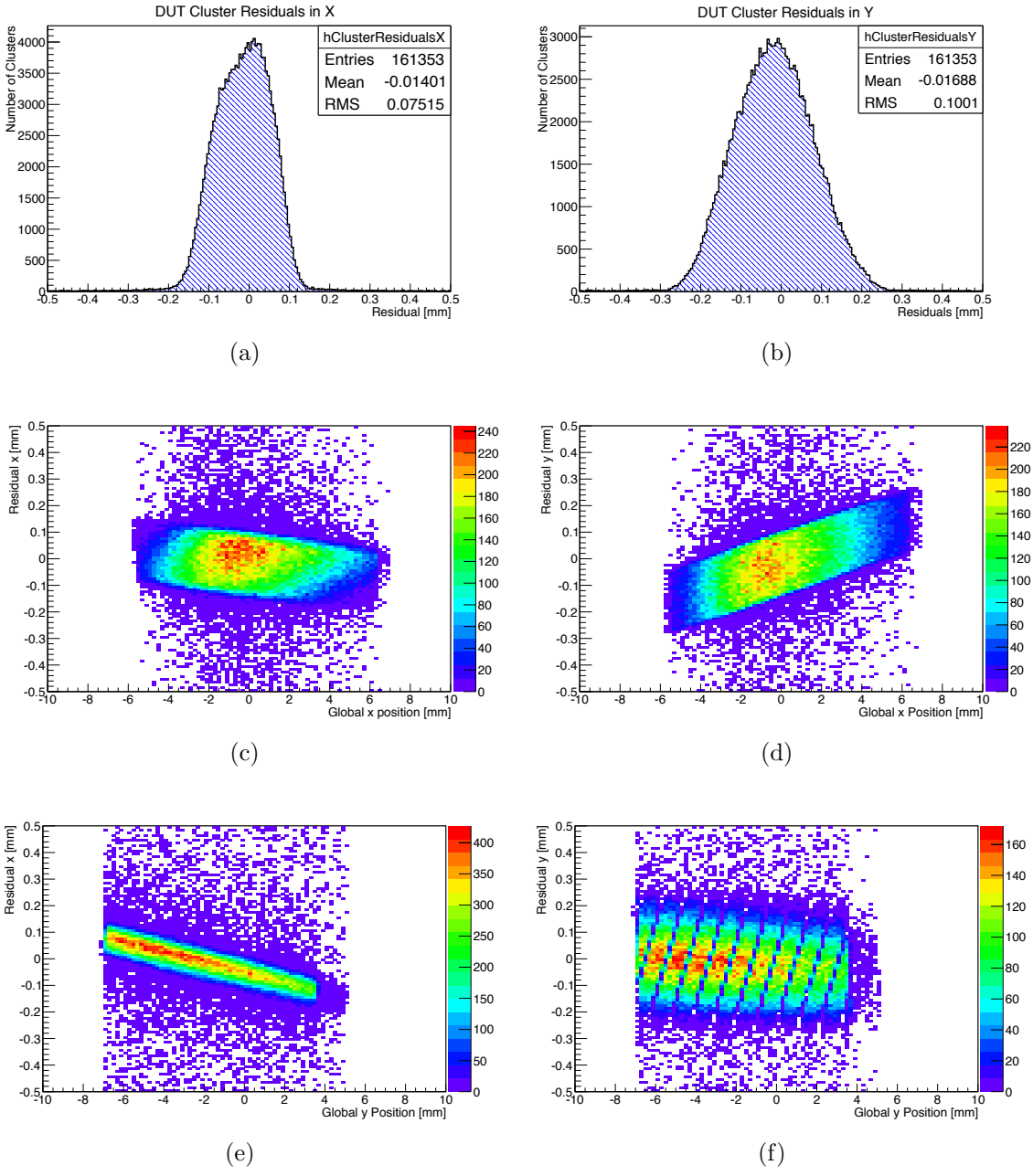

Figure B.9.: SCC99 (a) x and (b) y residual distributions and the corresponding correlations with global track coordinates in Run 5252, perpendicular incident. For comparison the DUT was tilted by $+1\,^{\circ}$ around the global z axis with respect to the original alignment.

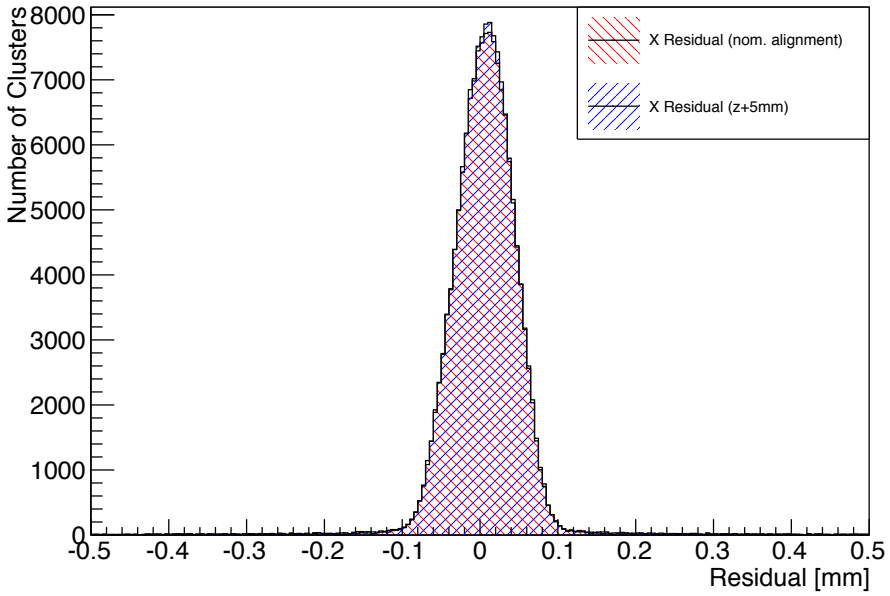

(a)

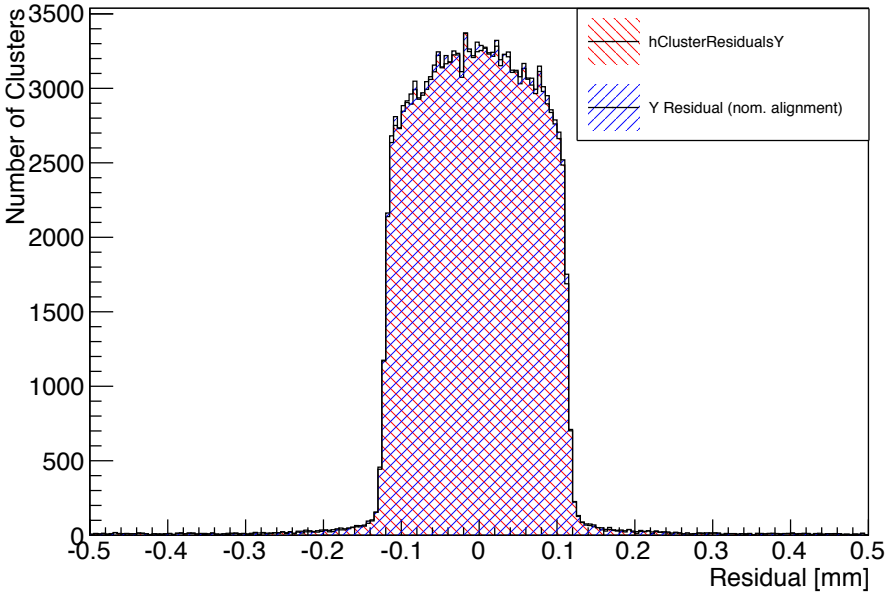

(b)

Figure B.10.: SCC99 (a) x and (b) y residual distributions in Run 5252, perpendicular incident. For comparison the DUT was shifted by +5 mm along the global z axis. Both residual distribution, with and without shift, are shown.

Appendix C

List of Acronyms

AC Alternating Current ... 39
AIDA Advanced European Infrastructures for Detectors at Accelerators ... 63
ALICE A Large Ion Collider Experiment ... 6
ASIC Application Specific Interated Circuit ... 63
ATCA Advanced Telecommunications Computing Architecture ... 46
ATLAS A Toroidal LHC ApparatuS ... 1
BCM Beam Conditions Monitor ... 17
CERN Conseil Européen pour la Recherche Nucléaire ... 1
CFD Computational Fluid Dynamics ... 56
CIM Cluster Interconnect Module ... 46
CiS Competence in Silicon, Forschungsinstitut für Mikrosensorik und Photovoltaik GmbH (Erfurt, Germany) ... 22
CMS Compact Muon Solenoid ... 1
CNM Centro Nacional de Microelectronica (Barcelona, Spain) ... 37
COMPASS COmmon Muon Proton Apparatus for Structure and Spectroscopy ... 61
CVD Chemical Vapor Deposition ... 17
DAC Digital to Analog Converter ... 24
DAQ Data Acquisition ... 42
DBM Diamond Beam Monitor ... 17
DCS Detector Control System ... 42
DRIE Deep Reactive Ion Etching ... 36
DUT Device Under Test ... 61
EEPROM Electrically Erasable Programmable Read-Only Memory ... 45
EoS End of Stave ... 44
FBK Fondazione Bruno Kessler (Trento, Italy) ... 37
FE FrontEnd Electronic ... 23
FE-I3 FrontEnd chip - Version 3 ... 21
FE-I4 FrontEnd chip - Version 4 ... 29
FDAC Feedback-current Digital to Analog Converter ... 24
FIFO First In First Out ... 39
FPGA Field Programmable Gate Array ... 45
FZ FloatZone ... 18
GEM Gas Electron Multiplier ... 11
HSIO High-Speed Input-Output ... 46
HV High Voltage, here: sensor bias ... 16
IBL Insertable B-Layer ... 31
IMC Interlock Matrix Crate ... 45
INFN Instituto Nazionale di Fisica Nucleare ... 48
IPT IBL Positioning Tube ... 55
ISEG iseg Spezialelektronik GmbH, Germany ... 44
IST IBL Support Tube
IZM Fraunhofer-Institut für Zuverlässigkeit und Mikrointegration (Berlin, Germany) ... 40
LDO Low Drop-Out regulators ... 38

LEP **L**arge **E**lectron-**P**ositron Collider . . . 4
LHC **L**arge **H**adron **C**ollider . . . 1
LHCb **LHC**-**b**eauty . . . 6
LSB **L**east **S**ignificant **B**it . . . 70
LV **L**ow **V**oltage, here: readout chip bias . . . 29
LVDS **L**ow **V**oltage **D**ifferential **S**ignal . . . 41
MIP **M**inimum **I**onising **P**article . . . 15
MPV **M**ost **P**robable **V**alue . . . 79
NEG **N**on **E**vaporable **G**etter . . . 56
NIEL **N**on **I**onising **E**nergy **L**oss . . . 18
NIM **N**uclear **I**nstrumentation **M**odule . . . 44
nSQP **n**ew **S**ervice **Q**uarter **P**anel
ON **ON** Semiconductor Czech Republic a.s., Roznov, Czech Republic . . . 22
PCB **P**rinted **C**ircuit **B**oard . . . 40
pCVD **p**olycrystalline **C**hemical **V**apor **D**eposition . . . 31
PKA **P**rimary **K**nock-on **A**tom . . . 18
PP2 **P**atch **P**anel **2** . . . 44
PS **P**roton **S**ynchrotron . . . 61
QA **Q**uality **A**ssurance . . . 34
RCE **R**econfigurable **C**luster **E**lement . . . 46
RELAXd high **RE**solution **L**arge **A**rea **X**-ray **d**etector . . . 63
RICH **R**ing **I**maging **CH**erenkov . . . 11
RMS **R**oot **M**ean **S**quare . . . 5
ROOT C++ based data analysis framework developed at CERN . . . 46
SCC **S**ingle **C**hip **C**ard . . . 74
SCT **S**emi**c**onductor **T**racker . . . 7
SEU **S**ingle **E**vent **U**psets . . . 39
SLAC SLAC National Accelerator Laboratory, originally **S**tanford **L**inear **A**ccelerator **C**enter . . . 46
SMD **S**urface **M**ounted **D**evice . . . 40
SPS **S**uper **P**roton **S**ynchrotron . . . 61
SQP **S**ervice **Q**uarter **P**anel . . . 29
TDAC **T**hreshold **D**igital to **A**nalog **C**onverter . . . 24
TDC **T**ime to **D**igital **C**onverter . . . 64
ToT **T**ime **o**ver **T**hreshold . . . 24
ToA **T**ime **o**f **A**rrival . . . 63
TRACI **T**ransportable **R**efrigeration **A**pparatus for CO_2 **I**nvestigation . . . 44
TRT **T**ransition **R**adiation **T**racker . . . 7
UBM **U**nder **B**ump **M**etallization . . . 35
VCAL **CAL**ibrated **V**oltage input line . . . 48
VELO **VE**rtex **LO**cator . . . 62
WIENER **W**orldwide-**I**ndustrial **E**lectronics-**N**uclear **E**lectronics-**R**esources, W-IE-NE-R, Plein & Baus GmbH (Burscheid, Germany) . . . 44

Appendix D

Publications

Articles

J. Jentzsch on behalf of the ATLAS Collaboration. "Performance tests during the ATLAS IBL Stave Integration". *Journal of Instrumentation, JINST 10 C04036* Doi: 10.1088/1748-0221/10/04/C04036, 2015.

ATLAS Collaboration. "ATLAS Pixel IBL: Stave Quality Assurance". *ATLAS Public Note*. ATL-INDET- PUB-2014-006, 2014.

J. Jentzsch on behalf of the ATLAS Collaboration. "Operational performance and status of the ATLAS Pixel Detector at the LHC". *World Scientific*, Doi: 10.1142/9789814603164_0074, 2014.

R. Nagai, J. Idarraga, C. Gallrapp, Y. Unno, **J. Jentzsch**, et al. "Evaluation of novel KEK/HPK n-in-p pixel sensors for ATLAS upgrade with testbeam". *Nuclear Instruments and Methods in Physics Research Section A, A699:78-83*, Doi:10.1016/j.nima.2012.04.081, 2013.

J. Jentzsch on behalf of the ATLAS IBL Collaboration. "Quality assurance and functionality tests on electrical components during the ATLAS IBL production". *Journal of Instrumentation, JINST 8 C02048*, Doi:10.1088/1748-0221/8/02/C02048, 2013.

ATLAS IBL Collaboration. "Prototype ATLAS IBL Modules using the FE-I4A Front-End Readout Chip". *Journal of Instrumentation, JINST P11010* Doi: 10.1088/1748-0221/7/11/P11010, 2012.

T. Wittig, S. Altenheiner, C. Goessling, **J. Jentzsch** et al. "Planar slim-edge pixel sensors for the ATLAS upgrades." *Journal of Instrumentation, JINST 7 C02051*, Doi: 10.1088/1748-0221/7/02/C02051, 2012.

J. Weingarten, S. Altenheiner, M. Beimforde, M. Benoit, M. Bomben, **J. Jentzsch** et al. "Planar pixel sensors for the ATLAS upgrade: beam tests results." *Journal of Instrumentation, JINST 7 P10028*, Doi: 10.1088/1748-0221/7/10/P10028, 2012.

S. Altenheiner, C. Goessling, **J. Jentzsch**, R. Klingenberg, D. Muenstermann et al. "Radiation hardness studies of n^+-in-n planar pixel sensors for the ATLAS upgrades". *Nuclear Instruments and Methods in Physics Research Section A, A658:25-29*, Doi: 10.1016/j.nima.2011.05.074, 2011.

Poster

J. Jentzsch on behalf of the ATLAS IBL Collaboration. "Quality assurance and functionality tests on electrical components during the ATLAS IBL production". TWEPP-12 Conference, September 2012.

Talks

J. Jentzsch. "Quality assurance measurements during the ATLAS Insertable B-Layer production and integration". HEP Seminar University College London, March 2015.

J. Jentzsch on behalf of the ATLAS Collaboration. "Performance tests during the IBL Stave Integration". PIXEL 2014 Conference, September 2014.

J. Jentzsch. "IBL summary from a planar perspective". Planar Pixel Sensor Meeting, May 2014.

J. Jentzsch. "3-dimensional Charge Collection Efficiency (3DCCE) Measurement of ATLAS-IBL and HL-LHC Tracking Detector Sensor Candidates". Particle Physics DPG Spring Meeting, National Conference, March 2014.

J. Jentzsch. "Stave QA Setup in SR1". ATLAS Upgrade Week, November 2013.

J. Jentzsch. "Quality control on detector components during the ATLAS IBL production". Annual Meeting of Students in the Wolfgang-Gentner-Programme. Oct. 2013.

J. Jentzsch on behalf of the ATLAS Collaboration. "Operational performance and status of the ATLAS Pixel Detector at the LHC". 14^{th} ICATPP 2013 Conference, September 2013.

J. Jentzsch. "Stave burn-in and QA in SR1". ATLAS Pixel Collaboration Week, June 2013.

J. Jentzsch. "IBL stave QA experience". Planar Pixel Sensor Meeting, May 2013.

J. Jentzsch. "Quality Control and Functionality Tests during ATLAS IBL production". Particle Physics DPG Spring Meeting, National Conference, March 2013.

J. Jentzsch. "IBL stave QA experience". Planar Pixel Sensor Meeting, Nov. 2012.

J. Jentzsch. "Stave0: Setup overview and DAQ". IBL General Meeting, Oct. 2012.

J. Jentzsch and Malte Backhaus. "Results from irradiated FE's and assemblies". IBL General Meeting, June 2011.

J. Jentzsch. "Characterization of planar n^+-in-n ATLAS FE-I4 Single Chip Assemblies". HEP Seminar Radboud Universiteit Nijmegen, May 2011.

J. Jentzsch. "Sensor studies of n^+-in-n planar pixel sensors for the ATLAS upgrades". Particle Physics DPG Spring Meeting, National Conference, April 2011.

J. Jentzsch. "First experiences with FE-I4 Single Chip Assemblies from a sensor perspective". Planar Pixel Sensor Meeting, February 2011.

J. Jentzsch. "A first look at n-bulk wafers from the PPS/RD50 common production." Planar Pixel Sensor Meeting, April 2010.

Je gravis la montagne, comme je gravis ma vie,
Tous ces regards croisés, si les ai compris
J'ai pourtant vu mille fois, et suis encore surprise
De la beauté des êtres qui m'ont fait lâcher prise.

- Zaz

Acknowledgments

I would like to thank my university supervisor Prof. Claus Gößling for granting me the opportunity to obtain a PhD in physics in his working group and for being my first referee of the thesis. I have learned a lot from him and I wish him all the best.

Secondly, I want to thank my CERN supervisors Heinz Pernegger, Daniel Dobos and Christoph Rembser for all their support and trust in my work. They taught me how to deal with the complex circumstances in scientific research and that colleagues should take good care of each other in order to be able to keep their heads up even in difficult situations. Daniel Dobos kindly supported me especially at the very end of the thesis, which I appreciated very much.

I would also like to thank the IBL SR1 Testing Team for the great deal of work we accomplished, the high diversity and the many lessons about life; Claudia Gemme, François-Xavier and Pedro for the very good collaboration during my qualification task; our dear colleagues from Université de Genève, especially Didier Ferrer, Alessandro La Rosa and Javier Bilbao, for the smooth stave, data and knowledge exchanges; the ATLAS Pixel and IBL Insertion Teams for letting me participate in the installation of both detectors and Daniel Hynds for his support and sharing of the Timepix telescope.

The next round of nice words I would like to spend on the legendary James Bond office. Up to eleven students sharing one room is not always easy but we made the best of it including a sweets table and a fancy coffee machine. I wish you all the best of luck for your theses and future plans. See you at the next gig of "The Emigrants".

I am grateful for having many dear colleagues and at the same time friends at CERN. Thank you, Timon Heim, for joining me during the planning phase of the QA setup at CERN, for staying with me the entire time of my PhD and most of all for becoming a very good friend of mine. I always appreciated our fruitful discussions and the productive working hours together as well as our evenings with too much whisky watching the cows and the sunset from your balcony. I hope you will find your way and that our paths will cross again some day! There were also Jens Dopke, Daniel Muenstermann, Alexander Bitadze and Michael Kagan who always helped out with advice and actions, no matter if work-related or not. Michael, however, deserves a very special thanks here for heroically saving the IBL project even though it nearly costed both our heads.

Apart from all the work at CERN I relished the company of many warm and friendly people: Crazy little Karo (with a "K"!), my dearest Sam, the horse riding troupe

Ruth, Josh and Kristof (thanks for proof-reading this thesis!), Steffi and Sarah from my favorite teachers' office, the Wednesday Doppelkopf/Skat crew, my super sweet summer students Christian (in favor of the Hanuschni), Thibaud and Umut as well as my fellow Gentner students. Thanks, Michael, for sneaking me into the heart of CMS! Et finalement je voudrais dire merci beaucoup au loup gris pour garder le mouton noir de perdre la boule! Tu es une merveille que j'ai pas mérité.

Even though I spent my PhD outside the TU Dortmund, there are still a few outstanding people I would like to mention and thank warmly for being with me nevertheless: my dear Silke for her awesomeness, Andreas for taking good care of her, my friends Niqui and Holger for having me witness the greatest moment in their life and my two favorite Fabis, among the countless Fabis I know, for their comfort in troubled times.

There is one very special person, very dear to me, who was supportive throughout my entire time at CERN, from the beginning up until the very last words I write here. I appreciate everything that you have done for me, especially for all the motivating words you sent me, no matter if I sat right next to you in the office or if I was far away traveling. Hvala lepo, Bane!

Ein ganz besonders warmes Dankeschön geht an meine Familie, vor allem meine Eltern, meine Großeltern, meinen Bruder und mein Cousinchen. Dafür, dass ihr mit mir bedingungslos durch dick und dünn geht. Dass ich machen kann, was auch immer ich will, und doch weiter eure Pickerick bleiben werde. Dass ihr so weit weg und doch näher bei mir seid als jeder andere Mensch.

I say goodbye to you all at once
Don't dare to face you all alone
I went from wreckage to world class
With a box of T-shirts and some records to sell
But times have changed
I have to defend my actions
The foundation crumbles and I have to leave
Thanks for everything
I couldn't ask for more
I say I love you all as I vanish through the Jester's door.

- In Flames

This work was supported by the Wolfgang Gentner Programme of the Federal Ministry of Education and Research.